2013

Autonomous Trajectory Planning by Convex Optimization

Xinfu Liu
Iowa State University

Autonomous Trajectory Planning by Convex Optimization

by

Xinfu Liu

A dissertation submitted to the graduate faculty

in partial fulfillment of the requirements for the degree of

DOCTOR OF PHILOSOPHY

Major: Aerospace Engineering

Program of Study Committee:

Ping Lu, Major Professor

Rai Dai

Wei Hong

Umesh Vaidya

Bong Wie

Iowa State University

Ames, Iowa

2013

DEDICATION

I would like to dedicate this dissertation to my wife, Sisi Dai, for her support, understanding and encouragement when I pursued this degree. I also would like to thank my sisters and my brother for taking care of our beloved parents.

TABLE OF CONTENTS

LIST OF FIGURES

ACKNOWLEDGEMENTS

I would like to express my sincere thankfulness to my advisor, Dr. Ping Lu, not only for his concern in my life, but also for his informed guidance and advice in the process of conducting research and writing this dissertation. His insights have always given me new ideas, and inspired me to work hard on the research. And I am truly fortunate to have had this opportunity to work with him. I am also very grateful to my committee members, Dr. Rai Dai, Dr. Wei Hong, Dr. Umesh Vaidya, and Dr. Bong Wie for their efforts and valuable suggestions to this work.

Finally, I would like to extend my sincere gratitude to the Chinese Scholarship Council for their financial support for my study in Iowa State University.

ABSTRACT

The objective of this dissertation is to use second-order cone programming (SOCP) for autonomous trajectory planning of optimal control problems arisen from aerospace applications. Rendezvous and proximity operations (RPO) of spacecraft in any general orbit include various constraints on acquisition of docking axis point, approach corridor, plume impingement inhibition, relative velocity, and rate of change of thrust. By a lossless relaxation technique, this highly constrained RPO problem (non-convex) is transformed into a relaxed problem the solution of which is proven to be the same as that of the original problem. Then a novel successive approximation method, forming a sequence of subproblems with linear and time-varying dynamics, is applied to solve the relaxed problem. Each subproblem is a SOCP problem which can be solved by state-of-the-art primal-dual interior point method. Constraints on collision avoidance, or more generally concave inequality state constraints, from any aerospace application also make a problem non-convex. A successive linearization method is employed to linearize the concave inequality constraints. It is proven that the successive solutions from this method globally converge to the solution of the original problem and the converged solution has no conservativeness. Further non-convex constraints include nonlinear terminal constraints which are handled by first approximated with first-order expansions, and then compensated with second-order corrections to improve the robustness of the approach. The effectiveness of the methodology proposed in this dissertation is supported by various applications in highly constrained RPO, finite-thrust orbital transfers, and optimal launch ascent.

CHAPTER 1. INTRODUCTION

1.1 Background

Orbital rendezvous and docking becomes more and more important as human exploration in space continues to increase. The history shows that the orbital rendezvous was developed in two diverged ways, which are the manual strategy and the automated methodology leaded by the United States and the Russian space programs respectively [1]. Since the ground support is impractical for time-critical missions, crew intervention is unavailable in spacecraft with small size, and sophisticated cooperation does not exist between vehicles when the target object is malfunctioning or uncooperative, autonomous trajectory planning , which is the process of planning the trajectory on-board without the involvement of ground support, crew on board, and complicated communication between vehicles, is significant for current and future missions. The purpose of this dissertation is to develop potential real-time algorithms for autonomous trajectory planning in various kinds of space missions by using convex optimization which can be solved very reliably and efficiently by interior-point methods.

First, for the mission of rendezvous and proximity operations (RPO) between a chaser spacecraft and a target spacecraft, which can be found in Refs. [1–4] about its history and related technologies, the majority of the present technology is based on the Clohessy-Wiltshire (CW) equations [5] having a set of linear and time-variant differential equations, derived by assuming that the distance between the chaser and the target is close and the target is in a circular orbit. The CW equations have an analytic solution which

provides a convenient way for terminal rendezvous. When the target is in any Keplerian orbit, linearized and time varying equations can be obtained to analyze the fuel-optimal rendezvous [6]. In addition, state transition matrix is available for the equations with application to terminal rendezvous [7, 8]. Nevertheless, the gap in the knowledge is that those methods are all based on the linearized model which becomes inaccurate or even invalid when the relative distance is not sufficient small. More importantly, they are not able to incorporate various kinds of constraints that are necessary in practice [9], such as those on approach corridor, hold points, plume impingement inhibition and relative velocity [10].

Second, consideration of perturbations is practically important for space missions since any spacecraft is subject to a variety of perturbations such as Earth gravity harmonics, atmospheric drag, third-body attractions and solar radiation pressure [11, 12]. For circular reference orbit, a set of linearized equations, incorporating the effect of J_2 perturbation, were developed in Ref. [13] for formation flying, which were also applied in studying the rendezvous maneuver for multiple spacecraft with consideration to the J_2 perturbation [14]. However, a general treatment to the perturbations, without linearization, is not available in the literature.

Another critical issue related to space missions is collision avoidance which ensures the safety of a spacecraft and its surrounding environment. For example, for the phase of proximity operations in the RPO problem, it is significant for the chaser to be outside of a keep-out-zone centered at the target to avoid possible collision with the target. The constraint from collision avoidance is challenging because it is a non-convex constraint. For polygonal obstacle avoidance with any number of sides, Ref. [15] proposed using a set of linear inequality equations with binary variables to represent the collision avoidance constraint. More specifically, ideas from Ref. [15] can be applied to approximate circular keep-out-zone avoidance with the appropriate number of linear equations

including binary variables, as shown in Fig. 1.1. At each discrete time point, only one linear inequality constraint in enforced, or the vehicle has to be on the outer side of at least one of those dashed lines, which is achieved by using one binary variable in each linear equation. If a large number of discretization points are needed for a problem in hand and at each time point a polygon with a sufficient number of sides are used to approximate the original keep-out-zone, the large number of binary variables would dramatically increase the computation cost. This is meliorated by using the time-step grouping technique in Ref. [15] to reduce the number of binary variables, even though it usually adds conservativeness to the original constraint.

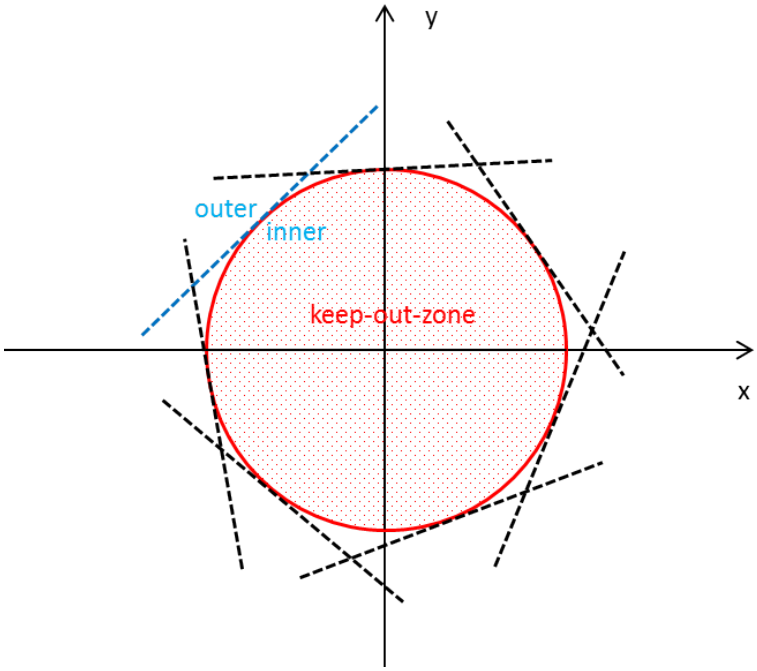

Figure 1.1 Collision avoidance constraint approximated by a set of linear equations with binary variables.

To avoid using the binary variables, an alternative is to approximate the keep-out-zone with a sequence of rotated tangent lines as in Refs. [16, 17], which is illustrated in Fig. 1.2. At each discrete time, only one linear inequality equation is employed, which excludes the use of binary variables and decreases the number of constraints to a large

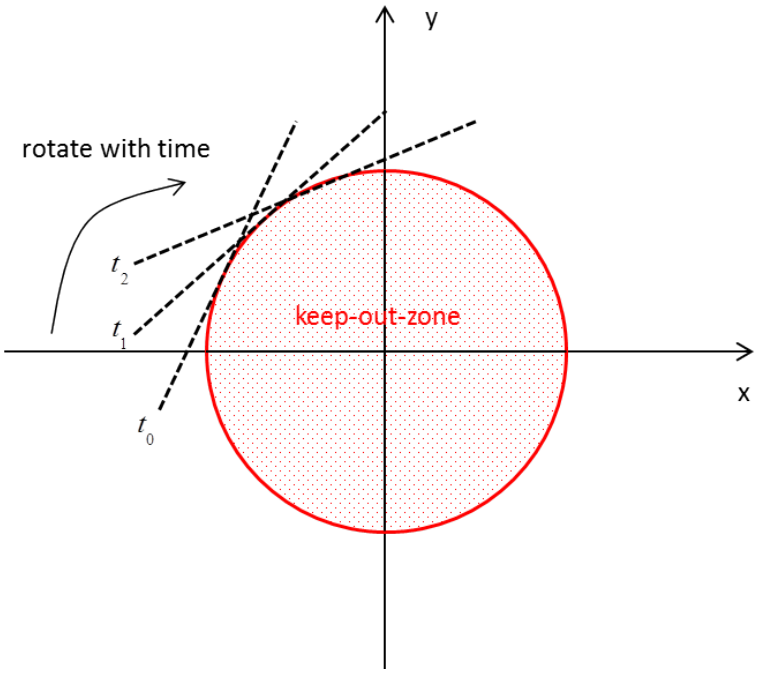

Figure 1.2 Collision avoidance constraint approximated by a series of rotated linear equations.

degree. This method requires to choose the location of the first tangent line and the rotation speed. Refs. [16, 17] propose to run a problem for multiple times over a range of different locations for the first line to find the best value. In addition, the rotation speed is determined to let the line make a full rotation for an orbital period [16]. Unfortunately, what makes the best value for the first tangent line is unclear and the constant rotation speed may result in convervativeness to the original constraint or even make a feasible problem to have infeasible solutions. For keep-out zone with other shapes such as ellipse or ellipsoid, it is even more difficult to choose the appropriate rotation speed.

Finally, space missions are usually formulated as optimal control problems with typical linear terminal constraints on the final position and velocity, but often nonlinear terminal constraints are necessities for a majority of the practical space missions, even though they make the problems to be non-convex and more difficult to solve. When the optimal control problems are discretized to nonlinear programming problems, the non-

linear terminal constraints are converted into nonlinear equality equations. A popular method to deal with those nonlinear constraints is the well-known sequential quadratic programming (SQP) method [18, 19] which linearizes the nonlinear constraints and includes their second-order (curvature) properties in the objective function. Consequently, a sequence of quadratic subproblems can then be solved by active-set methods discussed in details in Ref. [19].

For all the problems discussed above, they may have nonlinear dynamics, nonlinear convex constraints, and nonlinear non-convex constraints, which are challenging for most algorithms since they are non-convex optimization problems. In Ref. [20] a lossless relaxation method was applied to convexify non-convex control constraints for a class of optimal control problems. Similar ideas were used in Ref. [21] for convexification of the plume impingement inhibition constraints (or thrust direction constraints) which are non-convex in nature. The driving force behind it is that convex optimization problems can be reliably and efficiently solved by interior-point methods, while general nonlinear optimization problems are usually surprising difficult to solve [22]. Second-order cone programming (SOCP) problems, having a linear objective function and constraints being intersection of an affine set and the Cartesian product of second-order cones, are convex optimization problems and have a variety of applications [23, 24]. Particularly, planetary soft landing problems such as Mars landing can be efficiently dealt with SOCP based methodology [20, 21, 25, 26]. Primal-dual interior point methods (IPM) have been developed for SOCP [27, 28], and existing software capable solving SOCP include MOSEK [28], CPLEX, SDPT3 [29], SeDuMi [30], etc. Nevertheless, the problems considered in this dissertation are not in the form of SOCP and are highly constrained nonlinear optimization problems. As opposed to the constant gravity used in planetary soft landing, this dissertation considers inverse-square central force field, which is supposed to be more difficult due to its nonlinearity. Moreover, the inclusion of multiple interior-point constraints (or waypoints) in the RPO problems makes the already complex problems

more challenging to analyze, while they are not present in the planetary soft landing problems.

1.2 Research Contributions

Motivated by the gap in the knowledge for the problems discussed in the previous section, this dissertation first studies the RPO problem which uses the nonlinear equations of motion with inverse-square nonlinear gravity. Meanwhile, the problem includes all the necessary practical constraints such as those on thrust magnitude, plume impingement inhibition, approach corridor, hold points and relative velocity, which are not considered all together in the literature. A relaxed problem is obtained from the original highly constrained optimal control problem after convexifing the constraints on plume impingement inhibition and applying change of variables. Then this dissertation contributes to rigorously prove the equivalence of solutions between the original RPO problem and its relaxed problem. Due to the inverse-square gravitational field, nonlinearity still exists in the relaxed problem, which is overcome by a novel successive approximation method. Consequently, the relaxed problem is solved by a sequence of constrained subproblems with linear and time-varying dynamics. Each subproblem becomes a SOCP problem after discretization. This method is also capable of incorporating the perturbations from Earth harmonics J_2 and atmospheric drag without linearizing them.

For a problem with collision avoidance constraints, a successive linearization method (SLM) is proposed in this dissertation to instead solve a sequence of SOCP subproblems each of which avoids including binary variables in the constraints and at the same time uses the least number of constraints as that in Refs. [16, 17]. However, the SLM adds no conservativeness to the original constraints. More importantly, there are strong theoretical results to employ the SLM, which are that the successive solutions globally converge to at least a local solution for the original problem under mild assumptions. Meanwhile,

the practical effectiveness of the method is supported by some application examples.

When the terminal constraints are nonlinear, using the SQP method makes the problem have linear constraints by linearizing the nonlinear terminal constraints but have quadratic objective function which is not allowed in the SOCP based methodology. The method used in this dissertation leaves the linear objective function unchanged, linearizes the nonlinear terminal constraints, and adds second-order corrections to the linearized constraints to improve the robustness of the approach, which is proved to be effective and successful even for certain difficult problems through numerical demonstration. This approach can also be applicable to optimal control problems with nonlinear state equations.

1.3 Dissertation Organization

Autonomous trajectory planning to practical problems in aerospace is discussed in this dissertation which is organized as follows. Some preliminaries are given in Chapter 2, which are helpful and used in the following chapters. Chapter 3 presents a relaxation method and successive approximation method to transform the original problem into a series of SOCP problems for the rendezvous and proximity operations. Rigorous proof has been given to show the equivalence of the original problem and the relaxed one. Numerical results are provided to verify the convergence of the successive approximation method. While there is no consideration for perturbations in Chapter 3, a more realistic model is given in Chapter 4 to include the effects of perturbations from the gravity harmonic J_2 and atmospheric drag. The method discussed in Chapter 3 can efficiently incorporate those perturbations and some numerical examples are presented to support the analysis on the convergence of the algorithm. Other issues that are common in aerospace such as collision avoidance and nonlinear terminal conditions are the topics of Chapter 5 and Chapter 6 in which appropriate methods are developed to handle

those constraints so that the problems needed to be solved are still in the frame of SOCP, while the solutions obtained are for the original problems. With an attempt to implement a self-written solver for SOCP to have more efficiency and flexibility such as hot start, Chapter 7 describes the well-known primal-dual interior-point method in details. Finally, the conclusion is given in Chapter 8.

CHAPTER 2. PRELIMINARIES

2.1 Second-order Cone Programming

In this dissertation, the problems from the trajectory planning in aerospace are all transformed into second-order cone programming (SOCP) problems by various techniques. The SOCP problems, which are convex optimization problems, have linear objective subject to intersection of an affine set and product of quadratic (second order) cones [23, 24]. Linear programming (LP), convex quadratically programming (QP) and convex quadratically constrained quadratically programming (QCQP) problems can be formulated as SOCP problems, while SOCP is a special case of semidefinite programming (SDP) [31]. A standard form of the SOCP problem has the form of [28, 32]

$$(P) \text{ minimize} \qquad \boldsymbol{c}^T\boldsymbol{x} \tag{2.1}$$

$$\text{subject to} \qquad A\boldsymbol{x} = \boldsymbol{b} \tag{2.2}$$

$$\boldsymbol{x} \in K \tag{2.3}$$

where $\boldsymbol{x} \in R^n$ is the optimization variables. $A \in R^{m\times n}$ with $m \leq n$ and $rank(A) = n$, $\boldsymbol{c} \in R^n$ and $\boldsymbol{b} \in R^m$ are all given. K is a convex set that is the Cartesian product of linear cones K_+ and quadratic cones K_q which are defined as follows:

Definition 2.1.1. *Linear cone R_+:*

$$K_+ = \{x \in R \,:\, x \geq 0\}. \tag{2.4}$$

Quadratic cone K_q:

$$K_q = \{\boldsymbol{x} \in R^n \,:\, x_n \geq \sqrt{x_1^2 + \ldots + x_{n-1}^2},\, x_n \geq 0\}. \tag{2.5}$$

Rotated quadratic cone K_r:

$$K_r = \{\boldsymbol{x} \in R^n \ : \ \sqrt{2x_n x_{n-1}} \geq \sqrt{x_1^2 + \ldots + x_{n-2}^2}, \ x_n, x_{n-1} \geq 0\}. \tag{2.6}$$

Then, K can be expressed as

$$K = K^{n_1} \times K^{n_2} \times \cdots \times K^{n_r} \tag{2.7}$$

where each K^{n_i} represents either linear cone or quadratic cone, and n_i is the dimension of the cone. If $n_i = 1$, K^{n_i} defines the linear cone. For $n_i \geq 2$, the expression "$\boldsymbol{z} \in K^{n_i}$" for a $\boldsymbol{z} \in R^{n_i}$, or "$\boldsymbol{z} \geq_{K^{n_i}} 0$" means that

$$z_{n_i} \geq \sqrt{z_1^2 + \ldots + z_{n_i-1}^2} \tag{2.8}$$

Note that the rotated quadratic cone K_r is identical to the quadratic cone K_q under a linear transformation T [32], i.e.,

$$x \in K_r \Leftrightarrow Tx \in K_q \tag{2.9}$$

where

$$T = \begin{bmatrix} \frac{1}{\sqrt{2}} & \frac{1}{\sqrt{2}} & 0 & \cdots & 0 \\ \frac{1}{\sqrt{2}} & -\frac{1}{\sqrt{2}} & 0 & \cdots & 0 \\ 0 & 0 & 1 & \ldots & 0 \\ \vdots & \vdots & \vdots & \ddots & \vdots \\ 0 & 0 & 0 & \cdots & -1 \end{bmatrix} \tag{2.10}$$

In Eq. 2.8, the components of $\boldsymbol{z}$ are directly from $\boldsymbol{x}$, i.e., $\boldsymbol{z} = [x_l, \ldots, x_{l+n_i-1}]$. For quadratic cones or second order cones in the form of Eq. 2.8, it is convenient to express them in the form of Eq. 2.3. Nevertheless, when the second order cones are expressed as

$$\|G_i \boldsymbol{x} - \boldsymbol{h}_i\| \leq \boldsymbol{d}_i^T \boldsymbol{x} - e_i \tag{2.11}$$

where $G_i \in R^{(n_i-1)\times N}$, $\boldsymbol{h}_i \in R^{n_i-1}$, $\boldsymbol{c}_i \in R^N$, and $e_i \in R$, one can use the following notation to represent the cone [33]

$$A_i \boldsymbol{x} - \boldsymbol{b}_i \geq_{K^{n_i}} 0 \ \text{ (or } A_i \boldsymbol{x} - \boldsymbol{b}_i \in K^{n_i}) \tag{2.12}$$

where $A_i \in R^{n_i \times N}$ and $\boldsymbol{b}_i \in R^{n_i}$

$$[A_i; \boldsymbol{b}_i] = \begin{bmatrix} G_i & \boldsymbol{h}_i \\ \boldsymbol{d}_i^T & e_i \end{bmatrix} \tag{2.13}$$

Hence, a second order cone in the form of Eq. (2.11) is also identical to the quadratic cone K_q under the linear transformation defined in Eq. (2.13).

The SOCP problem can be solved efficiently by primal-dual interior-point method in polynomial time [28, 34, 35]. For more detains on SOCP and its applications, see Refs. [23, 24]. Chapter 7 also gives a detailed discussion on the primal-dual interior-point method in an attempt to implement a self-written solver for SOCP so that more flexibility and efficiency could be obtained.

2.2 Primal-Dual Interior Point Method

Primal-dual interior point method (IPM) is quite reliable and efficient in solving SOCP problems. It does not require user-supplied initial guess. In addition, it enjoys polynomial time convergence, and it is able to solve a SOCP problem within a number of iterations that are almost always in the range between 10 and 100. Moreover, by exploiting problem structure [28], such as sparsity, the method can efficiently solve very large problems with many thousands of variables and constraints. For SOCP problems considered in this dissertation, which have thousands of variables and constraints, the method can usually find the solutions in about one second. Finally, it is capable of detecting the infeasibility of either the primal problem or the dual problem. Therefore, for its high reliability and efficiency, the primal-dual IPM has the potential for on-board optimization or embedded optimization.

2.3 Coordinate Systems and Coordinate Transformations

In this dissertation, three coordinate systems are used, which are geocentric equatorial inertial coordinate system, perifocal coordinate system [36], and local vertical local horizontal coordinate system. First, the definition of those coordinate systems are introduced, then followed by the description of coordinate transformations among them.

2.3.1 Coordinate Systems

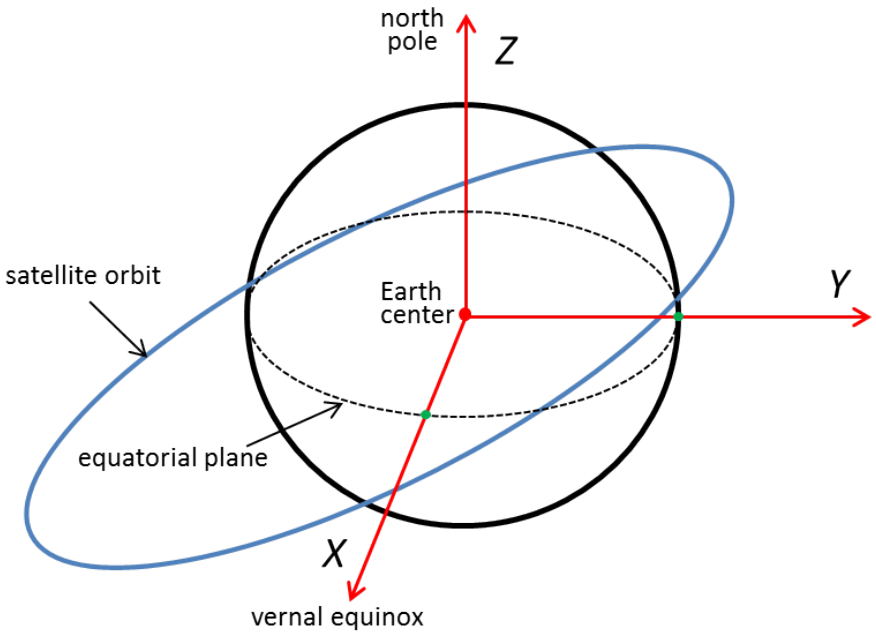

Figure 2.1 Geocentric-equatorial inertial coordinate system.

The Geocentric-Equatorial Inertial Coordinate System The geocentric equatorial inertial coordinate system (GEI) is an inertial frame which has its origin at the Earth's center and X-axis pointing in the vernal equinox direction. Z-axis points in the direction of the North pole. Y-axis completes the right-handed system, which, together with the X-axis, are all in the plane of equator, as shown in Fig. 2.1. Denote the unit vectors along the X, Y and Z axes be $\boldsymbol{I}$, $\boldsymbol{J}$, and $\boldsymbol{K}$, respectively.

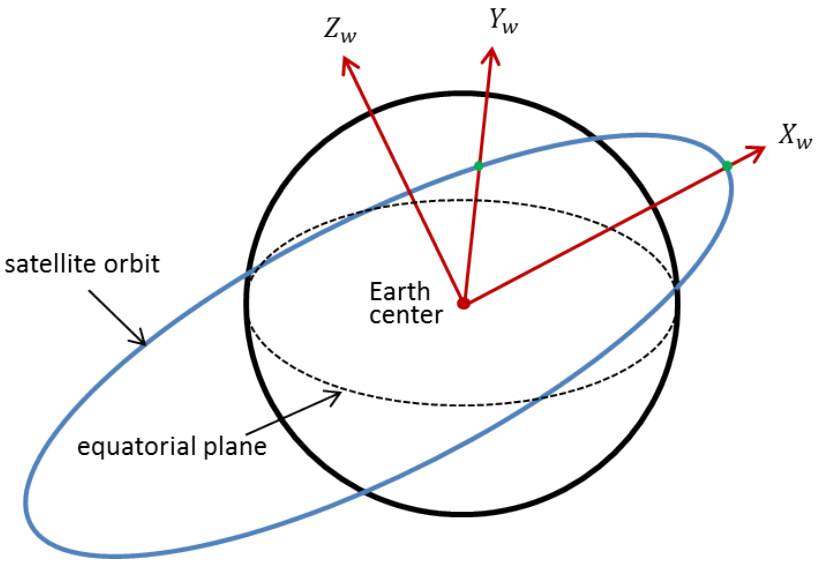

Figure 2.2 Perifocal coordinate system.

The Perifocal Coordinate System The perifocal coordinate system has the fundamental plane in the orbital plane, which is very convenient to describe the motion of a satellite. In Fig. 2.2, the X_w-axis points toward the perigee, Y_w-axis rotates 90 deg from the X_w-axis in the direction of the orbital motion and lies in the orbital plane, and Z_w-axis completes the righ-handed system. Unit vectors in the direction of X_w, Y_w and Z_w are $\boldsymbol{P}$, $\boldsymbol{Q}$ and $\boldsymbol{W}$ respectively.

The Local Vertical Local Horizontal Coordinate System In the local vertical local horizontal coordinate system (LVLH) centered at the satellite, shown in Fig. 2.3, the z-axis pointing to the Earth center is known as the local-vertical axis or R-bar axis. The x-axis is in the orbital plane of the satellite and perpendicular to the z-axis in the direction of the orbital motion. The z-axis is also called the local-horizontal axis or V-bar axis. The z-axis, or H-bar axis, completes a right-handed system. In this frame, the x-axis, y-axis and z-axis have their corresponding unit vectors $\boldsymbol{i}$, $\boldsymbol{j}$ and $\boldsymbol{k}$ respectively.

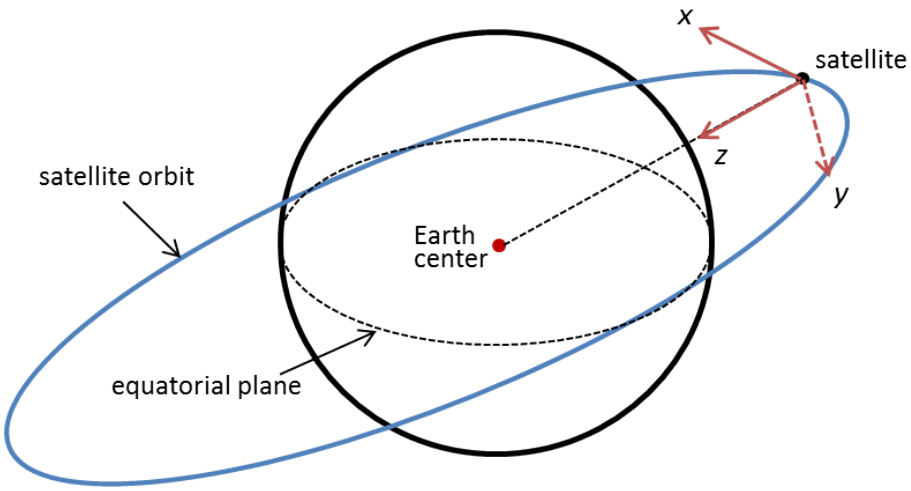

Figure 2.3 Local vertical local horizontal coordinate system.

2.3.2 Coordinate Transformations

To find the transformation matrix between two different coordinates, successive rotations about multiple axes can be used [36, 37]. Denote the transformation matrix from the GEI coordinate to the perifocal coordinate be $M^{P/G}$. First, refer to Fig. 2.4 for classical elements of an orbit. Then, based on Fig. 2.4, the perifocal coordinate can be formed by the following sequence of successive rotations from the GEI coordinate:

1. Rotate about the Z-axis with a positive angle Ω. Let X′-Y′-Z′ denote the axes for the new intermediate frame;

2. Rotate about the X′-axis with a positive angle i to yield a new frame with axes X″-Y″-Z″;

3. Rotate about the Z″-axis with a positive angle ω to get the perifocal coordinate frame.

Hence the rotation sequence can be written as: $C_z(\Omega) \rightarrow C_x(i) \rightarrow C_z(\omega)$ with [37]

$$C_z(\Omega) = \begin{bmatrix} \cos(\Omega) & \sin(\Omega) & 0 \\ -\sin(\Omega) & \cos(\Omega) & 0 \\ 0 & 0 & 1 \end{bmatrix} \tag{2.14}$$

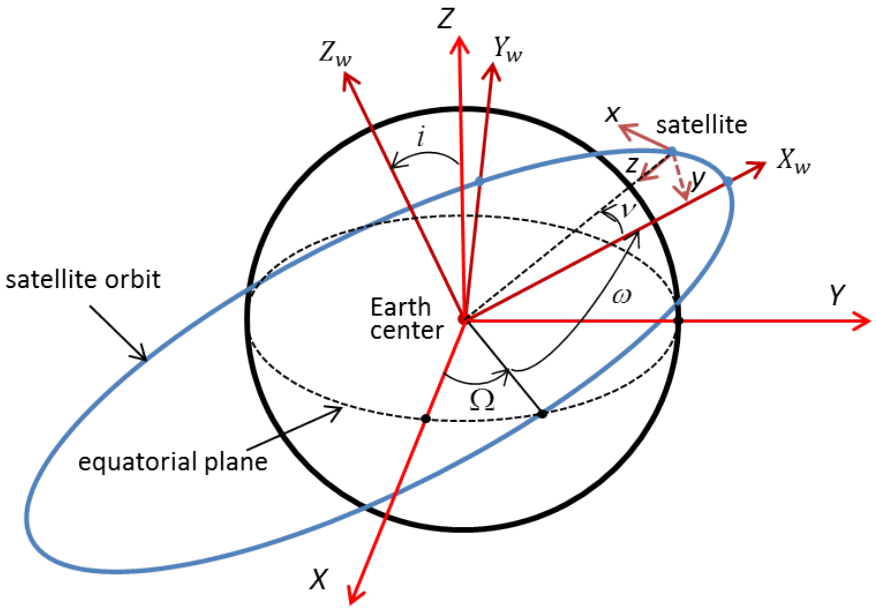

Figure 2.4 Orbital elements.

$$C_x(i) = \begin{bmatrix} 1 & 0 & 0 \\ 0 & \cos(i) & \sin(i) \\ 0 & -\sin(i) & \cos(i) \end{bmatrix} \tag{2.15}$$

$$C_z(\omega) = \begin{bmatrix} \cos(\omega) & \sin(\omega) & 0 \\ -\sin(\omega) & \cos(\omega) & 0 \\ 0 & 0 & 1 \end{bmatrix} \tag{2.16}$$

Then the transformation matrix $M^{P/G}$ is computed as follows

$$M^{P/G} = C_z(\omega)C_x(i)C_z(\Omega) \tag{2.17}$$

which implies that

$$\begin{bmatrix} \boldsymbol{P} \\ \boldsymbol{Q} \\ \boldsymbol{W} \end{bmatrix} = M^{P/G} \begin{bmatrix} \boldsymbol{I} \\ \boldsymbol{J} \\ \boldsymbol{K} \end{bmatrix} = C_z(\omega)C_x(i)C_z(\Omega) \begin{bmatrix} \boldsymbol{I} \\ \boldsymbol{J} \\ \boldsymbol{K} \end{bmatrix} \tag{2.18}$$

If a given vector $\boldsymbol{H} = [H_x, H_y, H_z]$ is expressed in the perifocal coordinate system as

$$\boldsymbol{H} = H_x\boldsymbol{P} + H_y\boldsymbol{Q} + H_z\boldsymbol{W} = [H_x \quad H_y \quad H_z] \begin{bmatrix} \boldsymbol{P} \\ \boldsymbol{Q} \\ \boldsymbol{W} \end{bmatrix} \tag{2.19}$$

Then by utilizing Eq. (2.18), in the GEI coordinate system $\boldsymbol{H}$ can be written as

$$\boldsymbol{H} = [H_x \quad H_y \quad H_z] \begin{bmatrix} \boldsymbol{P} \\ \boldsymbol{Q} \\ \boldsymbol{W} \end{bmatrix} = [H_x \quad H_y \quad H_z] M^{P/G} \begin{bmatrix} \boldsymbol{I} \\ \boldsymbol{J} \\ \boldsymbol{K} \end{bmatrix} \tag{2.20}$$

So $\boldsymbol{H}$ has coordinates $[H_x \quad H_y \quad H_z]M^{P/G}$ in the GEI coordinate system.

On the other hand, if a vector $\boldsymbol{F}$ is first given in the GEI coordinate system and has coordinates $[F_x, F_y, F_z]$, or

$$\boldsymbol{F} = F_x\boldsymbol{I} + F_y\boldsymbol{J} + F_z\boldsymbol{K} = [F_x \quad F_y \quad F_z] \begin{bmatrix} \boldsymbol{I} \\ \boldsymbol{J} \\ \boldsymbol{K} \end{bmatrix} \tag{2.21}$$

Similarly, we have

$$\boldsymbol{F} = [F_x \quad F_y \quad F_z][M^{P/G}]^{-1} \begin{bmatrix} \boldsymbol{P} \\ \boldsymbol{Q} \\ \boldsymbol{W} \end{bmatrix} \tag{2.22}$$

where $M^{P/G}$ has the following property [37]

$$[M^{P/G}]^{-1} = [M^{P/G}]^T = [C_z(\Omega)]^T[C_x(i)]^T[C_z(\omega)]^T \tag{2.23}$$

In addition, the transformation matrix from the perifocal coordinate system to the GEI coordinate system, if denoted as $M^{G/P}$, satisfies

$$M^{G/P} = [M^{P/G}]^{-1} = [M^{P/G}]^T \tag{2.24}$$

$$[M^{G/P}]^T = [M^{G/P}]^{-1} \tag{2.25}$$

Next, Let $M^{L/G}$ denote the transformation matrix from the GEI coordinate system to the LVLH coordinate system. Starting from the GEI coordinate system, we can obtain the LVLH coordinate system by the following rotation sequence:

1. Rotate about the X-axis with a positive angle $\frac{3\pi}{2}$;

2. In the new frame with axes X′-Y′-Z′, rotate about the Y′-axis with a positive angle $(2\pi - \Omega)$. The resulting frame has axes X″-Y″-Z″;

3. Then, rotate about the X″-axis with a positive angle i to generate the third intermediate frame with axes X‴-Y‴-Z‴;

4. Finally, rotate about the Y‴-axis with a positive angle $(\frac{3\pi}{2} - \omega - \nu)$ to arrive at the LVLH frame.

Each step gives a rotation matrix and they are given as follows:

$$D_x(\frac{3\pi}{2}) = \begin{bmatrix} 1 & 0 & 0 \\ 0 & \cos(\frac{3\pi}{2}) & \sin(\frac{3\pi}{2}) \\ 0 & -\sin(\frac{3\pi}{2}) & \cos(\frac{3\pi}{2}) \end{bmatrix} \tag{2.26}$$

$$D_y(2\pi - \Omega) = \begin{bmatrix} \cos(2\pi - \Omega) & 0 & -\sin(2\pi - \Omega) \\ 0 & 1 & 0 \\ \sin(2\pi - \Omega) & 0 & \cos(2\pi - \Omega) \end{bmatrix} \tag{2.27}$$

$$D_x(i) = \begin{bmatrix} 1 & 0 & 0 \\ 0 & \cos(i) & \sin(i) \\ 0 & -\sin(i) & \cos(i) \end{bmatrix} \tag{2.28}$$

$$D_y(\frac{3\pi}{2} - \omega - \nu) = \begin{bmatrix} \cos(\frac{3\pi}{2} - \omega - \nu) & 0 & -\sin(\frac{3\pi}{2} - \omega - \nu) \\ 0 & 1 & 0 \\ \sin(\frac{3\pi}{2} - \omega - \nu) & 0 & \cos(\frac{3\pi}{2} - \omega - \nu) \end{bmatrix} \tag{2.29}$$

Then,

$$M^{L/G} = D_y(\frac{3\pi}{2} - \omega - \nu)D_x(i)D_y(2\pi - \Omega)D_x(\frac{3\pi}{2}) \tag{2.30}$$

Similarly, Let $M^{G/L}$ be the transformation matrix from the LVLH coordinate name to the GEI coordinate frame. $M^{L/G}$ and $M^{G/L}$ have the following properties

$$[M^{L/G}]^{-1} = [M^{L/G}]^T = [D_x(\frac{3\pi}{2})]^T[D_y(2\pi - \Omega)]^T[D_x(i)]^T[D_y(\frac{3\pi}{2} - \omega - \nu)]^T \tag{2.31}$$

$$M^{G/L} = [M^{L/G}]^{-1} = [M^{L/G}]^T \tag{2.32}$$

$$[M^{G/L}]^T = [M^{G/L}]^{-1} \tag{2.33}$$

For the transformation of a vector between the GEI coordinate system and the LVLH coordinate system, follow the same method discussed above for the GEI coordinate system and the perifocal coordinate system.

CHAPTER 3. RENDEZVOUS AND PROXIMITY OPERATIONS

3.1 Introduction

Rendezvous and proximity operations (RPO) refer to the process of maneuvering a chaser spacecraft to have close distance with the target spacecraft, such as flying around/station-keeping, or physically dock with the target, which usually include far-field rendezvous phase, near-field rendezvous phase, proximity and docking phase [38]. PRO is a critical element of many space missions, such as the Soyuz program and the space shuttle program. Refs. [2–4] provided a detailed description on the history and technologies in RPO. The more recent activities in designing RPO for Orion Multiple-Purpose Crew Vehicle can be found in Refs. [10, 39]. Autonomous trajectory planning for the RPO is to plan the trajectory and generate guidance commands on-board with ground supports or crew intervention unavailable or impractical, which is crucial for time-critical missions and consideration of fuel optimization. Ref. [1] revealed the history and reasons on importance of the autonomy.

The Clohessy-Wiltshire (CW) equations [5] have played an important role for analysis in much of the current near-field and proximity operations. The CW equations are a set of linear, time-invariant differential equations and there exist two assumptions the first of which is the close distance between the chaser and the target, and the other of which is the restrictive circular orbit [40]. The CW equations provide a convenient way to analyze the relative motion between the chaser and the target, while they become

invalid even for an orbit with small eccentricity, e.g. $e < 0.1$. In addition, there is no analytic solution for the CW equations when practical constraints in RPO are included such as approach corridor constraints, plume-impingement inhibition, hold points, etc. Consequently, the CW equations become inadequate in practice. This dissertation is to develop a methodology to include all those constraints in the problem needed to be solved with consideration to fuel optimization, and design the trajectory on-board efficiently for the target in any Keplerian orbit.

It is common for problems in aerospace to be nonlinear and non-convex, which prevents the use of SOCP. For example, for limited-thrust system, the acceleration control input $\frac{\boldsymbol{T}}{m}$ is nonlinear, and the control constraints are non-convex [20]. Refs. [21, 25, 26] successfully applied the SOCP-based approach to solve powered descent guidance for Mars landing, which inspired the work of applying it to the RPO problem in this chapter [9]. The RPO problem in an inverse-square gravity field contains trajectory constraints including those on terminal conditions, hold points, approach corridor, plume-impingement inhibition, etc., which results in a highly constrained optimal control problem. In Section 3.2, a relaxation technique is used to transform the original problem into a more-like SOCP problem which has linear objective and convex constraint on plume-impingement inhibition. Meanwhile, rigorous proof is given to show the equivalence between the original problem and the relaxed problem. Nonlinearities resulting from the inverse-square gravity field are overcome by the successive approximation presented in Section 3.3 and its convergence is also analyzed. Numerical results are given in Section 3.4 to support the effectiveness of the methodology used in the RPO problem.

3.2 Problem Formulation

The point-mass three-dimensional equations of motion for a spacecraft in an inverse-square gravity field an Earth-centered inertial reference frame are

$$\ddot{\boldsymbol{r}} = -\frac{\mu}{r^3}\boldsymbol{r} + \frac{\boldsymbol{T}}{m} \tag{3.1}$$

where μ is called the *gravitational parameter* of the Earth, $\boldsymbol{r} \in R^{3\times 1}$ is a vector from the center of the Earth to the spacecraft and $r = \|\boldsymbol{r}\|$, $\boldsymbol{T}$ is the thrust vector of the spacecraft engine, and mass is m.

The above equations of motion, after normalization, can be written as [9]

$$\dot{\boldsymbol{r}} = \boldsymbol{V}, \qquad \boldsymbol{r}(0) = \boldsymbol{r}_0 \tag{3.2}$$

$$\dot{\boldsymbol{V}} = -(1/r^3)\boldsymbol{r} + \boldsymbol{T}/m, \qquad \boldsymbol{V}(0) = \boldsymbol{V}_0 \tag{3.3}$$

$$\dot{m} = -(1/v_{ex})\|\boldsymbol{T}\|, \qquad m(0) = m_0 \tag{3.4}$$

where the position vector $\boldsymbol{r}$ is normalized by R_0, the radius of the Earth. The velocity vector $\boldsymbol{V} \in R^{3\times 1}$ is normalized by $\sqrt{g_0 R_0}$ with g_0 being the gravitational acceleration at R_0. $\boldsymbol{T}$, m and t are normalized by $m_0 g_0$, m_0 and $\sqrt{R_0/g_0}$, respectively. The thrust $\boldsymbol{T} \in R^{3\times 1}$ is the control input vector. The fuel consumption is dependent on $\|\boldsymbol{T}\|$ and v_{ex}, the dimensionless constant effective exhaust velocity of the engines. The initial position, velocity and mass are given as $\boldsymbol{r}_0$, $\boldsymbol{V}_0$, and m_0, respectively.

For RPO, the chaser spacecraft follows a certain trajectory, usually fuel optimal path, to move closer to the target spacecraft from a far distance and finally dock with it so that they have the same final position and velocity and move together thereafter. During the process, there are considerations for fuel cost, safe operation, plume impingement

inhibition, etc. The problem considered is given as follows:

$$\text{Minimize} \quad J = \int_0^{t_f} \|\boldsymbol{T}\| dt \tag{3.5}$$

$$\text{Subject to} \quad \dot{\boldsymbol{x}} = f(\boldsymbol{x}, \boldsymbol{T}) \tag{3.6}$$

$$\|\boldsymbol{T}\| \leq T_{max} \tag{3.7}$$

$$\|\boldsymbol{r}(t) - \boldsymbol{r}_t(t)\| \cos\alpha \leq \mathbf{1}_n^T(t)(\boldsymbol{r}(t) - \boldsymbol{r}_t(t)) \tag{3.8}$$

$$\mathbf{1}_n^T(t)\boldsymbol{T} \leq \|\boldsymbol{T}\| \cos\theta \tag{3.9}$$

$$C_f(t_f)\boldsymbol{x}(t_f) + \boldsymbol{d}_f(t_f) = 0 \tag{3.10}$$

$$C_i(t_i)\boldsymbol{x}(t_i) + \boldsymbol{d}_i(t_i) = 0,\ i = 1, \ldots, l,\ 0 < t_1 < \cdots < t_l < t_f \tag{3.11}$$

where $\mathbf{1}_n$ is a unit vector representing the docking axis fixed on the target, thus moving with the target viewed in the inertial frame. The states of the spacecraft is denoted as $\boldsymbol{x} = (\boldsymbol{r}; \boldsymbol{V}; m) \in R^{7\times 1}$.

The performance index is to minimize the fuel/propellant consumption J in (3.5). The dynamic equations (3.2)–(3.4) are combined in equation (3.6) which is a nonlinear equation. The upper bound T_{max} in Eq. (3.7), which is equal to the maximum thrust magnitude divided by $m_0 g_0$ in a dimensionless sense, is engine dependent, and a spacecraft is in coast when $\|\boldsymbol{T}\| = 0$. Constraint (3.8), with $\boldsymbol{r}(t)$ being the position of the chaser and $\boldsymbol{r}_t(t)$ the position of the target, describes the approach corridor within which the chaser spacecraft should stay when they are close enough (relative distance is less than 200 m for instance), which is shown in Fig. 3.1 with α of usually 10∼15 deg. The equation (3.9) specifies the consideration on plume impingement inhibition, where θ is the minimum angle the thrust plume has to be pointed away from the target in order to avoid contamination. Specifically, when $\theta = 0$ the thrust vector can be in any direction, while for $\theta = 180$ deg the thrust vector can only point to the target with the plume in the opposite direction of the thrust direction. It is usually necessary to include this constraint when the chaser is in close range to the target. Meanwhile, the angle θ

can be chosen as time-varying parameter according to specific practical mission. Hence, constraints (3.8) and (3.9) are enforced only when the chaser is in proximity of the target.

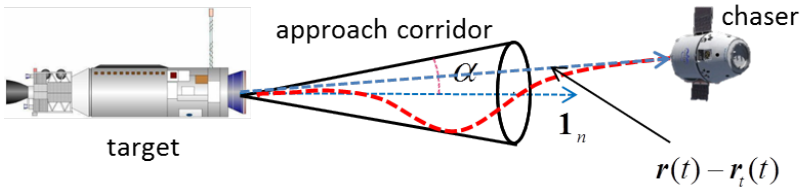

Figure 3.1 Approach corridor for the rendezvous and proximity operations.

The constraints for terminal conditions are expressed in Eq. (3.10), which are linear at this point. Chapter 6 will further discuss nonlinear terminal constraints. For an example on linear terminal constraints, a rendezvous mission has

$$\boldsymbol{x}(t_f) - \boldsymbol{x}_t(t_f) = 0 \tag{3.12}$$

which is to say that the final state of the chaser is the same as that of the target. For constraints on parts of the states or different relationship on final states between the two spacecraft, appropriate form of the constraints could be used. In addition, when necessary, constraint (3.11) can be added to achieve certain conditions at prescribed intermediate times $t_i < t_f$. For example, if the chaser is required to be d m in front of of the target along the docking axis $\mathbf{1}_n$ at t_1, then we have

$$[I_{3\times 3} \quad 0_{3\times 3}]\boldsymbol{x}(t_1) - (\boldsymbol{r}_t(t_1) + d\,\mathbf{1}_n) = 0 \tag{3.13}$$

which is called Acquisition of Docking Axis (ADA) in practical RPO.

3.2.1 Relaxation

In order to apply SOCP to solve the problem (3.5)–(3.11), it requires the problem to have a linear objective, linear constraints, quadratic or second-order cone constraints all of which are convex. However, the performance index in (3.5) contains norm of a

vector and is thus nonlinear. In addition, the dynamic equation (3.6) is nonlinear and the plume impingement inhibition constraint(3.9) is non-convex for $\theta \in [0, \pi/2)$. So, it is necessary to transform the original problem (3.5)–(3.11) to the form of SOCP.

First, a relaxed version is obtained by replacing $\|\boldsymbol{T}\|$ with η in constraints (3.4), (3.5) and (3.9), which is

$$\text{Minimize} \quad J = \int_0^{t_f} \eta dt \tag{3.14}$$

$$\text{Subject to} \quad \dot{\boldsymbol{r}} = \boldsymbol{V} \tag{3.15}$$

$$\dot{\boldsymbol{V}} = -(1/r^3)\boldsymbol{r} + \boldsymbol{T}/m \tag{3.16}$$

$$\dot{m} = -(1/v_{ex})\eta \tag{3.17}$$

$$\|\boldsymbol{T}\| \leq \eta \tag{3.18}$$

$$0 \leq \eta \leq T_{max} \tag{3.19}$$

$$\|\boldsymbol{r}(t) - \boldsymbol{r}_t(t)\| \cos\alpha \leq \mathbf{1}_n^T(t)(\boldsymbol{r}(t) - \boldsymbol{r}_t(t)) \tag{3.20}$$

$$\mathbf{1}_n^T(t)\boldsymbol{T} \leq \eta \cos\theta \tag{3.21}$$

$$C_f(t_f)\boldsymbol{x}(t_f) + \boldsymbol{d}_f(t_f) = 0 \tag{3.22}$$

$$C_i(t_i)\boldsymbol{x}(t_i) + \boldsymbol{d}_i(t_i) = 0,\ i = 1, \ldots, l,\ 0 < t_1 < \cdots < t_l < t_f \tag{3.23}$$

The performance index (3.14) is now linear after discretization. The dynamic equation (3.15)–(3.17) having $\boldsymbol{u} = (\boldsymbol{T}; \eta)$ as the new control input no longer contains $\|\boldsymbol{T}\|$, but it is still nonlinear because of the coupling of $\boldsymbol{T}$ and m as $\frac{\boldsymbol{T}}{m}$, plus the existence of the nonlinear term $\frac{1}{r^3}\boldsymbol{r}$. The constraint (3.7) in the original problem is relaxed with a convex set defined by (3.18) and (3.19), as in Refs. [21, 25, 26]. The original non-convex thrust direction constraint (3.9) becomes to Eq. (3.21) due to the replacement, which is a half-space and thus convex.

Even though the above relaxed problem still contains nonlinearity in Eq. (3.16), which prevents the direct use of SOCP to solve it, significant progress has been made by

transforming the objective function (3.5) and the thrust direction constraint (3.9) in the original problem into their convex forms (3.14) and (3.21) respectively. If we set aside the nonlinearity in Eq. (3.16) for the moment, the biggest concern now is whether the relaxed problem still has the same solution with the original one. First, it is easy to check that both problems are the same when $\|\boldsymbol{T}\| = \eta$, which is stated as the following proposition

Proposition 3.2.1. *The original problem Eqs. (3.5)–(3.11) and the relaxed problem Eqs. (3.14)–(3.23) are equivalent if and only if the following condition holds in the solution to the relaxed problem almost everywhere (a.e.) in* $[0, t_f]$

$$\|\boldsymbol{T}\| = \eta \tag{3.24}$$

This equivalence is evident by comparing the two problems: the relaxed problem becomes the original problem if $\|\boldsymbol{T}\| = \eta$ almost everywhere in the solution of the relaxed problem. In fact, this condition is checked *a posteriori* in all our numerical solutions to make sure that the solution found for the relaxed problem is indeed also that of the original problem. In the rest of this section, theoretical assurance of this equivalence is established.

Ref. [21] investigates the equivalence of the solutions of similarly posed problems for powered landing (earlier and less comprehensive versions of the problem and proofs can be found in Refs. [25] and [26]). There the key differences in Ref. [21] from this chapter are that the gravity is constant (both in magnitude and direction), constraints (3.23) are not present, and an assumption is required that there are at most some isolated points on the trajectory where a state inequality constraint like (3.20) is active. Here the gravity is from an inverse-square central force field, therefore the system dynamics are nonlinear, and the multiple interior-point constraints impact the trajectory differently. Furthermore, in our applications frequently the optimal trajectory lies on the boundaries of inequality constraints for some finite durations. Hence we will need to provide a general answer

to the question of equivalence of solutions, including the case when the state inequality constraint (3.20) is active in some subinterval(s) of finite length(s).

The following assumption will exclude a pathological case from consideration in the following theoretical investigation.

Assumption 1

If the constraint (3.21) is present, the optimal trajectory of the relaxed problem (3.14)–(3.23) does not contain any finite segment where the pointing constraint (3.21) is active, while the following conditions hold simultaneously

$$\frac{\mathbf{1}_n^T(t)\boldsymbol{T}(t)}{\cos\theta} = \text{constant}, \quad \text{and } 0 < \frac{\mathbf{1}_n^T(t)\boldsymbol{T}(t)}{\cos\theta} < T_{max} \tag{3.25}$$

Although it is probable that the constraint (3.21) is active in a finite interval, the constancy condition in Eq. (3.25) is very restrictive, given that $\mathbf{1}_n(t)$ and $\boldsymbol{T}(t)$ are both time varying. The conditions in Eq. (3.25) render such optimal trajectory highly unlikely. If the constraint (3.21) is not imposed, Assumption 1 is not needed.

First a result is stated and proved for the case when constraints (3.23) are not considered.

Lemma 3.2.1. *In the absence of the interior-point constraints (3.23) and under Assumption 1, if the optimal trajectory for the relaxed problem Eqs. (3.14)–(3.22) has no points where the constraint (3.20) is active, the solution to the relaxed problem is identical to that of the original problem Eqs. (3.5)–(3.10) without the interior-point constraints (3.11).*

Proof. Suppose that $\boldsymbol{y}^*(t) = (\boldsymbol{x}^{*T}(t)\ m^*(t))^T$ and $\boldsymbol{u}^*(t) = (\boldsymbol{T}^{*T}(t)\ \eta^*)^T$ are the optimal state and control solutions to the problem Eqs. (3.14)–(3.22). By the Maximum Principle [41], there exists in $[0, t_f]$ a continuous, nonzero costate vector function $\boldsymbol{p}(t) = (\boldsymbol{p}_r^T(t)\ \boldsymbol{p}_V^T(t)\ p_m(t)\ p_0)^T$, where $\boldsymbol{p}_r \in R^3$, $\boldsymbol{p}_V \in R^3$, $p_m \in R$ and $p_0 \geq 0$ is a

constant, such that for the Hamiltonian H defined below,

$$H = \boldsymbol{p}_r^T \boldsymbol{V} + \boldsymbol{p}_V^T \left(-\frac{1}{\|\boldsymbol{r}\|^3} \boldsymbol{r} + \frac{\boldsymbol{T}}{m} \right) - \frac{p_m \eta}{v_{ex}} - p_0 \eta \tag{3.26}$$

the costates satisfy the differential equations

$$\dot{\boldsymbol{p}}_r = -\frac{\partial H}{\partial \boldsymbol{r}} = \frac{1}{\|\boldsymbol{r}\|^3} \boldsymbol{p}_V - \frac{3(\boldsymbol{p}_V^T \boldsymbol{r})}{\|\boldsymbol{r}\|^5} \boldsymbol{r} \tag{3.27}$$

$$\dot{\boldsymbol{p}}_V = -\frac{\partial H}{\partial \boldsymbol{V}} = -\boldsymbol{p}_r \tag{3.28}$$

$$\dot{p}_m = -\frac{\partial H}{\partial m} = \frac{(\boldsymbol{p}_V^T \boldsymbol{T})}{m^2} \tag{3.29}$$

Along the optimal trajectory for each fixed t, $\boldsymbol{y}^*(t)$ and the corresponding $\boldsymbol{p}(t)$, the optimal values $\boldsymbol{T}^*(t)$ and $\eta^*(t)$ are determined by pointwise maximization of H in Eq. (3.26) with respect to $\boldsymbol{T}$ and η [41]

$$\max_{(\boldsymbol{T},\eta) \in \mathscr{U}} H[\boldsymbol{y}^*(t), \boldsymbol{p}(t), \boldsymbol{T}, \eta] \tag{3.30}$$

where

$$\mathscr{U} = \{(\boldsymbol{T}, \eta) \mid \|\boldsymbol{T}\| \leq \eta, \mathbf{1}_n^T(t) \boldsymbol{T} \leq \eta \cos\theta, 0 \leq \eta \leq T_{max}\} \tag{3.31}$$

Furthermore, H is a constant along the optimal trajectory because the dynamics are autonomous and this is a fixed-time problem. First, assume $\boldsymbol{p}_V \neq 0$ *a.e.* in $[0, t_f]$. Then with respect to $\boldsymbol{T}$, H is a non-constant, linear (thus convex) function. For each $\eta > 0$ the maximization of H with respect to $\boldsymbol{T}$ is performed over a bounded convex set

$$\mathscr{U}_T = \{T \mid \|\boldsymbol{T}\| \leq \eta, \mathbf{1}_n^T(t) \boldsymbol{T} \leq \eta \cos\theta\} \tag{3.32}$$

A unique solution to this constrained pointwise maximization problem exists on the boundary of $\mathscr{U}_T$ [42], and it satisfies the Karush-Kuhn-Tucker (KKT) conditions [22] (for minimizing $f = -H$)

$$-\frac{\boldsymbol{p}_V}{m} + \frac{\lambda_1}{\|\boldsymbol{T}\|} \boldsymbol{T} + \lambda_2 \mathbf{1}_n(t) = 0 \tag{3.33}$$

where

$$\begin{cases} \lambda_1 = 0 & \text{if } \|\boldsymbol{T}^*\| < \eta \\ \lambda_1 \geq 0 & \text{if } \|\boldsymbol{T}^*\| = \eta \end{cases}; \quad \begin{cases} \lambda_2 = 0 & \text{if } \mathbf{1}_n^T(t)\boldsymbol{T} < \eta\cos\theta \\ \lambda_2 \geq 0 & \text{if } \mathbf{1}_n^T(t)\boldsymbol{T} = \eta\cos\theta \end{cases} \tag{3.34}$$

Since the unique solution for the optimal $\boldsymbol{T}^*$ exists which must satisfy Eq. (3.33), this requires that $\lambda_1 \neq 0$. Thus the constraint (3.18) $\|\boldsymbol{T}\| \leq \eta$ must be active, i.e., $\|\boldsymbol{T}^*\| = \eta$.

And it follows that $\|\boldsymbol{T}^*\| = \eta^*$ when η takes its optimal value. By Proposition 3.2.1, the solutions to the relaxed and original problems are the same.

Next, consider the case where $\boldsymbol{p}_V = 0$ in a finite interval in $[0, t_f]$. It follows from Eqs. (3.27) and (3.28) that we must have $\boldsymbol{p}_V = \boldsymbol{p}_r \equiv 0$ in $[0, t_f]$. Thus $p_m =$ constant by Eq. (3.29). Since the final mass $m(t_f)$ is free, the transversality condition for $p_m(t_f)$ is [41]

$$p_m(t_f) = 0 \tag{3.35}$$

Therefore $p_m \equiv 0$ in $[0, t_f]$. The Hamiltonian H in Eq. (3.26) in this case reduces to

$$H = -p_0\eta \tag{3.36}$$

Because $\boldsymbol{p}$ is nonzero, it must be true that the non-negative p_0 is not zero (i. e., $p_0 > 0$), since already $\boldsymbol{p}_r = \boldsymbol{p}_V = p_m = 0$. The condition (3.30) applied with respect to η means maximization of H in (3.36) over the set

$$\mathscr{U}_\eta = \{\eta \mid \mathbf{1}_n^T(t)\boldsymbol{T} \leq \eta\cos\theta,\ 0 \leq \eta \leq T_{max}\} \tag{3.37}$$

The optimal η^* then should be the lower bound of the (non-empty) convex set $\mathscr{U}_\eta$. Given the required constancy of H, it is straightforward to verify that under Assumption 1, the set $\mathscr{U}_\eta$ is equivalent to

$$\mathscr{U}_\eta = \{\eta \mid 0 \leq \eta \leq T_{max}\} \tag{3.38}$$

Therefore the lower bound of $\mathscr{U}_\eta$ is 0 and

$$\eta^* = 0 \tag{3.39}$$

As a consequence constraint (3.18) admits only one solution $\boldsymbol{T}^* = 0$. But this again implies condition (3.24). It follows from Proposition 3.2.1 again that the solution to the relaxed problem is again the same as that to the original problem. □

When the inequality constraint (3.20) becomes active in $[0, t_f]$, and/or when the interior-point constraints (3.23) are added, what complicates the analysis is the fact that the costate will be only piecewise continuous, separated by the so-called jump conditions at the point(s) where the trajectory enters the boundary of the constraint (3.20), and at the instances $t_1, \ldots, t_l$ where the constraints (3.23) are imposed. Rewrite constraint (3.20) as

$$\|\boldsymbol{r}(t) - \boldsymbol{r}_t(t)\| \cos\alpha - \mathbf{1}_n^T(t)(\boldsymbol{r}(t) - \boldsymbol{r}_t(t)) := h(\boldsymbol{r}, t) \leq 0 \tag{3.40}$$

Constraint (3.40) is a second-order constraint with respect to the control vector $\boldsymbol{u}$, i.e., $\boldsymbol{T}$ (a part of $\boldsymbol{u}$) first appears in the second-order time derivative of $h(\boldsymbol{r}, t)$. Differentiating $h(\boldsymbol{r}, t)$ twice and using Eqs. (3.15) and (3.16) give

$$\ddot{h} = \boldsymbol{\gamma}^T(\boldsymbol{r}, t)\boldsymbol{T} + \phi(\boldsymbol{r}, \boldsymbol{V}, t) := q(\boldsymbol{x}, \boldsymbol{T}, t) \tag{3.41}$$

Suppose that $[t_{in},\ t_{out}] \subset [0, t_f]$ is an interval where the constraint (3.40) becomes active. Then the jump condition for the costates are [43]

$$\begin{pmatrix} \boldsymbol{p}_r(t_{in}^+) \\ \boldsymbol{p}_V(t_{in}^+) \end{pmatrix} = \begin{pmatrix} \boldsymbol{p}_r(t_{in}^-) \\ \boldsymbol{p}_V(t_{in}^-) \end{pmatrix} + \nu_1 \frac{\partial h}{\partial \boldsymbol{x}} + \nu_2 \frac{\partial \dot{h}}{\partial \boldsymbol{x}} \tag{3.42}$$

where ν_1 and ν_2 are two constant multipliers. Similarly, at the points $t_1, \ldots, t_l$, the interior-point constraints (3.23) will cause jump conditions of the form [43]

$$\begin{pmatrix} \boldsymbol{p}_r(t_i^+) \\ \boldsymbol{p}_V(t_i^+) \end{pmatrix} = \begin{pmatrix} \boldsymbol{p}_r(t_i^-) \\ \boldsymbol{p}_V(t_i^-) \end{pmatrix} + C_i^T \boldsymbol{\nu}_i, \quad i = 1, \ldots, l \tag{3.43}$$

where $\boldsymbol{\nu}_i$ is vector multiplier of appropriate dimension (the same as the row dimension of the C_i matrix). On the other hand, the following points should be made on the continuity of the Hamiltonian along the optimal trajectory of the relaxed problem:

- Since the times $t_1, \ldots, t_l$ are specified, the Hamiltonian H is continuous across $t_1, \ldots, t_l$, despite of the jumps in $\boldsymbol{p}_r$ and $\boldsymbol{p}_V$ at these points [43].

- Likewise it can be shown that the Hamiltonian is continuous at t_{in}, even though $\boldsymbol{p}_r$ and $\boldsymbol{p}_V$ are discontinuous in general at t_{in} due to Eq. (3.42). Parts of Theorems 5 and 22 in Ref. [41] on $H = 0$, with and without state inequality constraints, imply such continuity for free-time problems. Similar conclusion holds for the constancy of the Hamiltonian for fixed-time problems, thus H remains continuous in $[0, t_f]$.

These jump conditions preclude the use of similar arguments as in the proof of Lemma 1 to establish the equivalence of the solutions and necessitate a more involved approach. The following results will be used in this approach.

Lemma 3.2.2. *If the solution to the relaxed problem Eqs. (3.14)–(3.23) contains any finite subinterval in $[0, t_f]$ where $\|\boldsymbol{T}^*\| < \eta^*$ (i.e., the inequality (3.18) holds strongly), this must be an interval where $\boldsymbol{p}_V = 0$.*

Proof. The proof is given in the Appendix. □

Lemma 3.2.3. *Under Assumption 1, if the solution to the relaxed problem Eqs. (3.14)–(3.23) contains any finite subinterval of $[0, t_f]$ where $\boldsymbol{p}_V = 0$, the solution must have $\eta^* = T_{max}$ in that interval.*

Proof. The proof is also provided in the Appendix. □

Lemma 3.2.4. *Under Assumption 1, the optimal solution to the relaxed problem Eqs. (3.14)–(3.23) satisfies the condition $\|\boldsymbol{T}^*\| = \eta^*$ a.e. in $[0, t_f]$*

Proof. We shall prove the result by contradiction. Assume that there is a least one finite interval $[t_b, t_e] \subset [0, t_f]$ where $\|\boldsymbol{T}^*(t)\| = \beta(t) < \eta^*(t)$. By Lemma 3.2.2 this can only be an interval where $\boldsymbol{p}_V = 0$. By Lemma 3.2.3, this is also where $\eta^* = T_{max}$. In the following it will be shown that another feasible trajectory with a smaller cost can be constructed on the basis of these conditions to contradict the optimality of the given solution.

Since $\beta(t) < \eta^* = T_{max}$ in $[t_b, t_e]$, it is always possible to find a function $\varepsilon(t)$ such that $\varepsilon(t_b) = 0$, $\varepsilon(t) > 0, \forall t \in (t_b, t_e]$, and

$$[1 + \varepsilon(t)]\,\beta(t) \leq T_{max} \tag{3.44}$$

Specifically, choose $\varepsilon(t)$ as

$$\varepsilon(t) = \frac{1}{2}\varepsilon_0(t - t_b)\left[1 + \frac{m^*(t_b)}{m^*(t)}\right], \quad t \in [t_b, t_e] \tag{3.45}$$

where $m^*(t) = m^*(t_b) - T_{max}(t - t_b)/v_{ex}$ is the optimal mass history in $[t_b, t_e]$ for the relaxed problem, and $\varepsilon_0 > 0$ a sufficiently small constant such that the condition (3.44) remains true in the interval. Clearly such an ε_0 exists. For instance, let $\beta_{max} = \sup \beta(t)$ for $t \in [t_b, t_e]$ (obviously $\beta_{max} < T_{max}$ by the assumption that $\beta < T_{max}$). Then any ε_0 satisfying

$$0 < \varepsilon_0 \leq (T_{max}/\beta_{max} - 1) \,/\, \{(t_e - t_b)\,[1 + m^*(t_b)/m^*(t_e)]\}$$

will do. Define a new thrust profile $\boldsymbol{T}$ in $[t_b, t_e]$ by

$$\boldsymbol{T}(t) = [1 + \varepsilon(t)]\,\boldsymbol{T}^*(t), \quad t \in [t_b, t_e] \tag{3.46}$$

This $\boldsymbol{T}$ has the same direction as $\boldsymbol{T}^*$, but with greater magnitude, yet is still admissible because of condition (3.44). Furthermore, define a function

$$\delta(t) = -\varepsilon_0 v_{ex} m^*(t) < 0, \quad t \in [t_b, t_e] \tag{3.47}$$

Construct a control η in the interval

$$\eta(t) = T_{max} + \delta(t) < T_{max} = \eta^*, \quad t \in [t_b, t_e] \tag{3.48}$$

The inequality holds because $\delta < 0$. Clearly $\eta \geq 0$ when ε_0 is sufficiently small. So this η is also admissible. Let

$$m(t) = m^*(t_b) + \int_{t_b}^{t} \dot{m}(\tau)d\tau = m^*(t_b) - \int_{t_b}^{t} \frac{\eta(\tau)}{v_{ex}}d\tau$$

be the mass profile from Eq. (3.17) corresponding to this η in the interval $[t_b, t_e]$ with the same initial condition $m(t_b) = m^*(t_b)$. It can be shown that

$$m(t) = [1 + \varepsilon(t)]\, m^*(t), \quad t \in [t_b, t_e] \tag{3.49}$$

Note that there is no discontinuity in $m(t)$ at $t = t_b$ because $\varepsilon(t_b) = 0$. Hence for this new admissible control $\boldsymbol{u} = (\boldsymbol{T}, \eta)$, the following equation holds

$$\frac{\boldsymbol{T}(t)}{m(t)} = \frac{\boldsymbol{T}^*(t)}{m^*(t)}, \quad t \in [t_b, t_e] \tag{3.50}$$

From Eqs. (3.16) and (3.15), condition (3.50) implies that starting from the same condition as on the optimal trajectory at the beginning of the interval $[t_b, t_e]$, the trajectory for $\boldsymbol{x} = (\boldsymbol{r}^T \ \boldsymbol{V}^T)^T$ under the new control $\boldsymbol{u}$ in this interval will be identical to that of the optimal solution (therefore satisfying all trajectory constraints). In particular, at the end of the interval, $\boldsymbol{r}(t_e) = \boldsymbol{r}^*(t_e)$ and $\boldsymbol{V}(t_e) = \boldsymbol{V}^*(t_e)$, yet $m(t_e)$ now is greater than $m^*(t_e)$ because $|\dot{m}(t)| = \eta(t)/v_{ex} < T_{max}/v_{ex} = |\dot{m}^*|$ in $[t_b, t_e]$. But this contradicts the fuel/mass optimality of the solution $\boldsymbol{y}^* = (\boldsymbol{r}^*(t),\ \boldsymbol{V}^*(t),\ m^*(t))$. Thus the assumption that $\|\boldsymbol{T}^*\| < \eta^*$ in a finite interval cannot be true, and we must have $\|\boldsymbol{T}^*\| = \eta^*$ *a.e.* in $[0, t_f]$. □

Note that Lemma 3.2.4 only states that $\|\boldsymbol{T}^*\| = \eta^*$ in the solution of the relaxed problem, but does not suggest that $\eta^* = T_{max}$ always. In fact, in a finite interval where constraint (3.20) is active where necessarily $\ddot{h} = \boldsymbol{\gamma}^T(\boldsymbol{r}, t)\boldsymbol{T} + \phi(\boldsymbol{r}, \boldsymbol{V}, t) = 0$ (cf. Eq. (3.41)), it can be seen that in general $\eta^* = \|\boldsymbol{T}^*\| < T_{max}$ in a finite interval where $h \equiv 0$.

Combining Lemma 3.2.4 and Proposition 3.2.1, it is concluded that

Proposition 3.2.2. *Under Assumption 1, the solutions to the relaxed problem Eqs. (3.14)-(3.23) and the original problem in Eqs. (3.5)-(3.11) are the same.*

3.2.2 Change of Variables

In order to cancel the nonlinearity in the dynamic equation, the following change of variables is applied to the relaxed problem:

$$\boldsymbol{\tau} = \frac{\boldsymbol{T}}{m},\ \sigma = \frac{\eta}{m},\ z = \ln m \tag{3.51}$$

Then from the mass equation $\frac{\dot{m}(t)}{m(t)} = \dot{z} = -\frac{1}{v_{ex}}\sigma(t)$, we obtain

$$m(t) = m_0 \exp[-\frac{1}{v_{ex}}\int_0^t \sigma(s)ds] \tag{3.52}$$

So maximizing $m(t_f)$ is to minimize the equivalent performance index

$$J = \int_0^{t_f} \sigma(t)dt$$

For constraint (3.19), it becomes

$$0 \le \sigma \le T_{max}e^{-z} \tag{3.53}$$

and can be approximated with [25]

$$0 \le \sigma \le T_{max}e^{-z_0}[1-(z-z_0)] \tag{3.54}$$

where z_0 is the natural logarithm function of the nominal change of mass. It should be mentioned that constraint (3.53) includes constraint (3.54), i. e., any σ satisfying (3.54) also satisfies (3.53) [25]. So the problem (3.14)–(3.23) can be further written as

$$\text{Minimize} \quad J = \int_0^{t_f} \sigma dt \tag{3.55}$$

$$\text{Subject to} \quad \dot{\boldsymbol{x}} = A(r)\boldsymbol{x} + B\boldsymbol{u} \tag{3.56}$$

$$\|\boldsymbol{\tau}\| \le \sigma \tag{3.57}$$

$$0 \le \sigma \le T_{max}e^{-z_0}[1-(z-z_0)] \tag{3.58}$$

$$\|\boldsymbol{r}(t) - \boldsymbol{r}_t(t)\|\cos\alpha \le \mathbf{1}_n^T(t)(\boldsymbol{r}(t) - \boldsymbol{r}_t(t)) \tag{3.59}$$

$$\mathbf{1}_n^T(t)\boldsymbol{\tau} \le \sigma\cos\theta \tag{3.60}$$

$$C_f(t_f)\boldsymbol{x}(t_f) + \boldsymbol{d}_f(t_f) = 0 \tag{3.61}$$

$$C_i(t_i)\boldsymbol{x}(t_i) + \boldsymbol{d}_i(t_i) = 0,\ i = 1,\ldots,l,\ 0 < t_1 < \cdots < t_l < t_f \tag{3.62}$$

where $\boldsymbol{x} = (\boldsymbol{r}; \boldsymbol{V}; z)$ and $\boldsymbol{u} = (\boldsymbol{\tau}; \sigma)$. The constraint (3.56) is now a linear time-varying equation with

$$A(r) = \begin{bmatrix} 0_{3\times3} & I_{3\times3} & 0_{3\times1} \\ -\frac{1}{r^3} I_{3\times3} & 0_{3\times3} & 0_{3\times1} \\ 0_{1\times3} & 0_{1\times3} & 0 \end{bmatrix}, \quad B = \begin{bmatrix} 0_{3\times3} & 0_{3\times1} \\ I_{3\times3} & 0_{3\times1} \\ 0_{1\times3} & -1/v_{ex} \end{bmatrix} \tag{3.63}$$

Now the problem (3.55)–(3.62) can be solved by a sequence of SOCP subproblems if $A(r)$ is treated as a constant time-varying matrix in each subproblem and updated after having its solution at each iteration by using the method of successive approximation, which is the subject of the next section.

3.3 Solution to the RPO

3.3.1 Successive Approximation

The only nonlinearity in the state equations in problem (3.55)-(3.62) is in the term $1/r^3$ in the A matrix. In many cases the percentage of variations for r is very small, and the approximation of $r \approx r_0$ may suffice, where r_0 is the initial radius. This is exactly the basis for the so-called "linear gravity" model proposed by Jezewski [44]. In such a case A is a constant matrix, and the dynamics in Eq. (3.56) are linear. As a more general approach applicable to all cases with high precision, a successive solution method is devised in this chapter. In this approach, the following procedure is taken to find the solution of the relaxed problem:

1. Set $k = 1$, and $r^{(0)}(t) = r_0$, and $z^{(0)}(t) = \ln(1 - \dot{m}_c t)$, where $\dot{m}_c > 0$ is an arbitrary constant dimensionless mass rate such that for the given final time t_f, $\dot{m}_c t_f \leq m_p$ with m_p as the (dimensionless) propellant mass carried by the vehicle. A simple choice is

$$\dot{m}_c = \frac{m_p}{t_f} \tag{3.64}$$

2. Solve the following optimal control problem to find the solution pair $\{\boldsymbol{u}^{(k)}, \boldsymbol{x}^{(k)}\}$:

   Given the state equations and initial condition:

$$\dot{\boldsymbol{x}}^{(k)} = A[r^{(k-1)}(t)]\boldsymbol{x}^{(k)} + B\boldsymbol{u}^{(k)}, \quad \boldsymbol{x}^{(k)}(0) = \boldsymbol{x}(0) \tag{3.65}$$

   minimize for the given t_f

$$J = \int_0^{t_f} \sigma^{(k)}(t)dt \tag{3.66}$$

   subject to

$$\|\boldsymbol{\tau}^{(k)}(t)\| \leq \sigma^{(k)}(t) \tag{3.67}$$

$$0 \leq \sigma^{(k)}(t) \leq T_{max}e^{-z^{(k-1)}(t)} \left\{1 - [z^{(k)}(t) - z^{(k-1)}(t)]\right\} \tag{3.68}$$

$$\|\boldsymbol{r}^{(k)}(t) - \boldsymbol{r}_t(t))\| \cos\alpha \leq \mathbf{1}_n^T(t) \left[\boldsymbol{r}^{(k)}(t) - \boldsymbol{r}_t(t)\right] \tag{3.69}$$

$$\mathbf{1}_n^T\boldsymbol{\tau}^{(k)}(t) \leq \sigma^{(k)}(t)\cos\theta \tag{3.70}$$

$$C_f(t_f)\boldsymbol{x}^{(k)}(t_f) + \boldsymbol{d}_f(t_f) = 0 \tag{3.71}$$

$$C_i(t_i)\boldsymbol{x}^{(k)}(t_i) + \boldsymbol{d}_i(t_i) = 0, \ i = 1, \ldots, l, \ 0 < t_1 < \cdots < t_l < t_f \tag{3.72}$$

   where $\boldsymbol{x}^{(k)} = \text{col}(\boldsymbol{r}^{(k)} \ \boldsymbol{V}^{(k)})$, and $r^{(k-1)}(t) = \|\boldsymbol{r}^{(k-1)}(t)\|$ and $z^{(k-1)}(t)$ are already found from the previous solution.

3. Check to see whether the convergence condition has been met for a prescribed tolerance $\varepsilon > 0$

$$\sup_{0 \leq t \leq t_f} \|\boldsymbol{x}^{(k)}(t) - \boldsymbol{x}^{(k-1)}(t)\| \leq \varepsilon, \quad k > 1 \tag{3.73}$$

   If the above condition is satisfied (for $k > 1$), go to Step 4; otherwise, set $k = k+1$, and go to Step 2.

4. The solution to the problem is found to be $\boldsymbol{x} = \boldsymbol{x}^{(k)}$ and $\boldsymbol{u} = \boldsymbol{u}^{(k)}$. Stop.

Remarks:

- For each k the problem (3.65)–(3.72) is one with linear, time-varying dynamics, linear equality constraints and second-order-cone inequality constraints. Yet it is still a *nonlinear* optimal control problem (because of the conic constraints), but ready to be discretized into an SOCP problem and solved numerically.

- The above problems do not involve linearization in the conventional sense of small perturbations. The converged solution found is the one that satisfies exactly (to the accuracy of the numerical solution) the original nonlinear gravity model. On a related note, a successive solution approach is proposed in Ref. [45] to find the solution satisfying the linearized dynamics (in the conventional sense) in the proximity of a small celestial body, starting from a polynomial initial guessed trajectory.

- The above procedure suggests that even if the linear gravity approximation is accurate (e.g., trajectory near a circular orbit), at least two successive solutions will be needed in most cases because the optimal thrust profile (which consists of bang-bang structure in most cases) is unknown. Compared to Ref. [46] where the linear gravity model is used to solve for an optimal multiple-burn ascent trajectory all at once, the major difference is that the burn-coast structure (the number of burn and coast arcs) is specified in the problems treated in Ref. [46]. Here no such information is prescribed *a priori*. Consequently the initial guessed mass profile defined by $z^{(0)}(t)$ is generally far from the final solution. However, the final solution found here will automatically determine the *optimal* number of burn and coast arcs as well as their durations in a problem.

Finally, a complete rendezvous mission is typically divided into several phases, e. g., far-field phasing, near-field maneuvers and final approach, each having distinctly different primary objectives and requirements, and relying on different navigation means and propulsion systems. It may be beneficial for the planning of RPO trajectory to determine the best initial condition which will in turn serve as the target condition for

the preceding phase. In such a case the initial condition (position and velocity vectors) in Eq. (3.56) may be treated as unspecified, to be optimized subject to the box constraints

$$\boldsymbol{r}_L \leq \boldsymbol{r}^{(k)}(0) \leq \boldsymbol{r}_U, \quad \boldsymbol{V}_L \leq \boldsymbol{V}^{(k)}(0) \leq \boldsymbol{V}_U \tag{3.74}$$

where $\boldsymbol{r}_L$, $\boldsymbol{r}_U$, $\boldsymbol{V}_L$, and $\boldsymbol{V}_U$ are all in R^3 and prescribed.

3.3.2 Convergence

As the equivalence of the solutions of the relaxed problem and the original problem has already been established, our attention turns to the convergence of the solution sequence $\{\boldsymbol{y}^{(k)}\}$ in Section 3.3.1 to the solution of the relaxed problem.

The closest resemblance in the literature to the approach in this chapter is the work in Ref. [47]. The optimal control problem considered there is one with nonlinear system dynamics of the form

$$\dot{x} = A(\boldsymbol{x})\boldsymbol{x} + B(\boldsymbol{x})\boldsymbol{u}, \quad \boldsymbol{x}(0) = \boldsymbol{x}_0 \tag{3.75}$$

with performance index

$$J = \frac{1}{2}\boldsymbol{x}^T(t_f)F\boldsymbol{x}(t_f) + \frac{1}{2}\int_0^{t_f} \left[\boldsymbol{x}^T Q(\boldsymbol{x})\boldsymbol{x} + \boldsymbol{u}^T R(\boldsymbol{x})\boldsymbol{u}\right] dt \tag{3.76}$$

where $F \geq 0$, $Q(\boldsymbol{x}) \geq 0$ and $R(\boldsymbol{x}) > 0$ for all $\boldsymbol{x}$. The solution to the above problem is found by solving successively the following time-varying linear quadratic regulator problems

$$\dot{\boldsymbol{x}}^{(k)} = A(\boldsymbol{x}^{(k-1)})\boldsymbol{x}^{(k)} + B(\boldsymbol{x}^{(k-1)})\boldsymbol{u}^{(k)}, \quad \boldsymbol{x}^{(k)}(0) = \boldsymbol{x}_0 \tag{3.77}$$

with quadratic performance index

$$J^{(k)} = \frac{1}{2}\boldsymbol{x}^{(k)T}(t_f)F\boldsymbol{x}^{(k)}(t_f) + \frac{1}{2}\int_0^{t_f} \left[\boldsymbol{x}^{(k)T} Q(\boldsymbol{x}^{(k-1)})\boldsymbol{x}^{(k)} + \boldsymbol{u}^{(k)T} R(\boldsymbol{x}^{(k-1)})\boldsymbol{u}^{(k)}\right] dt \tag{3.78}$$

Assume that $A(\boldsymbol{x})$ satisfies the following conditions

$$\mu(A(\boldsymbol{x})) \leq \mu_0 \tag{3.79}$$

$$\|A(\boldsymbol{x}) - A(\boldsymbol{y})\| \leq c\|\boldsymbol{x} - \boldsymbol{y}\| \tag{3.80}$$

for some positive constant μ_0 and c, where μ in Eq. (3.79) denotes the logarithmic norm of the matrix [48]. Under these two conditions and another pair of boundedness and Lipschitz conditions, the convergence of the above solution sequence $\{\boldsymbol{x}^{(k)}\}$ is proved [47]. For time-invariant bilinear systems with quadratic performance index, Refs. [49] and [50] also use an iterative approach that constructs a successive solution sequence, and the converges of the solutions under a mild condition is proved.

For our problem we first state an obvious fact based on the physics.

Proposition 3.3.1. *Consider the system in Eqs. (3.2)–(3.4), subject to constraint (3.7). For given T_{max} and fraction of propellant mass, there exist appropriate positive numbers r_{min}, r_{max}, V_{min}, V_{max}, $r_{0_{min}}$, $r_{0_{max}}$, $V_{0_{min}}$, $V_{0_{max}}$,$\gamma_{0_{max}}$, and $t_{f_{max}}$ such that for any fixed $t_f \leq t_{f_{max}}$ and initial condition $(\boldsymbol{r}(0), \boldsymbol{V}(0)) \in X_0$ where*

$$X_0 = \{(\boldsymbol{r}_0, \boldsymbol{V}_0) \mid r_{0_{max}} \leq \|\boldsymbol{r}_0\| \leq r_{0_{max}}, V_{0_{min}} \leq \|\boldsymbol{V}_0\| \leq V_{0_{max}},$$
$$|\boldsymbol{r}_0^T \boldsymbol{V}_0| \leq \|\boldsymbol{r}_0\| \|\boldsymbol{V}_0\| \sin(\gamma_{0_{max}})\}$$

the trajectory will satisfy the following condition for any $\boldsymbol{T}(t)$ meeting $\|\boldsymbol{T}\| \leq T_{max}$

$$r_{min} \leq \|\boldsymbol{r}(t)\| \leq r_{max}, \ \forall t \in [0, t_f] \tag{3.81}$$

$$V_{min} \leq \|\boldsymbol{V}(t)\| \leq V_{max}, \ \forall t \in [0, t_f] \tag{3.82}$$

The above conclusion can be easily proven, given that the unforced solution of the system is the well-understood Keplerian motion. For the relaxed problem with dynamics in Eqs. (3.15)–(3.17) subject to constraints (3.18) and (3.19), since $\|\boldsymbol{T}\| \leq \eta \leq T_{max}$, the same conclusion will hold.

For our problem, the desired convergence of $\{\boldsymbol{x}^{(k)}\}$ to the solution of the original problem requires two prerequisites: (a) the relaxed problem (3.14)–(3.23) has solution; (b) the original problem (3.5)–(3.11) has solution. Let $\mathscr{F}$ denote the set of feasible solutions to the relaxed problem (3.14)–(3.23), i. e., $\mathscr{F}$ is the collection of all the solutions

that satisfy Eqs. (3.15)-(3.23). We have the following assurance regarding the existence of the solution(s).

Proposition 3.3.2. *Assume that $\mathscr{F}$ is not empty, and the problem data are such that Proposition 3.3.1 holds. Then the solution to the relaxed problem (3.14)–(3.23) exists. Furthermore, if Assumption 1 in the preceding section is assumed to hold, the solution to the original problem (3.5)–(3.11) also exists.*

Proof. The proof of the existence of solution to the relaxed problem directly follows Corollary 2 in Chapter 4 of Ref. [51]. The relaxed problem is affine in the control $\boldsymbol{u} = (\boldsymbol{T}^T \ \eta)^T)$, so is the integrand in the performance index (3.14). Proposition 3 ensures that the state trajectory of the problem is bounded. All other conditions required in Corollary 2 of Ref. [51] are satisfied (Corollary 2 does not include the interior-point constraints (3.23) in the problem statement. But the addition of those will not change the proof and conclusion). Hence the solution to the relaxed problem exists. By the Conclusion in the preceding section, the solution to the original problem is the same as that to the relaxed problem, hence the solution to the original problem exists as well. □

As shown in Ref. [47] for quadratic problems, whether $\{\boldsymbol{x}^{(k)}\}$ converges heavily depends on the properties of the $A(r)$ matrix in Eq. (3.56). The definition of A matrix in Eq. (3.63) gives

$$A(r)^T A(r) = \begin{bmatrix} \frac{1}{r^6} I_{3\times 3} & 0_{3\times 3} & 0_{3\times 1} \\ 0_{3\times 3} & I_{3\times 3} & 0_{3\times 1} \\ 0_{1\times 3} & 0_{1\times 3} & 0 \end{bmatrix} \tag{3.83}$$

which gives

$$\|A(r)\| = \sqrt{\lambda_{max}(A(r)^T A(r))} = 1 \tag{3.84}$$

since r is normalized by R_0 and $r > 1$. Eq. (3.84) further results in

$$\|A(r_1) - A(r_2)\| \leq \|A(r_1)\| + \|A(r_2)\| = 2 \tag{3.85}$$

To find $\mu(A(r))$, we first have

$$A(r)^T + A(r) = \begin{bmatrix} 0_{3\times3} & (1-\frac{1}{r^3})I_{3\times3} & 0_{3\times1} \\ (1-\frac{1}{r^3})I_{3\times3} & 0_{3\times3} & 0_{3\times1} \\ 0_{1\times3} & 0_{1\times3} & 0 \end{bmatrix} \tag{3.86}$$

Then

$$\mu(A(r)) = \lambda_{max}(\frac{A(r)^T + A(r)}{2}) = \frac{1}{2}(1-\frac{1}{r^3}) \tag{3.87}$$

With the Eq. (3.81), the above equation yields

$$\mu(A(r)) \leq \frac{1}{2}(1-\frac{1}{r_{min}^3}) \tag{3.88}$$

Therefore, the boundedness on the logarithmic norm of $A(r)$, i.e. Eq. (3.88), is derived similar to the Eq. (3.79). Note that Eq. (3.80) is replaced by a slight different form of Eq. (3.84), which, however, would still validate the convergence proof in Ref. [47]. But a complete theoretical proof of convergence of the successive solution sequence $\{\boldsymbol{x}^{(k)}\}$ appears much more difficult than those cases reported in the literature, because it is not a quadratic problem and there are various constraints (3.7)–(3.11). In a way Proposition 3.3.2 also reveals why such a proof would be difficult: a proof the convergence of $\{\boldsymbol{x}^{(k)}\}$ would be equivalent to the proof of the existence of the solution to the original nonlinear optimal control problem in Eqs. (3.5)–(3.11). A general proof of the latter is likely to be rather elusive. However, given the naturally weak nonlinearity in the A matrix due to relatively small percentage of variations in r (recall the successful applications of "linear gravity" approximations [44, 46]), it is rather natural in practice to expect convergence in just a few iterations. Our numerical experiences have always shown good convergence of the successive solutions, even in the case of highly eccentric orbits where the variations of r are not small.

3.4 Numerical Results

Let us consider a chaser spacecraft with an initial mass of 1385 kg and specific impulse I_{sp} of 200 sec. The target spacecraft is in an equatorial orbit which could be either circular or elliptic. An circular orbit of radius 370 km is chosen to demonstrate the simulation results, while a highly elliptic orbit with $e = 0.5$ is used, which has perigee altitude of 370 km and apogee altitude of 13866.27 km. GPOPS is also used to verify the optimality of the solution obtained from the SOCP method when it is applicable. The test is performed on a 3GHz dual-core PC with 8GB of RAM and Windows 7 Enterprise operating system.

3.4.1 Rate of Change of Thrust Vector

It is important to first point out the importance of constraining the rate of change of thrust vector before presenting the simulations for different cases. Let us see the rate of change of thrust magnitude, shown in the red curve of Fig. 3.2, when a chaser spacecraft, initially located 5 km behind and 500 m below the target spacecraft which is in the elliptic orbit with $e = 0.5$ and perigee altitude of 370 km, approaches and docks the target spacecraft by using the V-bar approach. It is obvious that the thrust magnitude chatters or changes quickly after $t = 1800$ sec when the chaser spacecraft is within the approach corridor. The thrust profile is still a bang-bang control for $t \in (0, 1800)$ sec since there is only one constraint on the maximum thrust magnitude besides inherent dynamic equation constraints. However, the rapid thrust chattering is found to be common at the moments when inequality constraints such as approach corridor constraint and plume impingement inhibition become active. Such chattering is an artifact of how the optimal control problem is posed: the problem is not told that rapid chattering of the control vector is not desirable. Due to the limited capability of a spacecraft to change quickly its thrust magnitude or direction, it is necessary to constrain the rate of change of $\boldsymbol{T}$,

which can be achieved by adding another two dynamic equations and the corresponding constraint equations as follows

$$\dot{\boldsymbol{\tau}} = \boldsymbol{\nu} \tag{3.89}$$

$$\dot{\sigma} = \lambda \tag{3.90}$$

$$\|\boldsymbol{\nu}\| \leq \xi, \quad |\lambda| \leq \zeta \tag{3.91}$$

where ξ is specified maximum rate of change of thrust direction, and ζ a specified maximum rate of change of thrust magnitude. The constraints in (3.91) are still second-order cone constraints which can be handled very effectively by SOCP. The states and controls in the dynamic equation (3.56) are now redefined as $\boldsymbol{x} = (\boldsymbol{r}; \boldsymbol{V}; z; \boldsymbol{\tau}; \sigma)$ and $\boldsymbol{u} = (\boldsymbol{\nu}; \lambda)$. As a result, matrices $A(r)$ and B become

$$A(r) = \begin{bmatrix} 0_{3\times3} & I_{3\times3} & 0_{3\times1} & 0_{3\times3} & 0_{3\times1} \\ -\frac{1}{r^3}I_{3\times3} & 0_{3\times3} & 0_{3\times1} & I_{3\times3} & 0_{3\times1} \\ 0_{1\times3} & 0_{1\times3} & 0 & 0_{1\times3} & -1/v_{ex} \\ 0_{3\times3} & 0_{3\times3} & 0_{3\times1} & 0_{3\times3} & 0_{3\times1} \\ 0_{1\times3} & 0_{1\times3} & 0 & 0_{1\times3} & 0 \end{bmatrix}, \quad B = \begin{bmatrix} 0_{3\times3} & 0_{3\times1} \\ 0_{3\times3} & 0_{3\times1} \\ 0_{1\times3} & 0 \\ I_{3\times3} & 0_{3\times1} \\ 0_{1\times3} & 1 \end{bmatrix} \tag{3.92}$$

So the problem is (3.55)–(3.62) with (3.56) redefined above plus the additional constraint (3.91). When the constraint on rate of change of thrust magnitude is enforced, the blue curve in Fig. 3.2 shows that the thrust profile within the approach corridor is much smoother, indicating improvement with respect to practical applications. The parameters ξ and ζ in (3.91) can be chosen according to the capabilities of a specific spacecraft. Note that most of the time it might be necessary to only include constraint on the rate of change of the thrust magnitude.

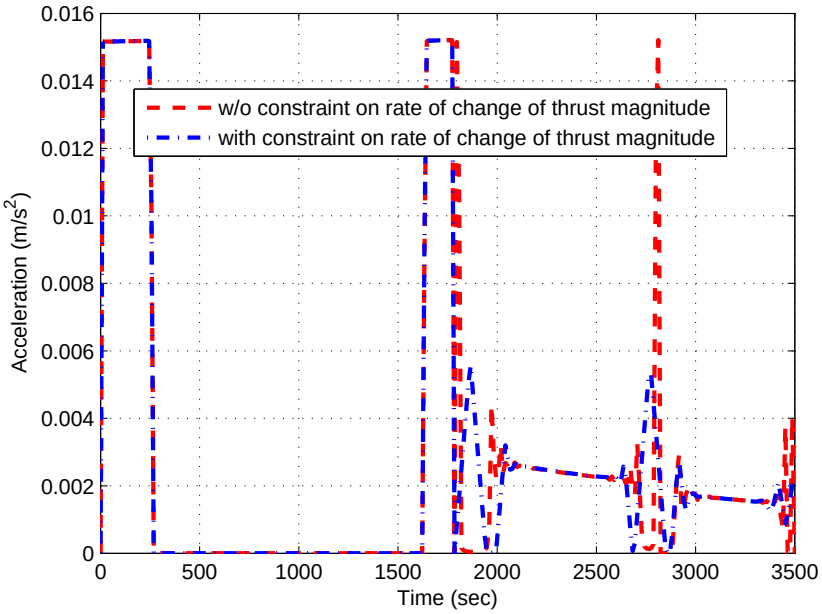

Figure 3.2 Effect of the constraints on the rate of change of the thrust vector in rendezvous and docking with a target spacecraft in an elliptic orbit with $e = 0.5$ and perigee altitude of 370 km.

3.4.2 Far-field Rendezvous Phase

Consider that the chaser is initially 100 km behind and 100 km below the target, and the initial relative velocity is [1 0 0.5] m/s in the LVLH frame. Maximum thrust T_{max} of 831 N is given for the chaser, generating thrust acceleration of around 0.6 m/s^2. The target is in an elliptic orbit with $e = 0.5$, and located in the position with true anomaly $\nu = 5$ deg when $t = 0$. The objective is to move the chaser to be 5 km behind the target at $t_f = 1800$ sec.

For this scenario, the dynamics between the chaser and the target can never be approximated by a linear model due to the significant difference in their altitudes. So it becomes a nonlinear problem, such as the nonlinearity in the dynamic equation of the chaser. However, this problem can be solved by solving a sequence of SOCP problems each of which has linear dynamic equation, linear objective, and second-order cone constraints. The final converged solution including thrust profile and trajectory is shown in

Figure 3.3 where '1' in the thrust profile represents the full thrust T_{max}. The solution from software GPOPS is also included in the figure, and the highly coincidence between the two solutions verifies the optimality of the solution from the SOCP method, which is further seen in the velocity components profile in Figure 3.4.

It is important to note that the solution obtained from GPOPS has only 36 nodes after two mesh refinement, which is the reason for the non-vertical transition from full thrust to zero in the thrust profile in Figure 3.3. The SOCP method uses 200 uniform nodes to discretize the problem, which is much more than that for GPOPS. However, GPOPS spends 276.36 sec to find the solution, while SOCP method needs only 5.01 sec to find the converged solution after 9 iterations. When the initial relative position between the chaser and the target is closer, such as in the near-field rendezvous, proximity and docking phase, less iterations are usually needed, and thus less time to find a converged solution.

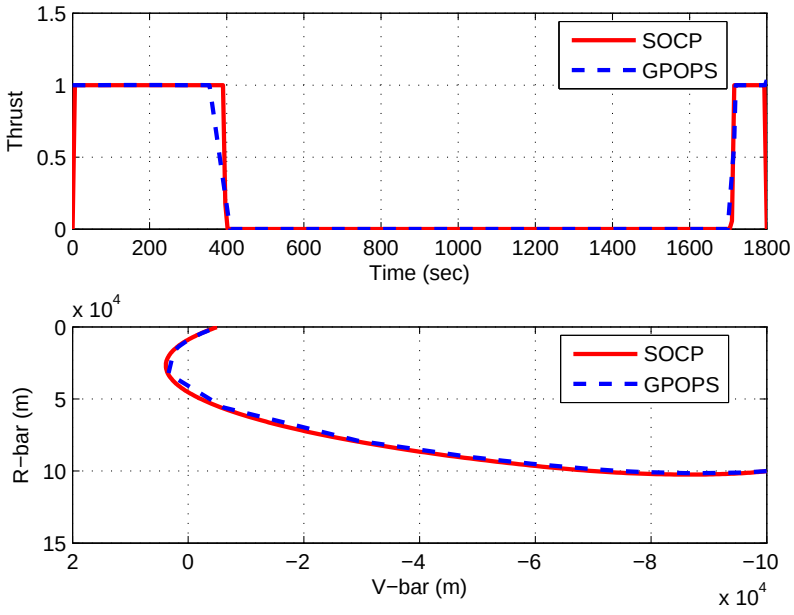

Figure 3.3 Thrust profile and relative trajectory in far-field rendezvous phase with initial relative position [-100, 0, 100] km and final relative position [-5, 0, 0] km in LVLH frame; target is in an elliptic orbit with $e = 0.5$.

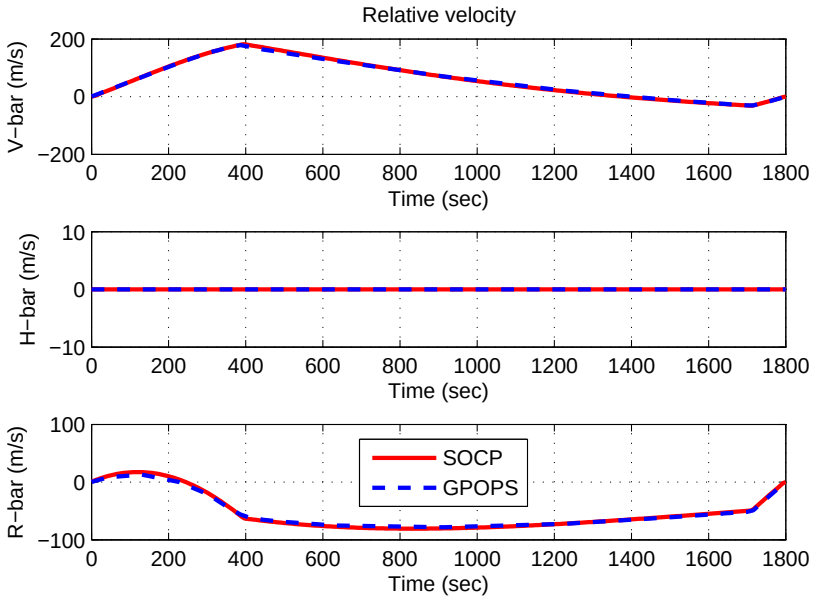

Figure 3.4 Relative velocity components in LVLH frame.

3.4.3 Near-field Rendezvous, Proximity and Docking Phase

In this phase, the chaser is controlled to move from a few kilometers away from the target to finally approach and dock with the target, with maximum thrust of 21 N or acceleration of about 0.015 m/s^2. Similar to the far-field rendezvous phase, it is necessary to check the optimality of solution obtained from SOCP method. Nevertheless, GPOPS is unable to get a converged solution when there is approach cone constraint, which is illustrated in Figure 3.5.

It is seen in Figure 3.5 that the solution from GPOPS does not completely satisfy the approach cone constraint and the thrust fluctuates a lot. So GPOPS can not help verify the optimality of the solution from the SOCP method. But at least a couple of phenomena could be observed from the GPOPS solution, which are that the chaser first move to the boundary of the cone and then try to move along it, and intermediate thrust is used for the chaser within the cone. Based on the solution from the SOCP method, the chaser also uses the same strategy for minimum fuel consumption. The thrust oscillation in the entrance and end of the cone can be eliminated if we add additional constraint

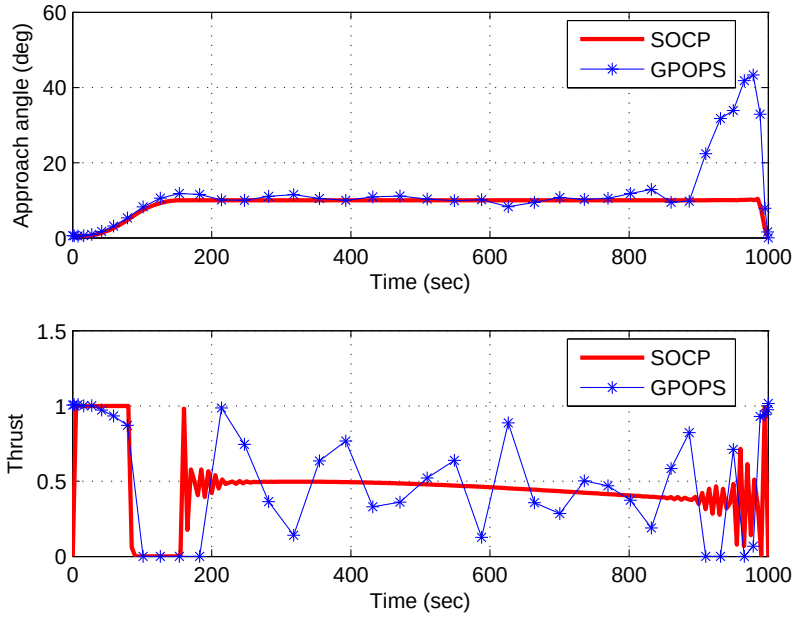

Figure 3.5 Approach cone and thrust profile in the proximity and docking phase with target in an elliptic orbit of $e = 0.5$, initial relative position is [200, 0, -2] m, initial relative velocity is [0.5, 0, 0.06] m/s, and approach cone constraint has a cone of half angle 10 deg.

on change rate of the thrust magnitude, which will be seen in the following simulation results. Both circular orbit and elliptic orbit will be considered to demonstrate the effectiveness of the SOCP method to the rendezvous and proximity operations.

Circular Orbit Let the chaser be 5 km ahead and 200 m above the target, which means the initial relative position between the two vehicles is [5000, 0, -200] m, and assume the initial relative velocity is [0.5, 0, 0.06] m/s. The constraints include:

1. Terminal constraint: At $t_f = 3000$ sec, the chaser has the same position and velocity with the target.

2. Interior point constraint: At $t_1 = 1800$ sec, the chaser arrives at 200 m ahead of the target along the V-bar axis, which is chosen as the docking axis, with relative velocity less than 0.2 m/s. This requirement is also called the *acquisition of docking*

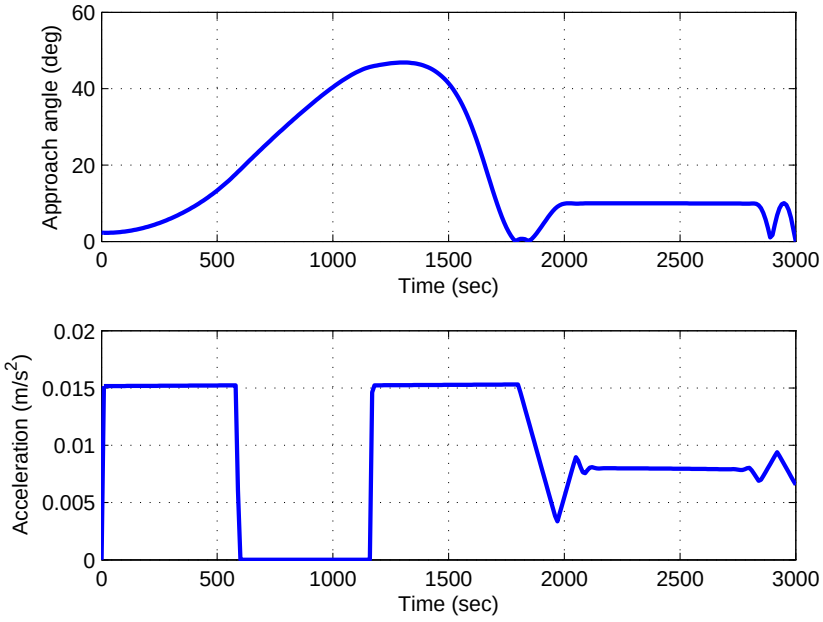

Figure 3.6 Approach cone with the docking axis and acceleration profile, the target is in a circular orbit with perigee altitude of 370 km.

axis (ADA).

3. Approach corridor constraint: Once within 200 m to the target, the chaser should stay inside an approach corridor which is defined as a cone with half angle of 10 deg.

4. Thrust direction constraint: From t_1 to $t_2 = 2520$ sec, the thrust plume must be 60 deg away from the target, while the angle is decreased to 89 deg for $t \in (t_2, t_f]$.

5. Change rate of thrust magnitude constraint: It is constrained to be less than 0.1 N/s for $t \in [t_1, t_2]$, and less than 0.05 N/s for $t \in (t_2, t_f]$.

The simulation results are shown in Figure 3.6–3.9. The constraints on approach cone and change rate of thrust magnitude for the last 200 m are satisfied, as seen in Figure 3.6, while Figure 3.7 illustrates the thrust direction constraint is also successfully enforced.

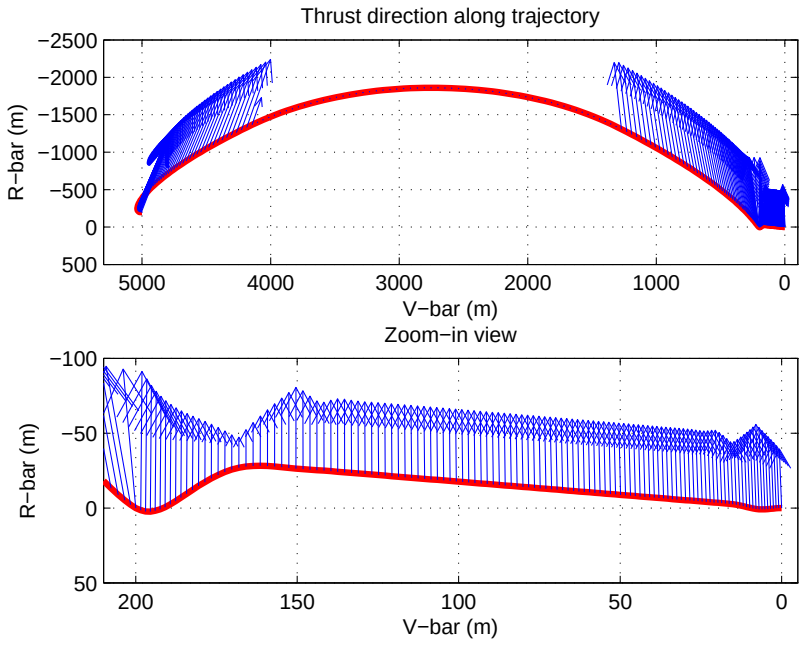

Figure 3.7 Trajectory plus thrust direction and the zoom-in view trajectory of the last 200 m, the target is in a circular orbit.

Before entering the approach cone, the chaser applies bang-band control which is to first increase the relative velocity with full thrust, then propagate with zero thrust, and finally brake with full thrust in order to have relative velocity less than 0.2 m/s when it is 200 m ahead of the target, which is shown in the top subplot of Figure 3.8. Its bottom subplot tells us that $\| T \| = \eta$ which is very important to ensure the equivalence between the relaxed problem and the original problem.

For the last 200 m, Figure 3.9 gives the detailed information on how the chaser moves within the cone to dock with the target. After the chaser is 200 m ahead of the target, almost vertical thrust perpendicular to the docking axis is applied to raise the chaser's altitude to move toward the boundary of the cone, which is seen from the increase of the approach angle for $t \in (1800, 2020)$ sec in the middle subplot of Figure 3.9. During this period, the relative velocity z component first increases in the negative R-bar direction to speed up, then decreases by using less thrust, and further decreases to finally have a small value in the positive R-bar direction. Due to the altitude increase of the chaser, its

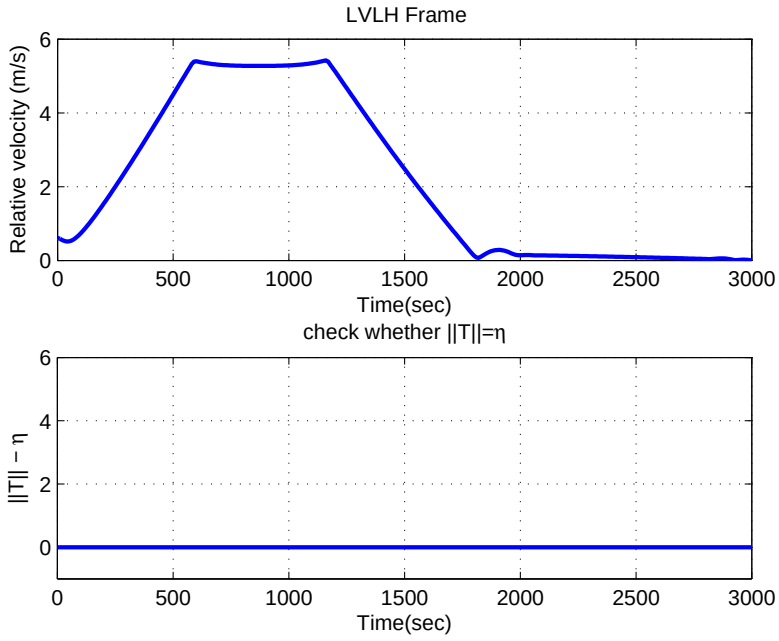

Figure 3.8 Top subplot: Magnitude of relative velocity in the LVLH frame; Bottom subplot: Check the relaxation condition $\| T \| = \eta$.

velocity along the V-bar direction is reduced, which makes the relative velocity between the two vehicles along the V-bar direction increased, that is to say the chaser moves faster toward the target. See the bottom subplot in Figure 3.9 for details.

Once the chaser is on the boundary of the cone, it keeps moving along the boundary with proper relative velocity in the positive R-bar direction, which is achieved by almost constant intermediate thrust shown in the top subplot of Figure 3.9. Since the altitude of the chaser is becoming smaller and smaller as it moves along the boundary, its velocity in the V-bar direction increases, resulting in the decrease in relative velocity along that direction. When the chaser is around 15 m to the target, or starting at $t = 2840$ sec, it starts to move away from the boundary by using less thrust and then slightly increase its speed to decrease the relative speed in the V-bar direction, during which the chaser will move back to the boundary again. This procedure is repeated one more to null the relative velocity, but still keeps the chaser to move within the cone. This phenomenon is not very noticeable in Figure 3.9, but it will be very easy to notice for the following

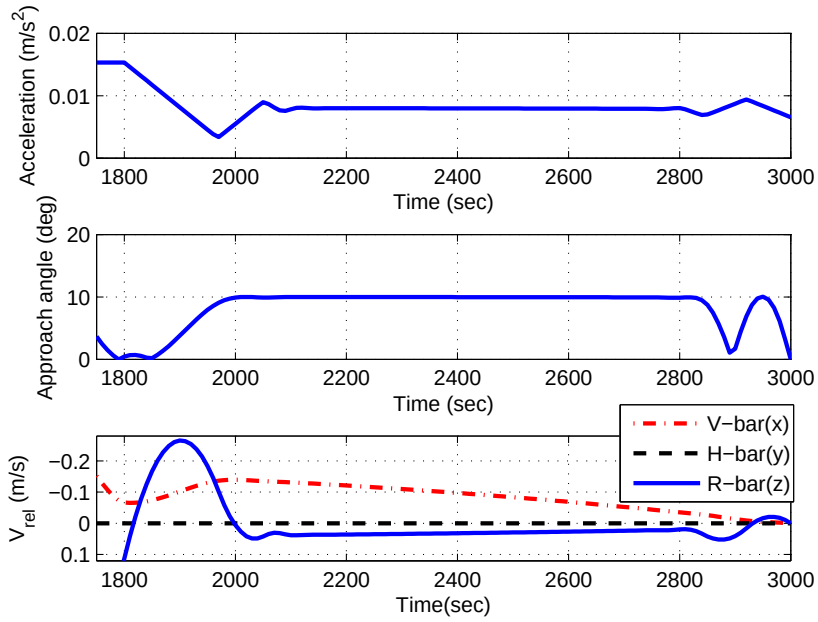

Figure 3.9 Acceleration, approach angle, and relative velocity within the last 200 m for the target in a circular orbit.

case with target in an elliptic orbit.

Elliptic Orbit The chaser is initially located 5 km behind and 500 m below the target which has true anomaly of 5 deg in an elliptic orbit with perigee altitude of 370 km and eccentricity $e = 0.5$. The initial relative velocity between them is [-0.8, 0, 0.1] m/s. All the requirements are stated as follows:

1. Terminal constraint: At $t_f = 3500$ sec, both the chaser and the target has the same position and velocity.

2. Interior point constraint: At $t_1 = 1800$ sec, the chaser arrives at 200 m ahead of the target along the V-bar axis, which is chosen as the docking axis, with relative velocity less than 0.2 m/s.

3. Approach corridor constraint: The corridor is defined to be the same cone as before with half angle of 10 deg.

4. Thrust direction constraint: From t_1 to $t_2 = 2820$ sec, the thrust plume must be 60 deg away from the target, while the angle is decreased to 89 deg for $t \in (t_2, t_f]$.

5. Change rate of thrust magnitude constraint: It is constrained to be less than 0.1 N/s for $t \in [t_1, t_2]$, and less than 0.05 N/s for $t \in (t_2, t_f]$.

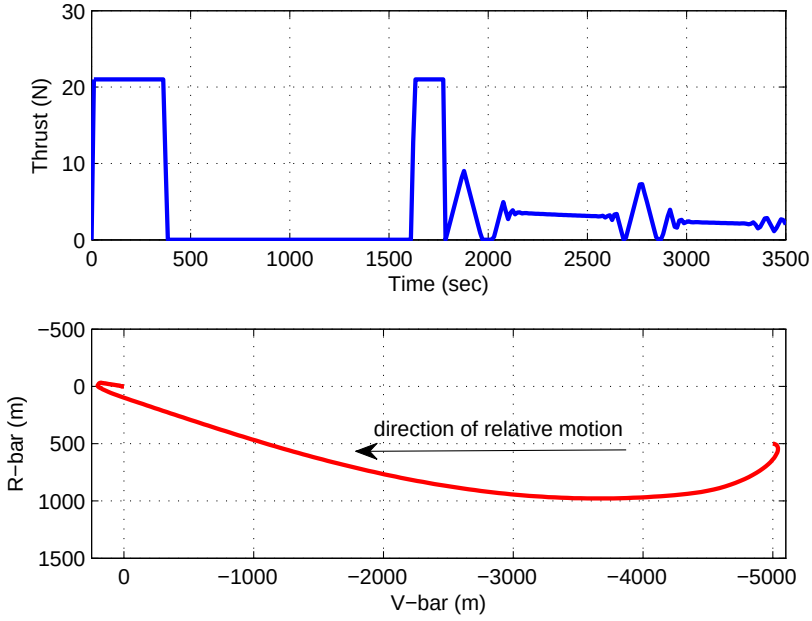

Figure 3.10 Thrust magnitude and trajectory for the whole process for the target in an elliptic orbit with $e = 0.5$.

The thrust magnitude and relative trajectory are plotted in Fig. 3.10. Note that the constraints from 3-5 described above are only enforced when the chaser is within the corridor. So the control profile is typical bang-bang control, as seen the top plot of Fig. 3.10, when there are only terminal constraint and an inequality constraint on limiting the maximum magnitude of norm of the controls. When all the constraints including those from 3-5 are included within the approach corridor, intermediate thrust is used by the chaser to satisfy all the constraints and have minimum fuel cost.

In Fig. 3.11, the top plot shows the trajectory within the approach corridor along with the thrust direction. It is interesting to notice that the chaser moves along the

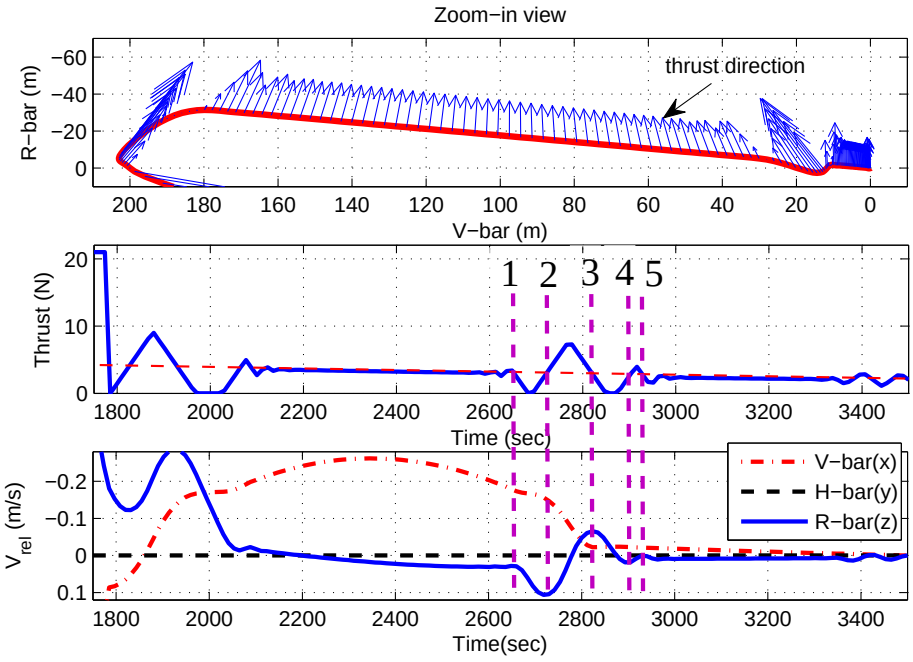

Figure 3.11 Trajectory, thrust magnitude, and relative velocity within the last 200 m for the target in an elliptic orbit with $e = 0.5$.

boundary of the corridor for most of the time. Right after the acquisition of docking axis (ADA), the chaser starts to first increase its thrust in the negative R-bar direction to move towards the boundary of the corridor, which is seen by the increase of relative velocity in the negative R-bar direction in the bottom plot of Fig. 3.11. At the same time, the thrust right after the ADA has component opposite to the direction of the orbital motion (or in the negative V-bar direction), which reduces the velocity of the chaser in the direction of the orbital motion so that the chaser accelerates towards the target, as shown in the bottom plot of Fig. 3.11. Then the chaser decreases its thrust to finally reach the boundary. After that, almost constant thrust perpendicular to the trajectory is used to maintain the motion along the boundary.

When the chaser is about 30 m to the target, it starts to prepare for the final docking by varying its thrust. There are five vertical lines in Fig. 3.11 between the first two of which the chaser uses less thrust, which is not enough to keep the motion along the boundary, so that it leaves the boundary as a result of the increase of the relative velocity

in the R-bar direction. When there is enough space between the chaser and the boundary, it is seen between line 2 and line 3 that more thrust in the V-bar direction is used to decrease the relative velocity between them. Meanwhile, the chaser will move back towards the boundary because the thrust has large enough component in the negative R-bar direction. What is happened in line 3-4 and line 4-5 repeats the previous process to further decrease the relative velocity in the negative V-bar direction. Finally, it should be pointed out that the middle plot of Fig. 3.11 illustrates that in the end similar thrust profile is used to make sure the relative velocity and position between the chaser and that target are zero at t_f.

CHAPTER 4. PERTURBATIONS

4.1 Introduction

As mentioned in Chapter 3, much of the rendezvous problems were based on the Clohessy-Wiltshire equations [5] which are linear and time-invariant differential equations describing the proximity relative motion of a chaser spacecraft with respect to a target spacecraft in a circular orbit. Linearized relative model was later extended to be valid for any arbitrary elliptic orbit and its analytic state matrix can be found [8], which enables the application in terminal rendezvous. See Ref. [7] for a summary of it. Optimal rendezvous problem in general Keplerian orbit with bounded-thrust can be also found in Ref. [6]. Furthermore, due to the existence of external perturbations to all satellites in reality, a set of linearized equations, incorporating the effect of J_2 perturbation, were developed for circular reference orbit [13]. The model was used to study the rendezvous maneuver for multiple spacecraft under the influence of J_2 disturbance in Ref. [14].

Despite the progress in deriving linearized relative-motion models on circular or elliptic orbit, and the attempt to include the J_2 effect, the prevalent work that can be found in literature is still rather limited for complex realistic RPO applications. First, all the models are linearized, implying that they are only approximations for the real relative motion and the accuracy will suffer to the case when two vehicles are not sufficiently close. Second, the constraints considered are very simple, such as only terminal conditions for the terminal rendezvous problem. When there are more constraints, it is usually impossible to derive an analytic solution for the relative motion. A practical

RPO problem is often constrained by a number of additional inequality trajectory constraints and interior-point constraints such as those on acquisition of docking axis point, relative velocity [10], approach corridor for docking, plume impingement inhibition [9], and keep-out zone. The presence of these practical constraints and the need to optimize the fuel-expenditure make an RPO problem a highly constrained and nonlinear optimal control problem. Third, while a majority of available studies are based on impulsive maneuver assumption to simplify the problem, the RPO maneuvers, particularly in the terminal phase, use small thrusters and the maneuvers are finite-time burns. Such difference cannot be overlooked if high fidelity is required, and the problem must be solved as finite-time-burn problem when it comes to guidance solution. Finally, other sources of perturbations in an RPO problem such as atmospheric drag may need to be incorporated in the solution. The methodology must be readily able to accommodate such needs.

For the highly constrained realistic RPO problem analyzed in Chapter 3, this chapter is an extension to incorporate perturbations in the RPO problem. The equation of two-body motion (3.1) does not consider any perturbations existing in real-world. In order to have more precise solution for the RPO, a more accurate model plays a crucial role for that, which can be written as [11]

$$\ddot{\boldsymbol{r}} = -\frac{\mu}{r^3}\boldsymbol{r} + \frac{\boldsymbol{T}}{m} + \boldsymbol{a}_{\mathrm{p}} \tag{4.1}$$

where $\boldsymbol{a}_{\mathrm{p}}$ is the sum of all perturbed acceleration caused by other forces. The value and form of $\boldsymbol{a}_{\mathrm{p}}$ depend on the type of perturbing sources which include Earth gravity harmonics, atmospheric drag, third-body attractions, solar radiation pressure, tides, etc. In this dissertation, we only consider the first two perturbations, which are discussed in Section 4.2 and 4.3 respectively. Inclusion of other perturbation sources is straightforward. The purpose is to show that the method proposed in Chapter 3 is able to solve the problem with perturbations. The discussion followed can also be found in Ref. [52].

4.2 Harmonic Gravity

Earth gravitational harmonics are due to its non-spherical shape, which can be broken down into zonal and tesseral harmonics. The latter attempts to model specific regions on the Earth departing from a perfect sphere, while the former accounts for the Earth's oblateness. Since the tesseral harmonics are much smaller, here we only consider the zonal harmonics in which J_2 is the largest term and represents the most of the Earth's gravitational departure from a perfect sphere. For instance, the value of J_2 is about 400 times larger than J_3, see Ref. [11] for more details. So, it has good accuracy by simply including J_2 effect to represent the Earth gravity harmonics.

To express the gravitational acceleration from J_2, a standard local-vertical local-horizontal (LVLH) frame centered at the target spacecraft is formed as that the z-axis pointing to the Earth is known as local-vertical axis or R-bar axis, the x-axis is in the plane of the osculating orbit and is perpendicular to the z-axis in the direction of the orbital motion of the target. The direction of the x-axis is also called as the local-horizontal axis or V-bar axis. The y axis, or H-bar axis, completes a right-hand coordinate system. Let $\boldsymbol{i}$, $\boldsymbol{j}$ and $\boldsymbol{k}$ be the unit vectors of the coordinate system. The gravitational acceleration due to J_2 is given as [11]

$$\boldsymbol{a}_{J_2} = a_V \boldsymbol{i} + a_H \boldsymbol{j} + a_R \boldsymbol{k} \tag{4.2}$$

where a_V, a_H, a_R are the gravitational components along V-bar, H-bar, R-bar axis, respectively and

$$\begin{aligned} a_V &= -\frac{3}{2}\frac{\mu}{r^2}(\frac{R_0}{r})^2 J_2 \sin^2 i \sin(2\theta) \\ a_H &= \frac{3}{2}\frac{\mu}{r^2}(\frac{R_0}{r})^2 J_2 \sin(2i) \sin\theta \\ a_R &= \frac{3}{2}\frac{\mu}{r^2}(\frac{R_0}{r})^2 J_2 (1 - 3\sin^2 i \sin^2\theta) \end{aligned} \tag{4.3}$$

where $J_2 = 1.08263 * 10^{-3}$, i is the inclination of the osculating orbit, and θ is the sum of the argument of perigee and the true anomaly of the osculating orbit. Note that i

and θ are functions of $\boldsymbol{r}$ and $\boldsymbol{V}$ in the presence of non-Newtonian gravity. The dynamic equation with J_2 perturbation becomes

$$\ddot{\boldsymbol{r}} = -\frac{\mu}{r^3}\boldsymbol{r} + a_V\boldsymbol{i} + a_H\boldsymbol{j} + a_R\boldsymbol{k} + \frac{\boldsymbol{T}}{m} \tag{4.4}$$

In order to express equation (4.4) in the form of (3.56), we make use of the following

$$\boldsymbol{i} = \boldsymbol{V}_h/V_h, \quad \boldsymbol{j} = \frac{\boldsymbol{r}\times\boldsymbol{V}}{|\boldsymbol{r}\times\boldsymbol{V}|}, \quad \boldsymbol{k} = \frac{-\boldsymbol{r}}{r} \tag{4.5}$$

where $\boldsymbol{V}_h$ the horizontal component of the velocity vector

$$\boldsymbol{V}_h = \boldsymbol{V} - (\boldsymbol{V}^T\boldsymbol{r}/r^2)\boldsymbol{r} \tag{4.6}$$

Equation (4.4) can be rewritten as

$$\ddot{\boldsymbol{r}} = -(\frac{\mu}{r^3} + \frac{a_V}{V_h}\frac{\boldsymbol{V}^T\boldsymbol{r}}{r^2} + \frac{a_R}{r})\boldsymbol{r} + \frac{a_V}{V_h}\boldsymbol{V} + a_H\boldsymbol{j} + \frac{\boldsymbol{T}}{m} \tag{4.7}$$

Substituting (4.5) to the above equation and applying normalization, we have

$$\dot{\boldsymbol{V}} = (-1/r^3 + a_1)\boldsymbol{r} + a_2\boldsymbol{V} + \frac{\boldsymbol{T}}{m} + \boldsymbol{a}_0 \tag{4.8}$$

where

$$\begin{aligned} a_1 &= \frac{3}{2}J_2\frac{\boldsymbol{V}^T\boldsymbol{r}}{r^6V_h}\sin^2 i\sin(2\theta) - \frac{3}{2}J_2\frac{1}{r^5}(1-3\sin^2 i\sin^2\theta) \\ a_2 &= -\frac{3}{2}J_2\frac{1}{r^4V_h}\sin^2 i\sin(2\theta) \\ \boldsymbol{a}_0 &= \frac{3}{2}J_2\frac{1}{r^4}\sin(2i)\sin\theta\ \boldsymbol{j} \end{aligned} \tag{4.9}$$

Similar to equation (3.56), we have the following dynamic equation

$$\dot{\boldsymbol{x}} = \bar{A}(\boldsymbol{x})\boldsymbol{x} + \bar{B}\boldsymbol{u} + \bar{b} \tag{4.10}$$

with

$$\bar{A}(\boldsymbol{x}) = \begin{bmatrix} 0_{3\times3} & I_{3\times3} & 0_{3\times1} \\ (-\frac{1}{r^3}+a_1)I_{3\times3} & a_2I_{3\times3} & 0_{3\times1} \\ 0_{1\times3} & 0_{1\times3} & 0 \end{bmatrix},\ \bar{B} = \begin{bmatrix} 0_{3\times3} & 0_{3\times1} \\ I_{3\times3} & 0_{3\times1} \\ 0_{1\times3} & -1/v_{ex} \end{bmatrix},\ \bar{b} = \begin{bmatrix} 0_{3\times1} \\ \boldsymbol{a}_0 \\ 0 \end{bmatrix} \tag{4.11}$$

Unlike the matrix $A(r)$ in (3.56) which only depends on the norm of $\boldsymbol{r}$ vector, the matrix $\bar{A}(\boldsymbol{x})$ here is dependent on both $\boldsymbol{r}$ and $\boldsymbol{V}$ as seen in the definitions of a_1 and a_2 in (4.9).

4.3 Atmospheric Drag

The orbital decay of any low-altitude satellite is due to atmospheric drag which is a non-conservative force, takes energy from the orbit and decreases the semi-major axis of the orbit. So the chaser spacecraft also faces the atmospheric drag computed as

$$\boldsymbol{a}_{drag} = -\frac{1}{2}\frac{C_D S}{m}\rho V \boldsymbol{V} \tag{4.12}$$

where C_D is the drag coefficient taking values about 2.2 for a flat plate model, S the cross-sectional area of the spacecraft normal to its velocity vector $\boldsymbol{V}$, and ρ the atmospheric density which is perhaps the most difficult parameter to determine. The density is dependent on many factors such as solar flux, diurnal variations, seasonal variations, geomagnetic activity, etc. See Ref. [12] for details.

Normalizing the drag acceleration (4.12) and adding it linearly to the state equation with perturbation from J_2 in (4.8), we have the same form of equation (4.10), but replace $\bar{A}(\boldsymbol{x})$ with

$$\tilde{A}(\boldsymbol{x}) = \begin{bmatrix} 0_{3\times3} & I_{3\times3} & 0_{3\times1} \\ (-\frac{1}{r^3} + a_1)I_{3\times3} & (a_2 + a_3)I_{3\times3} & 0_{3\times1} \\ 0_{1\times3} & 0_{1\times3} & 0 \end{bmatrix} \tag{4.13}$$

where

$$a_3 = -\frac{1}{2}\frac{C_D S}{m}\frac{R_0}{m_0}\rho V \tag{4.14}$$

The matrix $\tilde{A}(\boldsymbol{x})$ in (4.13) includes both perturbations from J_2 and the atmospheric drag. If only drag acceleration is considered, set $a_1 = 0,\ a_2 = 0,$ and $\boldsymbol{a}_0 = 0$.

4.4 Convergence

In this section, we will discuss the convergence of the successive approximation method to solve the problem in Chapter 3 with perturbations considered in the previous two sections. As what is discussed in Chapter 3, a complete and general proof

is not available when there are no perturbations. Nevertheless, some technical observations are made relevant to the convergence of the successive approximation method to the problem which is an extension to the problem considered in Chapter 3 by accounting for the perturbations from J_2 and atmospheric drag [52].

In Ref. [47] a nonlinear optimal control problem is considered where the system dynamic take the form of

$$\dot{\boldsymbol{x}} = A(\boldsymbol{x}) + B(\boldsymbol{x})\boldsymbol{u},\ \boldsymbol{x}(0) = \boldsymbol{x}_0 \tag{4.15}$$

with a quadratic performance index

$$\min J = \frac{1}{2}\boldsymbol{x}^T(t_f)F\boldsymbol{x}(t_f) + \frac{1}{2}\int_0^{t_f}(\boldsymbol{x}^T Q\boldsymbol{x} + \boldsymbol{u}^T R\boldsymbol{u})dt \tag{4.16}$$

Under the conditions of Lipschitz continuity on $A(\boldsymbol{x})$ and $B(\boldsymbol{x})$ and boundedness of the logarithmic norm of $A(\boldsymbol{x})$ and $B(\boldsymbol{x})$, Ref. [47] shows that the above problem can be approximated by a solving a sequence of linear-quadratic problems with the following linear, time-varying dynamic systems

$$\dot{\boldsymbol{x}}^{[k+1]} = A\left[\boldsymbol{x}^{[k]}(t)\right]\boldsymbol{x}^{[k+1]} + B\left[\boldsymbol{x}^{[k]}(t)\right]\boldsymbol{u}^{[k+1]},\ \boldsymbol{x}^{[k+1]}(0) = \boldsymbol{x}_0 \tag{4.17}$$

and

$$\min J = \frac{1}{2}\left(\boldsymbol{x}^{[k+1]}(t_f)\right)^T F\boldsymbol{x}^{[k+1]}(t_f) + \frac{1}{2}\int_0^{t_f}\left[\left(\boldsymbol{x}^{[k+1]}\right)^T Q\boldsymbol{x}^{[k+1]} + \left(\boldsymbol{u}^{[k+1]}\right)^T R\boldsymbol{u}^{[k+1]}\right]dt \tag{4.18}$$

In our problem $\tilde{B}$ is a constant matrix so it is trivially bounded. Make the following reasonable assumptions on the target orbit during the finite period $[t_0, t_f]$:

1. the altitude of the chaser is bounded: $1 < r_{min} \leq r \leq r_{max}$
2. the flight path angle ϕ of the chaser is bounded: $|\phi| \leq \phi_{max} < \pi/2$

We will show that the matrix $\tilde{A}(\boldsymbol{x})$ in our problem satisfies

$$\psi(\tilde{A}(\boldsymbol{x})) \leq \psi_0 \tag{4.19}$$

$$\|\tilde{A}(\boldsymbol{x}_1) - \tilde{A}(\boldsymbol{x}_2)\| \leq 2 \tag{4.20}$$

where ψ denotes the logarithmic norm of the matrix, and

$$\psi_0 = 1 - \frac{1}{r_{max}^3} + \frac{3}{2}J_2\left(2 + \sqrt{1 - \frac{1}{\cos^2\phi_{max}}}\right)$$

Let $\lambda_{max}(M)$ stands for the largest eigenvalue of the matrix M. By the definition of logarithmic norm, it can readily derived that

$$\psi(\tilde{A}(\boldsymbol{x})) = \lambda_{max}\left(\frac{\tilde{A}(\boldsymbol{x}) + \tilde{A}(\boldsymbol{x})^T}{2}\right) = 1 - \frac{1}{r^3} + a_1 \tag{4.21}$$

where a_1 is

$$a_1 = \frac{3}{2}J_2\frac{1}{r^5}[\sin^2 i\ \sin(2u)\ \tan\phi + 3\sin^2 i\ \sin^2 u - 1] \tag{4.22}$$

Since $\tan^2\phi + 1 = 1/\cos^2\phi$, so

$$-\sqrt{1 - \frac{1}{\cos^2\phi_{max}}} \leq \tan\phi \leq \sqrt{1 - \frac{1}{\cos^2\phi_{max}}} \tag{4.23}$$

Using $-1 \leq 3\sin^2 i\ \sin^2 u - 1 \leq 2$, $r_{min} > 1$ and the above bounds on $\tan\phi$ in Eq. (4.22), a_1 satisfies

$$-\frac{3}{2}J_2\left(1 + \sqrt{1 - \frac{1}{\cos^2\phi_{max}}}\right) \leq a_1 \leq \frac{3}{2}J_2\left(2 + \sqrt{1 - \frac{1}{\cos^2\phi_{max}}}\right) \tag{4.24}$$

Based on Eq. (4.21), it is proven that $\psi(\tilde{A}(\boldsymbol{x})) \leq 1 - \frac{1}{r_{max}^3} + \frac{3}{2}J_2\left(2 + \sqrt{1 - \frac{1}{\cos^2\phi_{max}}}\right)$.

For inequality (4.20), we first compute $\|\tilde{A}(\boldsymbol{x}))\|$ which is given as

$$\|\tilde{A}(\boldsymbol{x}))\| = \sqrt{\lambda_{max}(\tilde{A}(\boldsymbol{x}))^T\tilde{A}(\boldsymbol{x}))} = \max(|-1/r^3 + a_1|, 1) \tag{4.25}$$

Since $|-1/r^3 + a_1| \leq \frac{1}{r^3} + |a_1| \leq \frac{1}{r_{min}^3} + \frac{3}{2}J_2\left(2 + \sqrt{1 - \frac{1}{\cos^2\phi_{max}}}\right)$, this is a quantity that is usually less than 1 for $r_{min} > 1$. So $\max(|-1/r^3 + a_1|, 1) = 1$ and

$$\|\tilde{A}(\boldsymbol{x}))\| = 1 \tag{4.26}$$

Then we have

$$\|\tilde{A}(\boldsymbol{x}_1)) - \tilde{A}(\boldsymbol{x}_2))\| \leq \|\tilde{A}(\boldsymbol{x}_1))\| + \|\tilde{A}(\boldsymbol{x}_2))\| \leq 2 \tag{4.27}$$

which proves the inequality (4.20).

Based on the conditions of a Lipschitz condition on $A(\boldsymbol{x})$ and bounded logarithmic norm of $A(\boldsymbol{x})$ (plus Lipschitz and boundedness conditions on $B(\boldsymbol{x})$ which are automatically satisfied in our case), Ref. [47] shows that for sufficiently small t_f (or $\boldsymbol{x}_0$) the successive solutions to the linear-quadratic (LQ) problems converge to that of the original problem. It is shown here that critical condition in Ref. [47] on the logarithmic norm of the $\tilde{A}$ matrix is met. If the Lipschitz condition on $A(\boldsymbol{x})$ in Ref. [47] is replaced by the condition in similar to that in Eq. (4.20), the same convergence proof there would remain valid. However, our problem is much more complex than an LQ problem, because of all the constraints. While a theoretical proof of convergence is not available, our extensive numerical experience has provided strong evidence to consistent convergence of the proposed successive approximation method in solving the RPO problem.

4.5 Numerical Results

In this section, the simulation results, obtained by the modeling toolbox YALMIP [53] and the MOSEK solver [28], of the problem described in Chapter 3 will be shown to verify the effectiveness of the method to incorporate the perturbations from J_2 and atmospheric drag.

For the rendezvous and proximity operations with perturbation from J_2, consider the target to be in a circular orbit with altitude of 400 km, inclination of 51.6 deg, and right ascension of ascending node of 100 deg. The target is initially at a position that is 85 deg away from the right ascension of ascending node. The chaser having initial mass of 1385 kg is located 5 km behind and 500 m below the target with nonzero relative velocity of [0.7, 0, 0.5] m/s in the LVLH frame, and subjects to the perturbation from J_2. The maximum magnitude of thrust vector for the chaser is given as 84 N which gives an acceleration of 0.06 m/s^2. All constraints are given as follows:

1. The chaser is required to dock with the target with the same final position and

velocity at total given flight time $t_f = 4000$ sec. At $t_1 = 2000$ sec, the chaser arrives at 200 m in front of the target along V-bar and the relative velocity between them is less than 0.2 m/s.

2. Since $t_1 = 2000$ sec, the chaser needs to be inside the final approach corridor which is a cone with half angle of 15 deg.

3. Within the corridor, for safety consideration, when $t \in (2000, 3200]$ sec, the plume is required to be at least 60 deg away from the target and the inertial relative velocity is less than 0.3 m/s, while those values become 89 deg and 0.1 m/s respectively when $t \in (3200, 4000]$ sec.

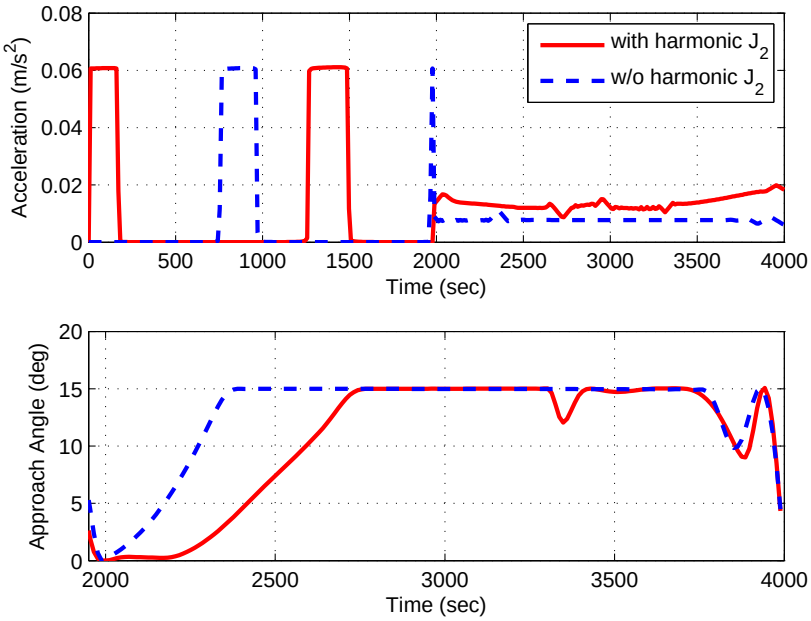

Figure 4.1 Top subplot: the thrust acceleration profile with the red curve including perturbation from J_2. Bottom subplot: the approach angle when the chaser is within the approach corridor since 2000 sec (or the last 200 m). The target is in a circular orbit with altitude of 400 km.

The simulation results are shown in Fig. 4.1–4.4 in which all blue curves, plotted for comparison, represent the results when there is no J_2 perturbation. Before the chaser

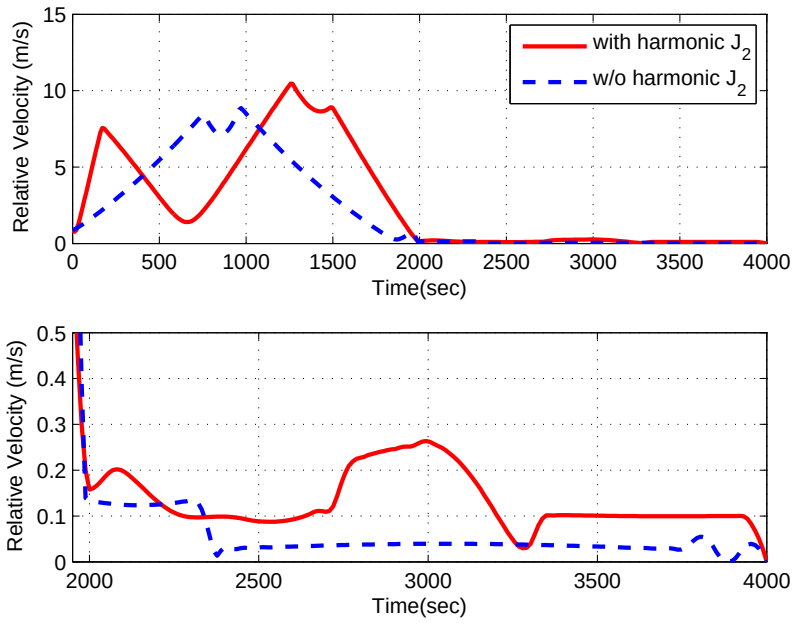

Figure 4.2 Top subplot: the magnitude of relative velocity in the LVLH frame. Bottom subplot: zoom in view on the magnitude of relative velocity since 2000 sec (or the last 200 m). The target is in a circular orbit with altitude of 400 km. The target is in a circular orbit with altitude of 400 km.

enters the approach corridor, the only constraint is the maximum magnitude of thrust, so the thrust is either full burn or coasting, as seen from the top plot of Fig. 4.1. However, the first burn does not occur until about $t = 730$ sec when there is no perturbation, and there is the second short burn for braking to satisfy the velocity requirement when the chaser is close to be 200 m ahead of the target. With consideration to J_2, the chaser has the first burn in the very beginning followed by another one in the midway, and uses a little bit thrust to brake right before it enters the corridor. So the thrust profile is totally different for the existence of J_2. In addition, the top two plots in Fig. 4.3 tells us that the H-bar or out of plane component of the relative trajectory in the LVLH frame is no longer zero when considering J_2, which is the same case for the trajectory inside the corridor shown in the bottom two plots of Fig. 4.3. Due to the existence of H-bar component, it is also implied that for fuel optimal objective there is no need to constrain the motion to be always in the orbital plane.

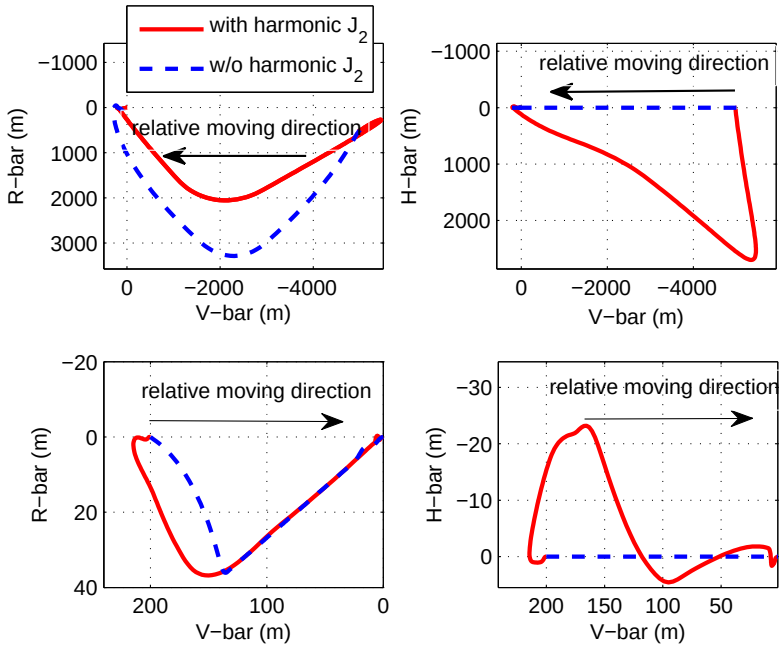

Figure 4.3 Top two subplots: the whole relative trajectory in the LVLH frame. Bottom two subplots: zoom in view on the relative trajectory since 2000 sec (or the last 200 m).

Within the corridor, the chaser tries to move along the boundary to save fuel as seen in the bottom plot of Fig. 4.1, with some temporarily leave away from the boundary for changing velocity. For the thrust, its magnitude is intermediate due to the inclusion of a variety of constraints. Also, it is larger than that when there is no J_2, which is understandable in practice. The direction of the thrust, plotted in Fig. 4.4, is not limited to be in the orbital plane, but has nonzero component in the H-bar direction, and satisfies the plume impingement inhibition.

In summary, the J_2 perturbation has a significant effect on the solution, as discussed above. So it is important to take J_2 perturbation into consideration in practice. Nevertheless, the main point here is that the method presented in Ref. [9] is applicable to rendezvous problem with perturbations. There is no difficulty for the algorithm to converge and it takes only 6 iterations or so.

Next, Let us consider the perturbation from atmospheric drag. From equation (4.12),

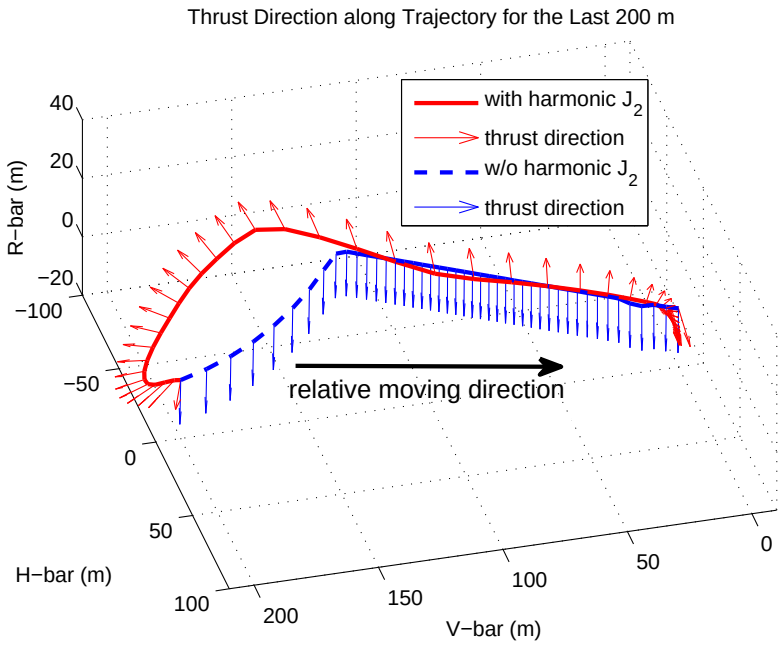

Figure 4.4 The relative trajectory in 3-dimension for the last 200 m with thrust direction along the trajectory. All thrust vectors are in unit length.

the atmospheric density ρ needs to be known. There are numerous models, either static or time-varying, to obtain the density, one of which is the Russian GOST model valid for altitude of 120-1500 km. The version GOST 25645.115-84 of the model will be used here, see Ref. [12] for details. The model accounts for the effects from solar flux, semiannual variation, and geomagnetic activity. Semiannual effect is ignored here. In order for the effect of drag perturbation to be more discernible, a lower circular orbit with altitude of 250 km is used. In addition, assume that there is extreme geomagnetic activity with $k_p = 9.0$ which is a quasi-logarithmic, worldwide average of geomagnetic activity below the auroral zones, and active solar activity with $\bar{F}_{10.7} = 240$ is taken into consideration. The drag coefficient C_D is chosen as 2.2, and the cross sectional areas is assumed to be a constant $S = 20$ m^2.

For the data given above, the atmospheric drag gives a disturbed acceleration of about 1.32×10^{-4} m/s^2, which effects on the thrust and approach angle are shown in Fig. 4.5. It is seen that little change is on the magnitude of thrust, while there is slight change

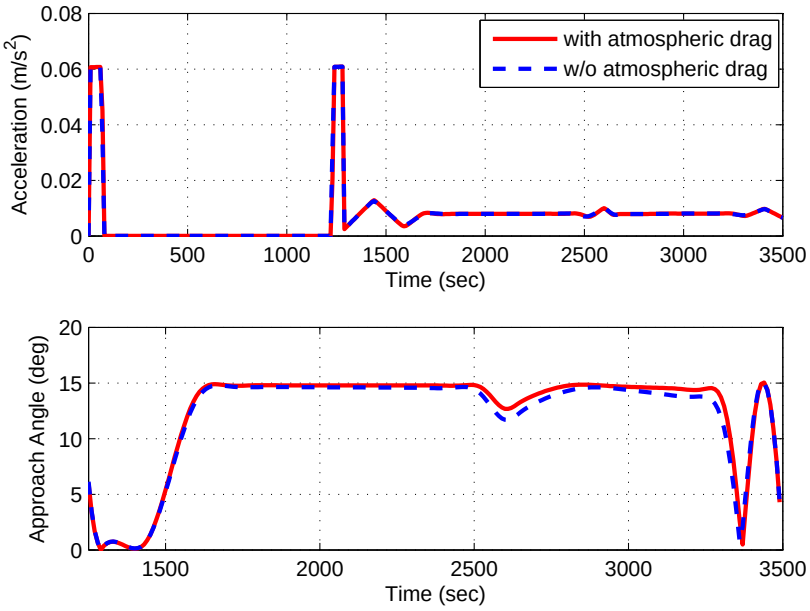

Figure 4.5 Top subplot: the thrust acceleration profile. Bottom subplot: the approach angle when the chaser is within the approach corridor. The target is in a circular orbit with altitude of 250 km. $t_f = 3500$ sec, $t_1 = 1300$ sec.

for the approach angle. The top two plots of Fig. 4.6 illustrate that before entering the approach corridor, the chaser's motion in the R-V bar plane is slightly affected by the atmospheric drag, but there is still no out of plane motion. When the chaser is inside the approach corridor, increased out of plane motion, even though very small, occurs under the influence of drag perturbation, as seen in the bottom-right plot in Fig. 4.6. Overall, atmospheric drag does have slight influence to the case considered here. When the chaser has less mass and smaller thrust, it is expected that the RPO will be more affected by the atmospheric drag.

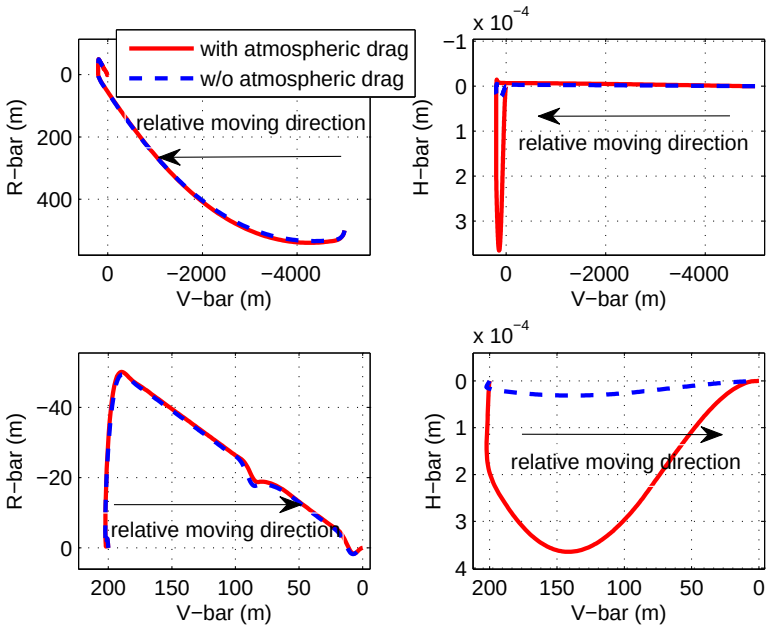

Figure 4.6 Top two subplots: the whole relative trajectory in the LVLH frame. Bottom two subplots: zoom in view on the relative trajectory inside the approach corridor. The target is in a circular orbit with altitude of 250 km.

CHAPTER 5. COLLISION AVOIDANCE

5.1 Introduction

Collision avoidance is practically important for satellites in orbit to avoid collision with space debris or other satellites. An immediate example is the RPO problem discussed in Chapter 3 which has a potential for collision during proximity operations. For example, when the chaser flies from behind the target to finally dock with the target by using the V-bar approach, the chaser may collide with the appendages from the target such as solar panel. Other areas could include launching a vehicle into orbit and orbital transfer where collision avoidance is significant.

The constraints from collision avoidance are commonplace in aerospace problems and robot path planning, and it may have different names in different situations, such as no-fly-zone constraint or obstacle avoidance. The only efforts in the literature that attempt to address such non-convex constraints for application of convex optimization are within the context of linear programming (thus applicable only to linear problems). For polygon avoidance region, Ref. [15] proposes to represent the collision avoidance constraint with a set of linear equations including binary variables. For example, it needs 4 binary variables in each time step for a rectangle avoidance region, producing 1200 binary variables if 300 time steps are used in a problem. To alleviate the greatly increased computational time caused by the many binary variables, a time-step grouping technique [15] can be used to reduce the number of binary variables needed to be dealt with. While in principle a non-polygon avoidance region may be approximated by a polygon and then treated by

the same approach as in Ref. [15], the dimension of the problem would be significantly higher for reasonably accurate constraint representation. Extensions to 3-dimensional constraints would result in a prohibitive dimension of the problem. In Refs. [16, 17], a circular collision avoidance region in a 2-dimensional plane is replaced by the half space defined by a single line tangent to the boundary of the circle and rotating at a constant angular rate. There is only one linear inequality constraint at each time step without involving binary variables. However, the initial location of the tangent line and the constant rotation rate are two critical parameters that need to be determined in each application. But the knowledge of what constitutes appropriate choices is not available before a solution is found. So trial and error are inevitable. Yet inappropriate choices could lead to infeasibility of this linear inequality constraint. When it works, it tends to produce more conservative trajectory because of the limitation of the constant rotation rate of the line. Extension to non-circular regions would be difficult, if not impossible, because the constant rotation-rate assumption would be challenged even more.

Inclusion of the constraints poses a fundamental challenge to the SOCP-based methodology because the constraints, which can actually be viewed as concave inequality constraints, are non-convex. In this dissertation, each concave inequality constraint is approached by a successive solution process where a sequence of convex problems are solved. Each of the concave inequality constraints is linearized about the last solution in the process. As a result, each of the successive problems is a convex problem that can be solved by SOCP. While similar ideas for handling nonlinearity in optimization problems have long been tried [54], but no convergence results are available and the performance may be poor [55]. However, it is shown in this disseration that the concavity of the constraints results in a fundamental property of guaranteed feasibility to the original constraints by the solutions of the successive problems. Further analysis establishes the existence of the successive solutions, and the equivalence of a solution of the original problem to the converged successive solution. Based on these findings, the convergence of the succes-

sive solutions to a solution of the original problem, at least a local optimal solution, is rigorously proven under reasonable conditions. Moreover, the converged solution by the proposed approach will not have any conservativeness in satisfying the original concave constraints.

5.2 Problem Formulation

For the RPO problem, during proximity operations around the target vehicle, the chaser should make sure that its maneuvering trajectory does not get too close to the target vehicle to avoid possible collision. The requirement is usually imposed as a constraint for keep-out zone centered at the target vehicle in the LVLH frame. In the near-field rendezvous phase, the chaser, initially located behind the target, is trying to approach the target and arrives in front of the target for a V-bar approach. Fig. 5.1 shows the scenario where the keep-out zone is modeled as a sphere of radius d centered at the target vehicle in the LVLH frame. Denote the position of the chaser and target be $\bar{\boldsymbol{r}}$ and $\bar{\boldsymbol{r}}_t$ respectively in the LVLH frame. Then the problem (3.55)–(3.62) has one more inequality trajectory constraint for collision avoidance which is expressed as

$$\bar{r}_x^2 + \bar{r}_y^2 + \bar{r}_z^2 \geq d^2 \tag{5.1}$$

where $\bar{r}_x$, $\bar{r}_y$ and $\bar{r}_z$ are the components of the relative position between the chaser and the target in the LVLH frame, i.e.,

$$\bar{\boldsymbol{r}} - \bar{\boldsymbol{r}}_t = \bar{r}_x \boldsymbol{i} + \bar{r}_y \boldsymbol{j} + \bar{r}_z \boldsymbol{k} \tag{5.2}$$

A more general and practical keep-out zone in the RPO problem is typically an ellipsoid where the chaser's trajectory is prohibited. Figure 5.2 illustrates such a scenario in 2D. If the ellipsoid has semi-principle axes of a, b and c along the x (V-bar), y (H-bar) and z (R-bar) axis respectively, the constraint can be written as

$$\frac{\bar{r}_x^2}{a^2} + \frac{\bar{r}_y^2}{b^2} + \frac{\bar{r}_z^2}{c^2} \geq 1 \tag{5.3}$$

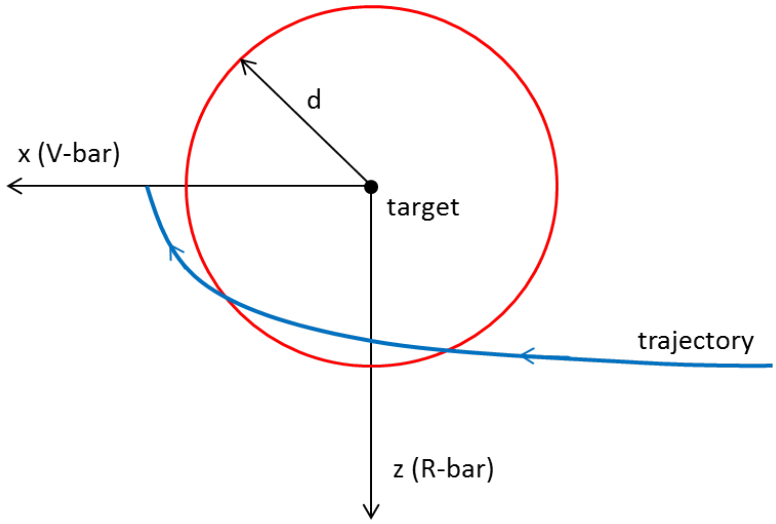

Figure 5.1 Circular keep-out zone for collision avoidance in 2-dimension (2D)

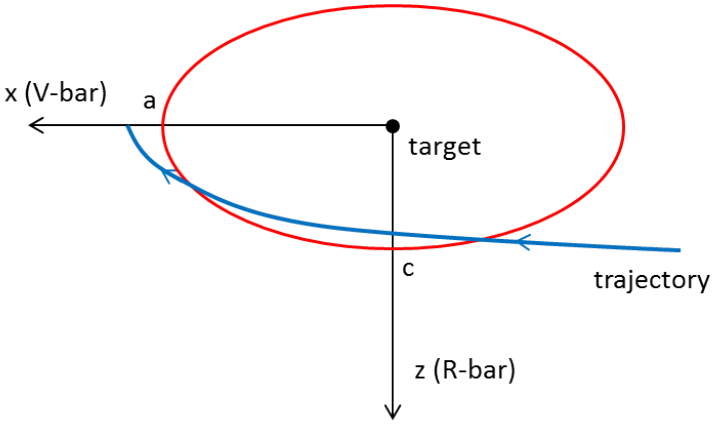

Figure 5.2 Elliptic keep-out zone for collision avoidance in 2D

It is seen that both Eq. (5.1) and (5.3) are expressed in the LVLH frame, while the states and controls in problem (3.55)–(3.62) are all with respect to the GEI frame. Therefore, it is necessary to rewrite the Eq. (5.1) and (5.3) in the GEI frame. Based on the transformation matrix (2.30) in Chapter 2, we can express the relative position vector in Eq. (5.2) in the GEI frame as

$$\boldsymbol{r} - \bar{\boldsymbol{r}}_t = [\bar{r}_x \quad \bar{r}_y \quad \bar{r}_z] \begin{bmatrix} \boldsymbol{i} \\ \boldsymbol{j} \\ \boldsymbol{k} \end{bmatrix} = [\bar{r}_x \quad \bar{r}_y \quad \bar{r}_z] M^{L/G} \begin{bmatrix} \mathbf{I} \\ \boldsymbol{J} \\ \boldsymbol{K} \end{bmatrix} \tag{5.4}$$

Let the relative position vector has coordinates $[r_X, r_Y, r_Z]$ in the GEI frame. Then we have

$$[r_X \quad r_Y \quad r_Z] = [\bar{r}_x \quad \bar{r}_y \quad \bar{r}_z]M^{L/G} \tag{5.5}$$

which results in

$$[\bar{r}_x \quad \bar{r}_y \quad \bar{r}_z] = [r_X \quad r_Y \quad r_Z][M^{L/G}]^{-1} = [r_X \quad r_Y \quad r_Z][M^{L/G}]^T \tag{5.6}$$

The above equation means that the variables in Eq. (5.1) and (5.3) can be replaced by components of the relative position vector in the GEI frame, which will generate the corresponding contraints in the GEI frame. For example, consider an elliptic orbit which has inclination $i = 0$ and its perigee is right on the Y-axis of the GEI frame. So, in Eqs. (2.26)-(2.29), Ω, i, and ω are chosen as 0, 0, and $\frac{\pi}{2}$ respectively, which are used, based on Eq. (2.31), to compute

$$\begin{aligned}[M^{L/G}]^T =& [D_x(\frac{3\pi}{2})]^T[D_y(2\pi)]^T[D_x(0)]^T[D_y(\pi-\nu)]^T \\ =& \begin{bmatrix} -\cos\nu & 0 & \sin\nu \\ -\sin\nu & 0 & -\cos\nu \\ 0 & -1 & 0 \end{bmatrix}\end{aligned} \tag{5.7}$$

Substituting it to Eq. (5.6), we have

$$\begin{aligned} \bar{r}_x &= -r_X\cos\nu - r_Y\sin\nu \\ \bar{r}_Y &= -r_Z \\ \bar{r}_Z &= r_X\sin\nu - r_Y\cos\nu \end{aligned} \tag{5.8}$$

With the above equations, Eq. (5.1) can be rewriten as

$$r_X^2 + r_Y^2 + r_Z^2 \geq d^2 \tag{5.9}$$

and Eq. (5.3) is rewritten as

$$(\frac{\cos^2\nu}{a^2} + \frac{\sin^2\nu}{c^2})r_X^2 + (\frac{1}{a^2} - \frac{1}{c^2})\sin(2\nu)r_Xr_Y + (\frac{\sin^2\nu}{a^2} + \frac{\cos^2\nu}{c^2})r_Y^2 + \frac{r_Z^2}{b^2} \geq 1 \tag{5.10}$$

Eq. (5.9) or (5.10) is the constraint that needed to be added to problem (3.55)–(3.62) for collision avoidance. Immediately one recognizes that the constraint is neither linear nor second-order cone, the two types of inequality constraints that can be handled in SOCP. Rather, they are concave inequality constraints.

Remark:

For practical numerical implementation, the form of expression for constraints in either Eq. (5.9) or (5.10) may cause numerical problems. For example, the solution obtained may not satisfy those constraints, even though they are indeed included in problem formulation. It is because of the limited accuracy of an algorithm that the constraints in Eq. (5.9) or (5.10) can not be satisfied in any digit accuracy. The prescribed variables d, a, b, c are all small after normalization, and their square becomes even smaller. Therefore, it is always better to express Eq. (5.9) and (5.10) in the following forms:

$$\sqrt{r_X^2 + r_Y^2 + r_Z^2} \geq d \tag{5.11}$$

$$\sqrt{(\cos^2\nu + \frac{a^2\sin^2\nu}{c^2})r_X^2 + (1 - \frac{a^2}{c^2})\sin(2\nu)r_X r_Y + (\sin^2\nu + \frac{a^2\cos^2\nu}{c^2})r_Y^2 + \frac{a^2 r_Z^2}{b^2}} \geq a \tag{5.12}$$

In the development hereafter, the notation for the quadratic-cone K induced partial ordering "$\geq_K$" follows the standard used in the conic optimization literature (e. g., see Ref. [33]). To make the analysis below also applicable to other problems with collision avoidance, we generate the expression for the collision avoidance constraints. The

following SOCP problem with concave inequality constraints is considered [56]:

$$\mathrm{P}^1: \quad \min_{\boldsymbol{y}} \quad \boldsymbol{c}^T\boldsymbol{y} \tag{5.13}$$

$$\text{subject to} \quad H\boldsymbol{y} \leq \boldsymbol{p} \tag{5.14}$$

$$g_i(\boldsymbol{y}) \leq 0, \; i = 1, \ldots, l \tag{5.15}$$

$$A\boldsymbol{y} - \boldsymbol{b} \geq_K 0 \tag{5.16}$$

where $\boldsymbol{y} \in R^N$ is the variable vector consisting of the collection of all state and control variables at the discretization points, and $\boldsymbol{c}$ is a constant column vector; $H \in R^{M\times N}$ is a constant matrix and $\boldsymbol{p} \in R^M$ is a constant vector. Each of the linear equality constraints in Eqs. (3.61) and (3.62) is expressed by two linear inequality constraints and included in Eq. (5.14). Eqs. (3.58) and (3.60) can be directly transformed into the form of Eq. 5.14. Each $g_i(\boldsymbol{y})$ is a concave function, which could be from (5.1) or (5.3). All the second-order cone constraints in Eqs. (3.57) and (3.59) are represented in Eq. (5.16). See Chapter 2 on how to represent it. The cone K is a direct product of second-order cones of dimension n_i, defined as

$$K = K^{n_1} \times K^{n_2} \times \cdots \times K^{n_r} \tag{5.17}$$

where each K^{n_i} represents the quadratic cone at a discretization point from a second-order-cone constraint in the original problem.

5.3 Successive Linear Approximation

5.3.1 Methodology

It is obvious in P^1 that the constraints (5.15) neither convex nor second-order cones, while violates the requirement in SOCP. One may find a way to equate the effects of Eq. (5.15) with linear affine constraints. When the concave constraints in Eq. (5.15) are linearized about the k-iterated solution $\boldsymbol{y}^{[k]}$, a related subproblem $\mathrm{PP}(\boldsymbol{y}^{[k]})$ is formulated

for a given $\boldsymbol{y}^{[k]} \in R^N$ as follows:

$$\text{PP}(\boldsymbol{y}^{[k]}): \quad \min_{\boldsymbol{y}} \quad \boldsymbol{c}^T\boldsymbol{y} \tag{5.18}$$

$$\text{subject to} \quad H\boldsymbol{y} \leq \boldsymbol{p} \tag{5.19}$$

$$g_i(\boldsymbol{y}^{[k]}) + \nabla g_i^T(\boldsymbol{y}^{[k]})(\boldsymbol{y} - \boldsymbol{y}^{[k]}) \leq 0, \; i = 1, \ldots, l \tag{5.20}$$

$$A\boldsymbol{y} - \boldsymbol{b} \geq_K 0 \tag{5.21}$$

$$\|\boldsymbol{y} - \boldsymbol{y}^{[k]}\| \leq \rho \tag{5.22}$$

where $\nabla g_i(\boldsymbol{y}^{[k]})$ is the gradient of $g_i(\boldsymbol{y})$ at $\boldsymbol{y}^{[k]}$. The constraint (5.22) is a "trust-region" constraint (which is a second-order cone) for the linearization in Eq. (5.20) and ρ is the radius of the trust region. This constraint will prevent $\|\boldsymbol{y} - \boldsymbol{y}^{[k]}\|$ from getting too large before convergence so that the linearized constraints in Eq. (5.20) are reasonable approximations to the original constraints (5.15). This mechanism is found to be important for this approach to be robust.

The Problem PP($\boldsymbol{y}^{[k]}$) is an SOCP problem for a given $\boldsymbol{y}^{[k]}$. In this dissertation a sequence of the problems PP($\boldsymbol{y}^{[k]}$), $k = 1, 2, \ldots$, will be solved in order to find the solution to Problem P^1.

5.3.2 Convergence

It will be shown that if Problem P^1 has a solution that satisfies the necessary conditions for optimality, known as the Karush-Kuhn-Tucker (KKT) conditions [22], the solutions of the problems PP($\boldsymbol{y}^{[k]}$) will converge to the KKT-solution of Problem P^1 under certain conditions to be stated later. The discussion thereafter on convergence is from Ref. [56]. We start with the following result first:

Lemma 5.3.1. *If $g_i(\boldsymbol{y})$ in (5.15) is C^2, and concave, then any $\boldsymbol{y}$ that is feasible for Problem PP($\boldsymbol{y}^{[k]}$) is also feasible for Problem P^1.*

Proof. Since all the constraints in Problem P^1 are also in Problem $\mathrm{PP}(\boldsymbol{y}^{[k]})$, except for the difference between (5.15) and (5.20), it is only necessary to show that any $\boldsymbol{y}$ feasible for (5.20) will be feasible for (5.15). Let $\boldsymbol{y}$ be an arbitrary feasible point to constraint (5.20), i.e.,

$$g_i(\boldsymbol{y}^{[k]}) + \nabla g_i^T(\boldsymbol{y}^{[k]})(\boldsymbol{y} - \boldsymbol{y}^{[k]}) \leq 0 \tag{5.23}$$

Represent $g_i(\boldsymbol{y})$ by the second-order Taylor series expansion

$$g_i(\boldsymbol{y}) = g_i(\boldsymbol{y}^{[k]}) + \nabla g_i^T(\boldsymbol{y}^{[k]})(\boldsymbol{y} - \boldsymbol{y}^{[k]}) + \frac{1}{2}(\boldsymbol{y} - \boldsymbol{y}^{[k]})^T \nabla^2 g_i \left[\boldsymbol{y}^{[k]} + \theta(\boldsymbol{y} - \boldsymbol{y}^{[k]})\right](\boldsymbol{y} - \boldsymbol{y}^{[k]}) \tag{5.24}$$

where $\theta \in [0, 1]$ and $\nabla^2 g_i$ the Hessian of g_i. Using Eq. (5.23) in the above equation leads to

$$g_i(\boldsymbol{y}) \leq \frac{1}{2}(\boldsymbol{y} - \boldsymbol{y}^{[k]})^T \nabla^2 g_i \left[\boldsymbol{y}^{[k]} + \theta(\boldsymbol{y} - \boldsymbol{y}^{[k]})\right](\boldsymbol{y} - \boldsymbol{y}^{[k]}) \tag{5.25}$$

Since $g_i(\boldsymbol{y})$ is concave, $\nabla^2 g_i \left[\boldsymbol{y}^{[k]} + \theta(\boldsymbol{y} - \boldsymbol{y}^{[k]})\right]$ is negative definite or negative semi-definite, therefore $g_i(\boldsymbol{y}) \leq 0$ from the above equation, which is exactly condition (5.15). □

Since the constraint in Eq. (5.22) is also a second-order cone, it can be put into the following form

$$A_{n_{r+1}}\boldsymbol{y} - \boldsymbol{b}_{n_{r+1}} \geq_{K^{n_r+1}} 0 \tag{5.26}$$

where $A_{n_{r+1}}$ and $\boldsymbol{b}_{n_{r+1}}$ are constructed as

$$[A_{n_{r+1}}; \boldsymbol{b}_{n_{r+1}}] = \begin{bmatrix} I_{n\times n} & \boldsymbol{y}^{[k]} \\ \mathbf{0}_{1\times n} & -\rho \end{bmatrix} \tag{5.27}$$

Hence, Eq. (5.22) can be combined with Eq. (5.21) to give

$$A\boldsymbol{y} - \boldsymbol{b} \geq_{\bar{K}} 0 \tag{5.28}$$

where $\bar{K} = K \times K^{n_r+1}$ is the direct product of K and K^{n_r+1}.

The relationship between the solutions to Problem P^1 and $\mathrm{PP}(\boldsymbol{y}^{[k]})$ is established by the following lemma.

Lemma 5.3.2. *Suppose that the quadratic-cone constraints in Problem PP($\boldsymbol{y}^{[k]}$) are strictly feasible, i.e., there exists a $\boldsymbol{y} \in R^N$ such that*

$$A\boldsymbol{y} - \boldsymbol{b} >_{\bar{K}} 0, \qquad H\boldsymbol{y} \leq \boldsymbol{p}, \qquad g_i(\boldsymbol{y}^{[k]}) + \nabla g_i^T(\boldsymbol{y}^{[k]})(\boldsymbol{y} - \boldsymbol{y}^{[k]}) \leq 0,\ i = 1, \ldots, l \quad (5.29)$$

If the optimal solution $\boldsymbol{y}^*$ to Problem PP($\boldsymbol{y}^{[k]}$) is $\boldsymbol{y}^{[k]}$ itself, then $\boldsymbol{y}^* = \boldsymbol{y}^{[k]}$ is a Karush-Kuhn-Tucker solution for Problem P^1.

Proof. See the Appendix. □

Note that no claim is made in Lemma 5.3.2 about the optimality of the KKT solution of Problem P^1. But later it will shown that the objective function of Problem P^1 is indeed improved by each successive solution.

Suppose that the solution to PP($\boldsymbol{y}^{[k]}$) is found and designated by $\boldsymbol{y}^{[k+1]}$. Form the problem PP($\boldsymbol{y}^{[k+1]}$) and assume that its solution is found again. Repeating this process will generate a sequence of solutions $\{\boldsymbol{y}^{[k]}\}$. Lemma 5.3.2 states that if this solution sequence converges, a KKT solution to the original problem P^1 is found. The next lemma answers whether a solution sequence $\{\boldsymbol{y}^{[k]}\}$ can indeed be generated.

Lemma 5.3.3. *If $\boldsymbol{y}^*$ is the solution to Problem PP($\boldsymbol{y}^{[k-1]}$) for a given $\boldsymbol{y}^{[k-1]}$, and denote $\boldsymbol{y}^{[k]} = \boldsymbol{y}^*$. Then Problem PP($\boldsymbol{y}^{[k]}$) has an optimal solution.*

Proof. For Problem PP($\boldsymbol{y}^{[k]}$), $\boldsymbol{y} = \boldsymbol{y}^{[k]}$ immediately satisfies constraints (5.19), (5.21) and (5.22) by the fact that $\boldsymbol{y}^{[k]}$ is the solution to Problem PP($\boldsymbol{y}^{[k-1]}$). As for Eq. (5.20), using Lemma 1 (Eq. (5.24) in particular) gives rise to $g_i(\boldsymbol{y}^{[k]}) \leq 0$. Thus $\boldsymbol{y} = \boldsymbol{y}^{[k]}$ is also feasible to Eq. (5.20), hence $\boldsymbol{y}$ is a feasible solution to Problem PP($\boldsymbol{y}^{[k]}$). Define the feasibility set C of Problem PP($\boldsymbol{y}^{[k]}$)

$$C = \left\{\boldsymbol{y} \in R^n \mid H\boldsymbol{y} \leq \boldsymbol{p},\ g_i(\boldsymbol{y}^{[k]}) + \nabla g_i(\boldsymbol{y}^{[k]})^T(\boldsymbol{y} - \boldsymbol{y}^{[k]}) \leq 0,\ A\boldsymbol{y} - \boldsymbol{b} \geq_K 0,\ \|\boldsymbol{y} - \boldsymbol{y}^{[k]}\| \leq \rho\right\} \quad (5.30)$$

The fact that $\boldsymbol{y} = \boldsymbol{y}^{[k]} \in C$ means that the feasible set C of Problem PP($\boldsymbol{y}^{[k]}$) is not empty. It is obvious that the set C, an intersection of half-spaces and second-order cones,

is closed. In addition, the trust-region constraint (5.22) renders C bounded. Therefore, the set C is compact. The objective function in PP($\boldsymbol{y}^{[k]}$) is continuous on C. Then, by the Weierstrass Theorem [57], there exists a minimizer in C for Problem PP($\boldsymbol{y}^{[k]}$). □

From the proof it is evident that $\boldsymbol{y}^{[k]}$ need only be a feasible solution, not necessarily optimal. Note that Lemma 5.3.3 is sufficient, but not necessary for the solution to Problem PP($\boldsymbol{y}^{[k]}$) to exist. Suppose that for an arbitrary $\boldsymbol{y}^{[0]}$, the solution to Problem PP($\boldsymbol{y}^{[0]}$) is found. Set that solution to be $\boldsymbol{y}^{[1]}$. Then the optimal solution to Problem PP($\boldsymbol{y}^{[1]}$) exists by Lemma 5.3.3. Designate this optimal solution to be $\boldsymbol{y}^{[2]}$ and repeat this process. Lemma 5.3.3 establishes that such a solution sequence $\{\boldsymbol{y}^{[k]}\}$, $k = 1, 2, \ldots$, exists under a very mild condition. The next lemma addresses the change in the objective function caused by the sequence $\{\boldsymbol{y}^{[k]}\}$.

Lemma 5.3.4. *If $\boldsymbol{y} = \boldsymbol{y}^{[k]}$ is feasible to PP($\boldsymbol{y}^{[k]}$), and $\boldsymbol{y}^*$ solves the problem PP($\boldsymbol{y}^{[k]}$), then the objective function is non-increasing from $\boldsymbol{y}^{[k]}$ to $\boldsymbol{y}^*$, i. e.,*

$$\boldsymbol{c}^T\boldsymbol{y}^* \leq \boldsymbol{c}^T\boldsymbol{y}^{[k]} \tag{5.31}$$

Furthermore, if $\boldsymbol{y}^*$ is the unique optimal solution to Problem PP($\boldsymbol{y}^{[k]}$), and $\boldsymbol{y}^* \neq \boldsymbol{y}^{[k]}$, the above condition holds strictly

$$\boldsymbol{c}^T\boldsymbol{y}^* < \boldsymbol{c}^T\boldsymbol{y}^{[k]} \tag{5.32}$$

Proof. If $\boldsymbol{y}^*$ is the (optimal) solution and $\boldsymbol{y} = \boldsymbol{y}^{[k]}$ is a feasible solution, both to Problem PP($\boldsymbol{y}^{[k]}$), then the objective function corresponding to $\boldsymbol{y}^*$ is no greater than that corresponding to $\boldsymbol{y}^{[k]}$

$$\boldsymbol{c}^T\boldsymbol{y}^* \leq \boldsymbol{c}^T\boldsymbol{y}^{[k]} \tag{5.33}$$

When $\boldsymbol{y}^*$ is the unique solution of Problem PP($\boldsymbol{y}^{[k]}$), assume that $\boldsymbol{c}^T\boldsymbol{y}^* = \boldsymbol{c}^T\boldsymbol{y}^{[k]}$. Since $\boldsymbol{y}^{[k]}$ is feasible to Problem PP($\boldsymbol{y}^{[k]}$), This means that $\boldsymbol{y}^{[k]} \neq \boldsymbol{y}^*$ is also optimal, which contradicts the uniqueness of $\boldsymbol{y}^*$. Therefore, only the strict inequality in Eq. (5.33) can hold, and this is the conclusion in Eq. (5.32). □

Note that the assumption of uniqueness of optimal solution to Problem PP($\boldsymbol{y}^{[k]}$) is not a very stretched condition. Lemma 5.3.3 already ensures the existence of an optimal solution. Problem PP($\boldsymbol{y}^{[k]}$) is a convex optimization problem and any of its minimum is global. All it takes for condition (5.32) to hold is that this global minimum is unique. By Lemma 5.3.4, if Problem PP($\boldsymbol{y}^{[k]}$) always has a unique optimal solution for all k, the solution sequence $\{\boldsymbol{y}^{[k]}\}$, obtained by recursively solving Problem PP($\boldsymbol{y}^{[k]}$) satisfies the following monotone decreasing condition

$$\boldsymbol{c}^T\boldsymbol{y}^{[k+1]} < \boldsymbol{c}^T\boldsymbol{y}^{[k]} \tag{5.34}$$

In fact, starting from an arbitrary $\boldsymbol{y}^{[0]} \in R^n$, as long as a feasible solution $\boldsymbol{y}^{[1]}$ to Problem PP($\boldsymbol{y}^{[0]}$) can be found, by Lemma 5.3.3 such a sequence $\{\boldsymbol{y}^{[k]}\}$ is guaranteed to exist, and can be found by solving Problem PP successively. Under the condition of Lemma 5.3.4, this sequence will enjoy the monotone decreasing property in Eq. (5.34). This condition, together with Lemma 5.3.1, means that the objective function in Problem P^1 is improving successively by the sequence $\{\boldsymbol{y}^{[k]}\}$.

Lemmas 5.3.1–5.3.4 have laid the groundwork for the following convergence result.

Theorem 5.3.1. *Let $\{\boldsymbol{y}^{[k]}\}$ be a sequence of the solutions obtained by recursively solving Problem PP. Assume that there exists a unique solution for each of Problems PP($\boldsymbol{y}^{[k]}$), and the quadratic-cone constraints in each of the Problems PP($\boldsymbol{y}^{[k]}$) are strictly feasible (cf. Eq. (5.29)). Then either the sequence $\{\boldsymbol{y}^{[k]}\}$ terminates in finite steps with a KKT solution to Problem P^1, or an infinite sequence $\{\boldsymbol{y}^{[k]}\}$ converges to a KKT solution of Problem P^1.*

Proof. The sequence $\{\boldsymbol{y}^{[k]}\}$ terminates in finite steps if at one step $\boldsymbol{y}^{[k+1]} = \boldsymbol{y}^{[k]}$. Then by Lemma 5.3.2, $\boldsymbol{y}^{[k]}$ is a KKT solution of Problem P^1. Next, consider the case when $\{\boldsymbol{y}^{[k]}\}$ is an infinite sequence. Eq. (5.22) implies that $\{\boldsymbol{y}^{[k]}\}$ is bounded. Thus $\{\boldsymbol{y}^{[k]}\}$ is in a compact set in R^n. Then there is a subsequence $\{\boldsymbol{y}^{[k_i]}\}$ that converges to a limit

$\boldsymbol{y}^*$. Choose the merit function (referred to as the "adaptation function" in Ref. [58]) to be $Z(\boldsymbol{y}) = \boldsymbol{c}^T\boldsymbol{y}$. By Lemma 5.3.4, $Z(\boldsymbol{y}^{[k+1]}) < Z(\boldsymbol{y}^{[k]})$. Since Z is continuous, so $Z(\boldsymbol{y}^{[k_i]}) \longrightarrow Z(\boldsymbol{y}^*)$. By Lemma 4.1 in Zangwill [58], we also have $Z(\boldsymbol{y}^{[k]}) \longrightarrow Z(\boldsymbol{y}^*)$ for the entire sequence $\{\boldsymbol{y}^{[k]}\}$. Represent the process of solving Problem PP($\boldsymbol{y}^{[k]}$) to get $\boldsymbol{y}^{[k+1]}$ by the point-to-set mapping $\boldsymbol{y}^{[k+1]} \in \mathcal{M}(\boldsymbol{y}^{[k]})$ where the set $\mathcal{M}(\boldsymbol{y}^{[k]})$ consists of all the solutions to Problem PP($\boldsymbol{y}^{[k]}$) [58]. By the condition of uniqueness of solution to Problem PP($\boldsymbol{y}^{[k]}$), we can simply use the expression $\boldsymbol{y}^{[k+1]} = \mathcal{M}(\boldsymbol{y}^{[k]})$. Since the KKT conditions used to find the solution of Problem PP($\boldsymbol{y}^{[k]}$) are continuous in $\boldsymbol{y}^{[k]}$, and the solution of these conditions depends continuously on $\boldsymbol{y}^{[k]}$, the mapping $\mathcal{M}$ is closed in the sense as defined in Ref. [58]. Therefore we must have the conclusion that $\boldsymbol{y}^* = \mathcal{M}(\boldsymbol{y}^*)$. To prove this conclusion by contradiction, suppose that it is not true. Consider the sequence $\{\boldsymbol{y}^{[k_i+1]}\}$ which is obtained by increasing the index of each element in the sequence $\{\boldsymbol{y}^{[k_i]}\}$ by 1. Then $\{\boldsymbol{y}^{[k_i+1]}\}$ contains a subsequence $\{\boldsymbol{y}^{[k_i+1]_j}\}$ that converges to a limit $\boldsymbol{y}^{*+1}$. Let $\boldsymbol{y}^{[k_i]_j}$ be the jth element of the sequence $\{\boldsymbol{y}^{[k_i]}\}$, and $\boldsymbol{y}^{[k_i+1]_j}$ the jth element of the sequence $\{\boldsymbol{y}^{[k_i+1]}\}$. Since $\boldsymbol{y}^{[k_i+1]_j} = \mathcal{M}(\boldsymbol{y}^{[k_i]_j})$, $\boldsymbol{y}^{[k_i+1]_j} \longrightarrow \boldsymbol{y}^{*+1}$, and $\boldsymbol{y}^{[k_i]_j} \longrightarrow \boldsymbol{y}^*$, we have $\boldsymbol{y}^{*+1} = \mathcal{M}(\boldsymbol{y}^*)$ by the closeness of the mapping $\mathcal{M}$. But $\boldsymbol{y}^{*+1} \neq \boldsymbol{y}^*$ since $\boldsymbol{y}^* \neq \mathcal{M}(\boldsymbol{y}^*)$ is assumed. Consequently by Lemma 5.3.4

$$Z(\boldsymbol{y}^{*+1}) < Z(\boldsymbol{y}^*) \tag{5.35}$$

Since $\{\boldsymbol{y}^{[k_i+1]_j}\}$ is a subsequence of $\{\boldsymbol{y}^{[k]}\}$, and $Z(\boldsymbol{y}^{[k]}) \longrightarrow Z(\boldsymbol{y}^*)$, thus it is necessary that $Z(\boldsymbol{y}^{*+1}) = Z(\boldsymbol{y}^*)$. But this result contradicts with the finding in Eq. (5.35). So we must have $\boldsymbol{y}^* = \mathcal{M}(\boldsymbol{y}^*)$. Again by Lemma 5.3.2, $\boldsymbol{y}^*$ is a KKT solution of Problem P^1. □

Nothing has been said so far about the optimality of the KKT solution of the original Problem P^1 where the successive solution sequence $\{\boldsymbol{y}^{[k]}\}$ converges to, i. e., whether this KKT solution is indeed a minimum. In the following, we guarantee that this KKT solution is *at least* a local minimum of Problem P^1.

Corollary

Let the conditions assumed in the Theorem hold. Let $\boldsymbol{y}^*$ be the *accumulation point* of the successive solution sequence $\{\boldsymbol{y}^{[k]}\}$ identified in the proof of the Theorem, or the last solution when $\{\boldsymbol{y}^{[k]}\}$ terminates in finite steps. Then $\boldsymbol{y}^*$ is at least a local minimum of Problem P^1.

Proof: The conclusion will be proven by contradiction. First realize from the proof of the Theorem that $\boldsymbol{y}^*$ is the solution to Problem $\mathrm{PP}(\boldsymbol{y}^*)$. Assume that $\boldsymbol{y}^*$ is not a local minimum of Problem P^1. This implies that for any arbitrarily small $\delta > 0$, there exists a $\tilde{\boldsymbol{y}}$ such that $\tilde{\boldsymbol{y}}$ is feasible to Problem P^1, $\|\boldsymbol{y}^* - \tilde{\boldsymbol{y}}\| \leq \delta$, and the following condition holds

$$\boldsymbol{c}^T \tilde{\boldsymbol{y}} < \boldsymbol{c}^T \boldsymbol{y}^* \tag{5.36}$$

By Taylor's Theorem, we have

$$g_i(\tilde{\boldsymbol{y}}) = g_i(\boldsymbol{y}^*) + \nabla g_i^T(\boldsymbol{y}^*)(\tilde{\boldsymbol{y}} - \boldsymbol{y}^*) + \frac{1}{2}(\tilde{\boldsymbol{y}} - \boldsymbol{y}^*)^T \nabla^2 g_i \left[\boldsymbol{y}^* + \theta(\tilde{\boldsymbol{y}} - \boldsymbol{y}^*)\right](\tilde{\boldsymbol{y}} - \boldsymbol{y}^*), \quad \theta \in [0,1] \tag{5.37}$$

For sufficiently small δ, the first two terms in the above equation dominate the second-order term on the right-hand side. Since $g_i(\tilde{\boldsymbol{y}}) \leq 0$ as $\tilde{\boldsymbol{y}}$ is feasible to Problem P^1, this implies that

$$\nabla g_i(\boldsymbol{y}^*) + g_i^T(\boldsymbol{y}^*)(\tilde{\boldsymbol{y}} - \boldsymbol{y}^*) \leq 0 \tag{5.38}$$

This is because if condition (5.38) is not true, it would lead to $g_i(\tilde{\boldsymbol{y}}) > 0$ for a $\tilde{\boldsymbol{y}}$ sufficiently close to $\boldsymbol{y}^*$, and this is a contradiction. Condition (5.38) and the fact that $\tilde{\boldsymbol{y}}$ is feasible to other constraints in Problem $\mathrm{PP}(\boldsymbol{y}^*)$ because of the feasibility of $\tilde{\boldsymbol{y}}$ to the same constraints in Problem P^1 suggest that $\tilde{\boldsymbol{y}}$ is feasible to Problem $\mathrm{PP}(\boldsymbol{y}^*)$. Equation (5.36) implies that there is another feasible solution to Problem $\mathrm{PP}(\boldsymbol{y}^*)$ that produces a smaller objective function value than $\boldsymbol{y}^*$ does, which contradicts the condition that $\boldsymbol{y}^*$ is the optimal solution of $\mathrm{PP}(\boldsymbol{y}^*)$. Therefore $\boldsymbol{y}^*$ must be at least a local minimum of Problem P^1. ♣

Remarks:

1. The above convergence results provide a rigorous foundation for the successive solution method in this dissertation that other heuristic approaches lack. Another implication of the above convergence theorem is that, unlike the existing approaches in the literature, there will be no conservativeness in constraint satisfaction when convergence occurs, even though linearization is used in Eq. (5.20) to approximate the nonlinear constraints (5.15). This is true because at convergence, the constraints in (5.20) in Problem PP($\boldsymbol{y}^{[k]}$) are the same as the original constraints (5.15) in Problem P[1], as the solution is $\boldsymbol{y}^* = \boldsymbol{y}^{[k]}$.

2. In the standard convergence analysis of the well-recognized general nonlinear programming algorithm, the sequential quadratic programming (SQP) method, the convergence conclusion is reached on the basis of certain algorithmic parameter selection rules dependent on the Lagrange multipliers of the problem [18, 19]. Since the Lagrange multipliers are not known *a priori*, the convergence proof has only theoretical significance, but offers little in algorithm implementation for guaranteed convergence. Here the general nonlinear constraints in a general nonlinear programming problem the SQP method allows are traded for a special class of constraints (concave constraints) and an SOCP setting. The payoff is the certainty of ensured convergence (under proper conditions) of the algorithm without depending on unknown parameters.

3. Even though the above convergence conclusions are derived in the context of using an SOCP-based approach, little needs to be changed for the conclusions to be applicable if a Linear Programming (LP) based method is used to solve a problem with concave inequality constraints. Hence, conceivably the problems solved by using LP-based methods in Refs. [15–17] can benefit from the development in this dissertation with the a similar successive LP solution approach.

5.4 Numerical Demonstration

For the PRO problem with keep-out zone constraints (or collision avoidance constraints), two examples are given to demonstrate the effectiveness of the methodology proposed in the previous sections.

Elliptic Keep-out Zone and V-bar Approach

In this RPO problem, the target spacecraft is in an *elliptical* orbit with eccentricity $e = 0.3$ and perigee altitude of 350 km. A chaser spacecraft has an initial mass of 1500 kg. The chaser's engine has a maximum thrust of 30 N (a maximum thrust acceleration of just 2.0×10^{-3} g) and specific impulse of 200 sec. In order to express the relative position and velocity between the target and chaser conveniently, the standard local-vertical local-horizontal (LVLH) frame centered at the target is used. At $t_0 = 0$, the target has a true anomaly of 10 deg, the chaser is located 6 km behind and 300 m below the target, i. e., the relative position vector in the LVLH frame is $\boldsymbol{r}_{rel}$=[-6000, 0, 300] m, and relative velocity vector is $\boldsymbol{V}_{rel}$=[-0.5, 0, 0.2] m/s. The chaser is required to fly around the target to a close distance on the V-bar axis in front of the target, approach it and finally dock with it along the V-bar axis within a total given time t_f=4000 sec. The performance index is minimum-propellant consumption. During the process, there are a variety of constraints imposed as follows:

1. At t_1=2000 sec, the chaser is required to be 200 m ahead of the target on the V-bar direction with relative velocity no greater than 0.2 m/s. This is called the Acquisition-of-the-Docking-Axis constraint.

2. For $t \in [t_0, t_1]$, there is a *Keep-Out Zone* (KOZ) constraint [59] which is defined here to be an ellipsoid in the LVLH frame, centered at the target with the semi-major axis of 200 m along the V-bar axis and two semi-minor axes of 100 m. The

chaser cannot enter this KOZ before t_1 to avoid the risk of collision between the two spacecraft. This is a concave (and non-spherical) state inequality constraint.

3. For all $t \in [t_1, t_f]$, the chaser should remain inside an approach corridor which is defined by a circular cone fixed at the target which has V-bar axis as its centerline, a half angle of 10 deg and the apex at the target vehicle.

4. Once inside the approach corridor and for $t \in (t_1, t_2]$ with t_2=3200 sec, the relative velocity is constrained to be less than 0.3 m/s and the chaser thrust plume (negative of the thrust direction) should point at least 60 deg away from the target; and the parameters for those constraints become 0.1 m/s and 89 deg respectively for $t \in (t_2, t_f]$.

5. At t_f, the relative position and velocity between the chaser and the target are both zero. For a target vehicle on a known orbit, these conditions form 6 linear terminal conditions.

The reader is referred to Ref. [9] for more detailed formulation and description of the RPO problem (note that the KOZ constraint is not imposed in Ref. [9]). In addition, the rate of change of thrust vector within the approach corridor is also constrained as in Ref. [52]. Only inverse-square gravity field is used in this example. For more realistic modeling such as a gravity field with high-order gravitational harmonics and aerodynamic drag, see Ref. [52].

Even without the KOZ constraint, repeated attempts to solve this RPO problem by general-purpose trajectory optimization software have failed. Now with the KOZ, the numerical results by the proposed method are shown in Figs. 5.3–5.5. One of the trajectories in Fig. 5.3 shows that the optimal chaser trajectory would violate the KOZ constraint without including it (the closest approach is 85 m, shorter than the semi-minor axis of the keep-out ellipsoid). When the KOZ constraint is included, the approach proposed in

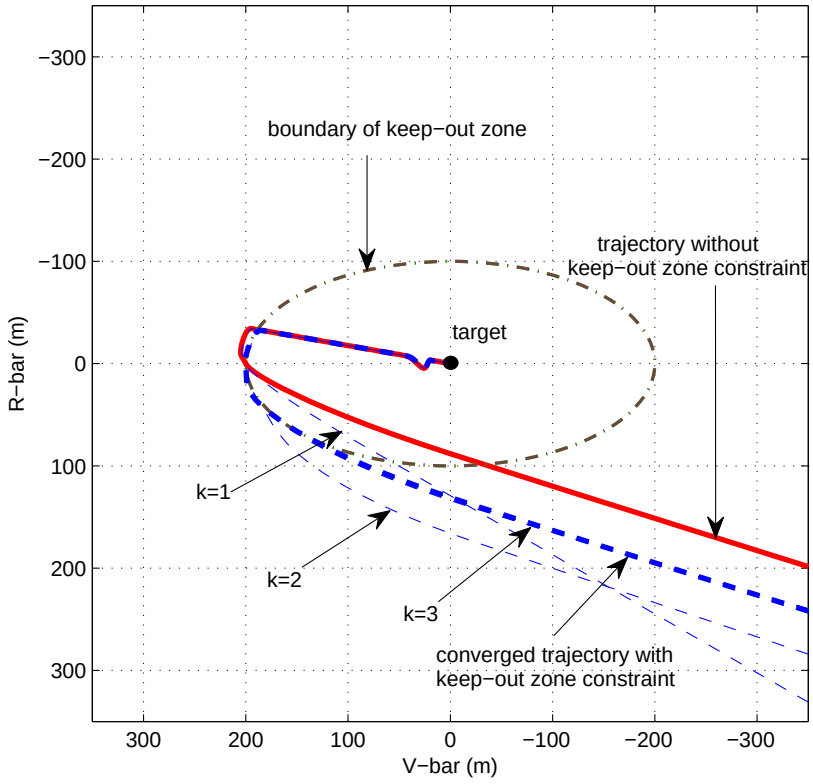

Figure 5.3 RPO trajectories in LVLH frame with Keep-Out Zone constraint, V-bar approach.

Section 5.3 very effectively and conveniently enforces it. As seen from Fig. 5.3, a part of the converged trajectory lies on the boundary of the KOZ. While the convergence is ensured by the Theorem in Section 5.3.2, in this example the convergence is also achieved rapidly in just 4 iterations: in the first iterate ($k = 1$) the trajectory is one generated without including the constraint, and it violates the KOZ constraint. The second iterate ($k = 2$) is obtained from solving Problem PP($\boldsymbol{y}^{[1]}$) in Section 5.3. By Lemma 5.3.1 this solution will be feasible to original Problem P^1, which indeed is the case as is evident from Fig. 5.3. All further iterates will be feasible to the original problem from this point on. When $k = 3$ the solution is already indiscernible from the converged solution (when $k = 4$) in the scale of Fig. 5.3.

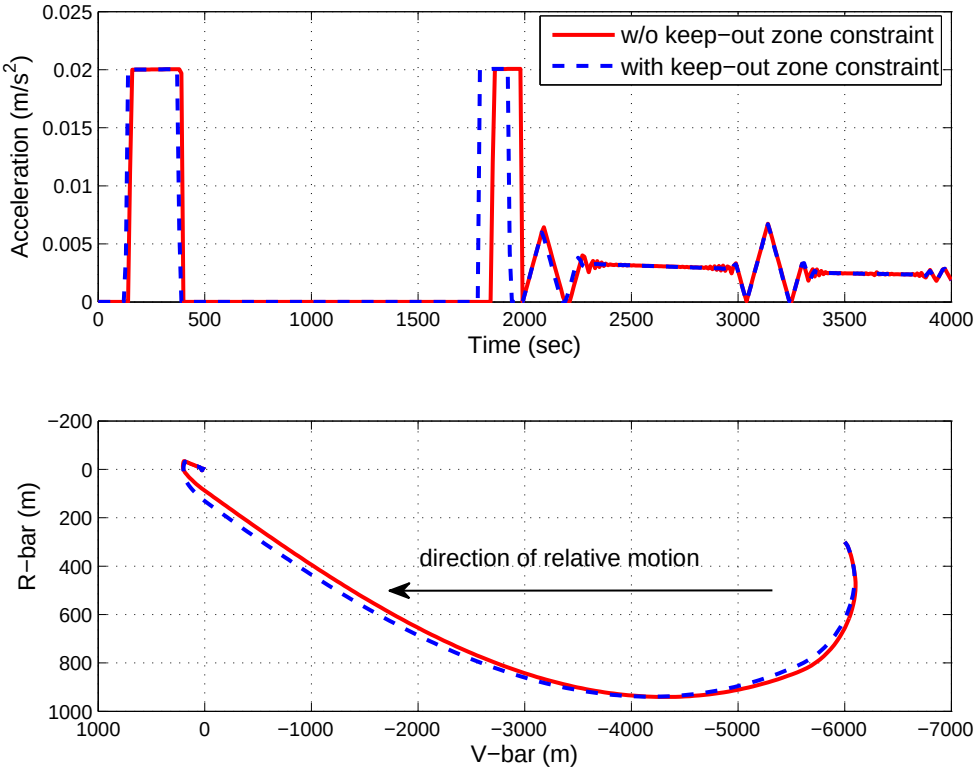

Figure 5.4 The magnitude of thrust acceleration and the complete relative RPO trajectory in the LVLH frame, V-bar approach.

The top subplot of Fig. 5.4 reveals that for $t \in [t_0, t_1]$ there are two burns no matter whether the KOZ constraint is enforced or not. However, with the constraint, the first burn occurs earlier in order to change the trajectory as seen in the lower subplot of Fig. 5.4 so as to help the second burn to steer the chaser to move on the boundary of the KOZ when the two vehicles are in close range. Another function of the second burn is to reduce the chaser's velocity relative to the target so that the velocity constraint at t_1 will be met. The variable thrust burn after $t_1 = 2000$ sec in the lower subplot of Fig. 5.4 is caused by the fact that the trajectory after t_1 is always on the boundary of either the approach corridor cone or the relative velocity magnitude constraint.

The zoom-in view of the RPO trajectory near the target along with the thrust direction during the second full-thrust burn and variable thrust-burn inside the approach

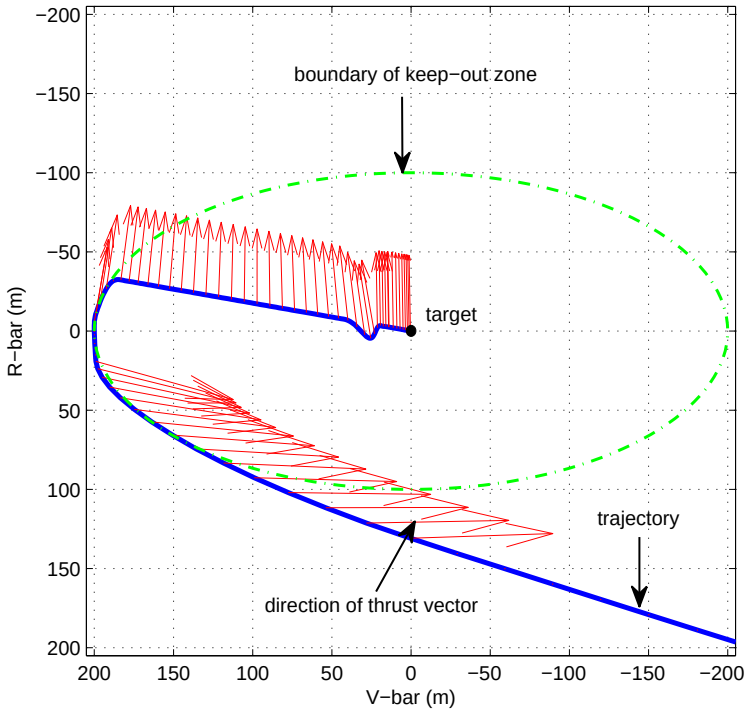

Figure 5.5 The RPO trajectory along with direction of the thrust vector near the target, V-bar approach.

corridor is plotted in Fig. 5.5. It can be seen that the second full-thrust burn is largely a braking maneuver, while the variable-thrust burn is mainly to maintain a relative trajectory along the V-bar direction, with the thrust vector nearly perpendicular to the relative trajectory. A considerable part of the chaser's trajectory is on the boundary of the KOZ constraint (about 210 sec), clearly indicating zero conservativeness in constraint satisfaction by the proposed approach. The propellant consumption increase due to the inclusion of the KOZ constraint is 0.58%.

Circular Keep-out Zone and R-bar Approach

The previous example shows the effectiveness of the methodology to solve the RPO problem with elliptic keep-out zone constraint and V-bar approach for proximity operations. Here the same chaser spacecraft is considered, but the target is in an elliptic orbit

with higher eccentricity $e = 0.5$ and $r_p = 350$ km. The R-bar approach, i.e., the chaser docks with the target in the R-bar direction, is used and the keep-out zone is circular. In addition, t_0, t_1, t_2 and t_f have the same values as before. At t_0, the relative position and velocity between the chaser and the target are [3500, 0, -3500] m and [-1, 0, 0.1] m/s, respectively. Following is a full description for all the constraints:

1. At t_1, the chaser has to arrive at a position in the R-bar axis that is 200 m from the target (ADA) and the relative velocity is no greater than 0.2 m/s.

2. For $t \in [t_0, t_1]$, the keep-out zone is a circle with radius of 180 m centered at the target.

3. When $t \in [t_1, t_f]$, the chaser is required to stay inside the approach corridor with half angle of 10 deg.

4. Within the approach corridor, for $t \in (t_1, t_2]$ the relative velocity is constrained to be less than 0.3 m/s and the chaser thrust plume (negative of the thrust direction) should point at least 60 deg away from the target; and the parameters for those constraints become 0.1 m/s and 89 deg respectively for $t \in (t_2, t_f]$.

The simulation results are shown in Fig. 5.6–5.8. As before, no matter there is KOZ constraint or not, the top plot of Fig. 5.6 shows there are two burns before the chaser enters the approach corridor. It is hard to notice the difference for the first burn when there is KOZ constraint or not, but the existence of difference is implied by the trajectory plotted in the bottom plot of Fig. 5.6. Actually, with consideration to the constraint the first burn lasts longer for about 10 sec. When the chaser is close to the target, the second burn occurs to steer the chaser to move along the boundary of the KOZ which is seen in Fig. 5.7. The functions of the second burn are similar to those discussed in the first example.

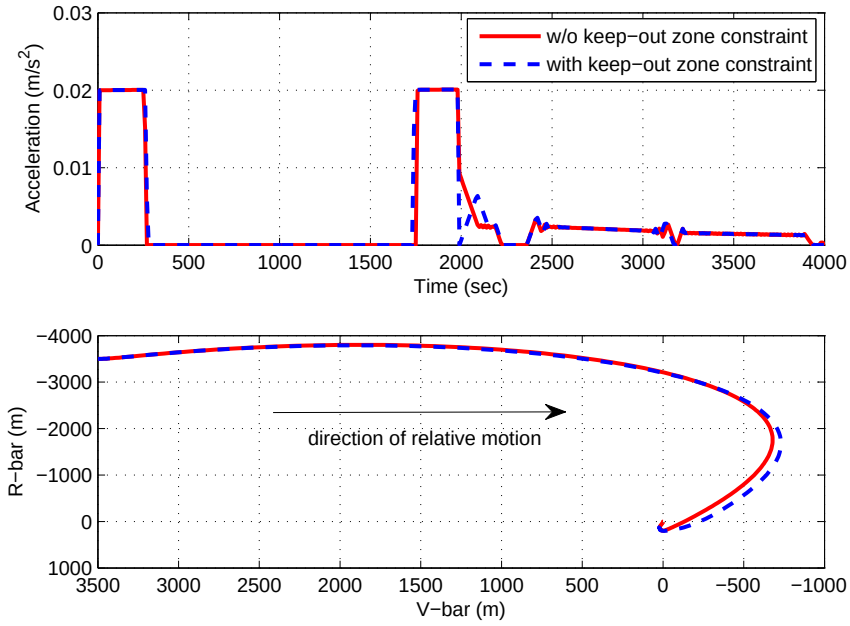

Figure 5.6 The magnitude of thrust acceleration and the relative trajectory in the LVLH frame for the R-bar approach.

It is illustrated in Fig. 5.7 that the trajectory in solid line violated the KOZ constraint and the shortest distance is about 115 m which is much smaller than the threshold 180 m, as shown in Fig. 5.8. When considering the KOZ constraint, the proposed methodology also successfully solves the problem, yielding a trajectory satisfying the KOZ constraint with no conservatism which is supported by the chaser's motion on the boundary of the KOZ for about 20 sec. This is reflected in Fig. 5.7 and Fig. 5.8.

Finally, it should be pointed out that the KOZ constraint has an effect on the trajectory inside the approach corridor, even though the constraint is only enforced outside of the approach corridor. The effect is noticeable in both the thrust acceleration profile in Fig. 5.6 and the trajectory in Fig. 5.7. The reason for causing it is that the chaser arrives at the ADA point with different velocity when the KOZ constraint is added, which results in the different control profiles since then.

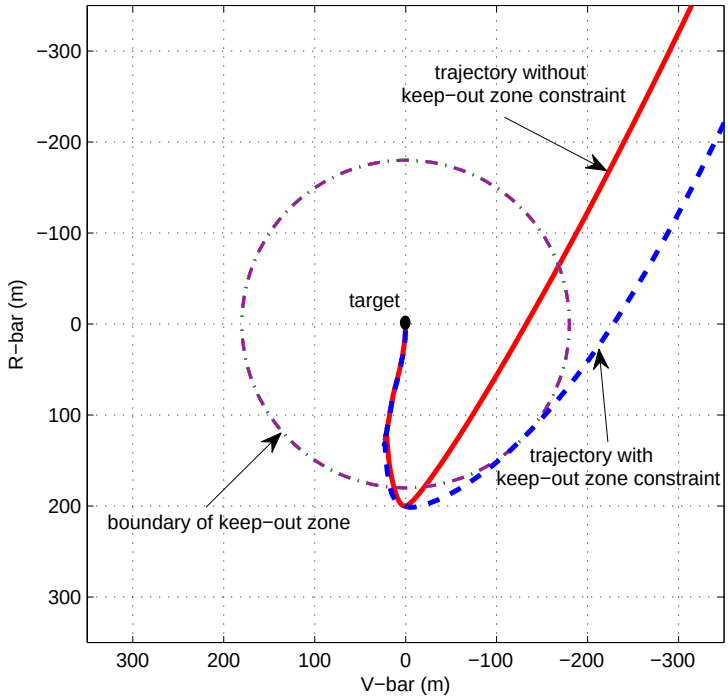

Figure 5.7 The PRO relative trajectory when the target and the chaser are in close range, R-bar approach.

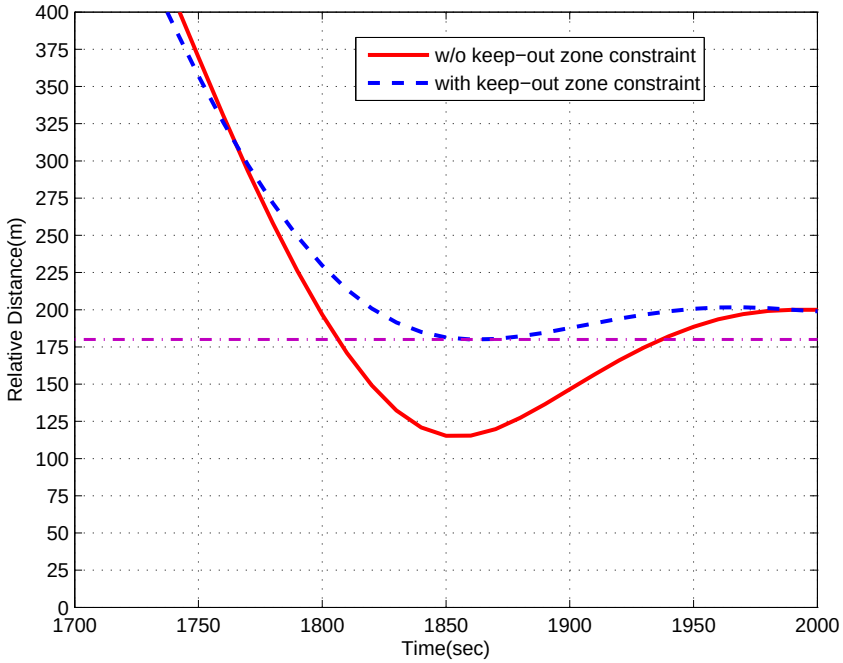

Figure 5.8 The relative distance between the chaser and the target.

CHAPTER 6. NONLINEAR TERMINAL CONSTRAINTS

6.1 Introduction

The previous chapter proposes a methodology to handle the concave inequality constraint which is not directly applicable in SOCP. This chapter focuses on the next topic on nonlinear state terminal equality constraints, which are also not allowed in the frame of SOCP. A majority of practical aerospace problems will have nonlinear terminal constraints as opposed to linear ones. Within the same successive-solution, SOCP-based methodology, a two-step approach is developed in this chapter to treat nonlinear equality constraints. In each iteration, the first step is to approximate the nonlinear constraints by their first-order expansions in the problem. A second-order correction is computed for each constraint based on the result from the first step. The problem is then solved with linearized equality constraints that are now compensated with the second-order corrections. The testing results show convergence behavior typical of superlinearly convergent methods. The second-order corrections are found to be critical for enhancing the reliability of convergence. The approach proves to be effective and successful even in some difficult problems known for high sensitivity. While this dissertation uses the systems with linear, time-varying dynamics as the baseline model in the presentation of the development, the method is equally applicable to nonlinear equality constraints in a discretized problem arising from nonlinear state equations.

6.2 Problem Formulation

Based on the problem PP($\boldsymbol{y}^{[k]}$) in Chapter 5 where the collision avoidance constraints are linearized, we add one more type of constraints that is from the nonlinear terminal constraints discussed in Section 6.1 and form the problem as follows [56]:

$$\text{minimize} \quad \boldsymbol{c}^T\boldsymbol{y} \tag{6.1}$$

$$\text{subject to} \quad H\boldsymbol{y} \leq \boldsymbol{p} \tag{6.2}$$

$$g_i(\boldsymbol{y}^{[k]}) + \nabla g_i(\boldsymbol{y}^{[k]})^T(\boldsymbol{y} - \boldsymbol{y}^{[k]}) \leq 0,\ i = 1, \ldots, l \tag{6.3}$$

$$h_i(\boldsymbol{y}) = 0,\ i = 1, \ldots, q \tag{6.4}$$

Here we do not have the second-order cone constraint (5.16) to simplify the problem. If it is assumed that at the optimal solution $\boldsymbol{y}^*$ of problem (6.1)–(6.4) the active inequality constraints are known. Then when $\boldsymbol{y}^{[k]}$ is sufficiently close to $\boldsymbol{y}^*$, the problem will have the same active constraints as those at $\boldsymbol{y}^*$. Those inactive inequality constraints at $\boldsymbol{y}^*$ can be ignored, so are those in problem (6.1)–(6.4). The active ones can be treated as equality constraints [18]. So it is enough to consider only equality constraints and we consider the problem in the form of

$$\text{P}^2\text{:} \quad \text{minimize} \quad \boldsymbol{c}^T\boldsymbol{y} \tag{6.5}$$

$$\text{subject to} \quad h_i(\boldsymbol{y}) = 0,\ i = 1, \ldots, q \tag{6.6}$$

The active linear inequality constraint from Eq. (6.2)–(6.3) can be easily incorporated to the above problem and for notation simplicity the form of the above problem is considered.

6.3 Algorithm

A popular method to solve problem P^2 is the well-known SQP approach [18, 19] which solves a sequence of quadratic programming subproblems. The SQP method is

equivalent to applying the Newton's method to solve the first-order optimality conditions (or KKT conditions) of P^2, hence has the same local superlinear or quadratic convergence properties as the Newton's method does [19], depending on the assumptions on the problem data. In the SQP subproblems, the nonlinear equality constraints (6.6) are approximated by their linearized versions. But the curvatures (second-order terms) of the constraints are included in the objective functions of the subproblems. Our intention is to devise an algorithm that retains a similar consideration of the second-order influence in treating the nonlinear equality constraints, but otherwise can be readily integrated into the successive SOCP-solution framework described in Chapter 5 when other constraints are included. Such will require the objective functions of the subproblems to remain linear. Toward this end, the nonlinear equality constraints will be handled by successive linearization with second-order corrections in the following development.

To make the treatment to the nonlinear equality constraints amendable to a SOCP-based method, we seek to approximate $h_i(\boldsymbol{y}) = 0$ by

$$h_i(\boldsymbol{y}^{[k]}) + \nabla h_i^T(\boldsymbol{y}^{[k]})(\boldsymbol{y} - \boldsymbol{y}^{[k]}) + h_i^c(\boldsymbol{y}^{[k]}) = 0 \tag{6.7}$$

where $h_i^c(\boldsymbol{y}^{[k]})$ is the correction that is an approximation to the second-order term in the second-order Taylor series of $h_i(\boldsymbol{y})$ about $\boldsymbol{y}^{[k]}$

$$h_i(\boldsymbol{y}) = h_i(\boldsymbol{y}^{[k]}) + \nabla h_i^T(\boldsymbol{y}^{[k]})(\boldsymbol{y} - \boldsymbol{y}^{[k]}) + \frac{1}{2}(\boldsymbol{y} - \boldsymbol{y}^{[k]})^T \nabla^2 h_i(\boldsymbol{y}^{[k]})(\boldsymbol{y} - \boldsymbol{y}^{[k]}) \tag{6.8}$$

The key requirements for the corrections are that no computation of the Hessian $\nabla^2 h_i(\boldsymbol{y}^{[k]})$ is required, and the correction h_i^c depends only on $\boldsymbol{y}^{[k]}$, but not $\boldsymbol{y}$. The approach we take relies on a two-step solution procedure. In the first step, $h_i^c = 0$ is used in Eq. (6.7) and the following problem is solved

$$\mathrm{P}^3: \qquad \min_{\boldsymbol{y}} \quad \boldsymbol{c}^T\boldsymbol{y} \tag{6.9}$$

$$\text{subject to} \quad h_i(\boldsymbol{y}^{[k]}) + \nabla h_i^T(\boldsymbol{y}^{[k]})(\boldsymbol{y} - \boldsymbol{y}^{[k]}) = 0, \qquad i = 1, \ldots, q \tag{6.10}$$

Let the solution to Problem P^3 be $\boldsymbol{y}^p$. Note that $\boldsymbol{y}^p$ is dependent on $\boldsymbol{y}^{[k]}$, but nothing else in a given problem. Next, consider the first-order expansion of the gradient $\nabla h_i(\boldsymbol{y}^p)$ at $\boldsymbol{y}^{[k]}$:

$$\nabla h_i(\boldsymbol{y}^p) - \nabla h_i(\boldsymbol{y}^{[k]}) = \nabla^2 h_i(\boldsymbol{y}^{[k]})(\boldsymbol{y}^p - \boldsymbol{y}^{[k]}) \tag{6.11}$$

The gradient $\nabla h_i(\boldsymbol{y}^p)$ can be analytically computed, given $\boldsymbol{y}^p$. Left-multiplying both sides of the above equation with $(\boldsymbol{y}^p - \boldsymbol{y}^{[k]})^T/2$ gives

$$\frac{1}{2}(\boldsymbol{y}^p - \boldsymbol{y}^{[k]})^T \left(\nabla h_i(\boldsymbol{y}^p) - \nabla h_i(\boldsymbol{y}^{[k]}\right) = \frac{1}{2}(\boldsymbol{y}^p - \boldsymbol{y}^{[k]})^T \nabla^2 h_i(\boldsymbol{y}^{[k]})(\boldsymbol{y}^p - \boldsymbol{y}^{[k]}) \tag{6.12}$$

Hence a logical choice of the correction in Eq. (6.7) should be

$$h_i^c(\boldsymbol{y}^{[k]}) = \frac{1}{2}(\boldsymbol{y}^p - \boldsymbol{y}^{[k]})^T \left(\nabla h_i(\boldsymbol{y}^p) - \nabla h_i(\boldsymbol{y}^{[k]})\right) \tag{6.13}$$

By Eq. (6.12), this correction is a second-order correction. An alternate form of the correction can also be obtained by using $\boldsymbol{y} = \boldsymbol{y}^p$ in Eq. (6.8) to get an approximation to the second-order term as

$$h_i^c(\boldsymbol{y}^{[k]}) = h_i(\boldsymbol{y}^p) - h_i(\boldsymbol{y}^{[k]}) - \nabla h_i^T(\boldsymbol{y}^{[k]})(\boldsymbol{y}^p - \boldsymbol{y}^{[k]}) \tag{6.14}$$

For a quadratic function $h_i(\boldsymbol{y}) = \boldsymbol{y}^T H \boldsymbol{y} + \boldsymbol{b}^T \boldsymbol{y}$, both corrections in Eqs. (6.13) and (6.14) yield the exact second-order term $(\boldsymbol{y}^p - \boldsymbol{y}^{[k]})^T H (\boldsymbol{y}^p - \boldsymbol{y}^{[k]})$ in the Taylor series expansion without any approximation. Still, it is clear that Eqs. (6.13) and (6.14) are not the same for non-quadratic (and nonlinear) functions. In fact, if the gradient $\nabla h_i(\boldsymbol{y}^p)$ in Eq. (6.13) is approximated by the rank-one update first derived as Eq. (10) in Ref. [60]

$$\nabla h_i(\boldsymbol{y}^p) = \nabla h_i(\boldsymbol{y}^{[k]}) + \frac{2}{\delta \boldsymbol{y}^T \delta \boldsymbol{y}} \left(h_i(\boldsymbol{y}^p) - h_i(\boldsymbol{y}^{[k]}) - \nabla h_i^T(\boldsymbol{y}^{[k]}) \delta \boldsymbol{y}\right) \delta \boldsymbol{y} \tag{6.15}$$

where $\delta \boldsymbol{y} = \boldsymbol{y}^p - \boldsymbol{y}^{[k]}$, then Eq. (6.13) becomes exactly Eq. (6.14)! It is interesting to note that if the coefficient "2" in Eq. (6.15) is changed to 1, this equation reduces to the famous *Broyden rank-one update* [61]. But it is shown in Ref. [60] that the update in Eq. (6.15) is more accurate than the Broyden rank-one update. In the testing we

have done so far, no practically significant performance difference has been detected between using the correction in Eq. (6.13) or (6.14). Other applications, however, may favor one over the other. For instance, if the number of equality constraints is large, the computation required for the correction in Eq. (6.14) will be considerably less than Eq. (6.13) because no computation of the gradient $\nabla h_i(\boldsymbol{y}^p)$ is needed.

With the correction h_i^c obtained, the following problem is solved as the second step

$$\mathrm{P}^4: \qquad \min_{\boldsymbol{y}} \quad \boldsymbol{c}^T\boldsymbol{y} \tag{6.16}$$

$$\text{subject to} \quad h_i(\boldsymbol{y}^{[k]}) + \nabla h_i^T(\boldsymbol{y}^{[k]})(\boldsymbol{y}-\boldsymbol{y}^{[k]}) + h_i^c(\boldsymbol{y}^{[k]}) = 0, \qquad i = 1,\ldots,q \tag{6.17}$$

The solution to Problem P^4 is set to be $\boldsymbol{y}^{[k+1]}$.

The numerical evidences from our tests suggest superlinear local convergence of the solution of Problem P^4 to that of Problem P^2, even though no rigorous proof is available yet. It should be pointed out that faster convergence is not the only motivation for using the second-order corrections. For our purposes the benefit of potentially enhanced robustness in convergence is arguably more important. We have encountered cases (see Section 6.4 later) where the solution approach succeeds with the second-order corrections, but would fail to converge to satisfy the nonlinear constraints without the corrections.

As with any other methods utilizing constraint linearization, there is a possibility for Eq. (6.10) to be inconsistent with other constraints in the problem (when they are present), especially during the earlier iterations, even if the original nonlinear constraints are consistent with other constraints. To find a remedy to ameliorate this possibility, we stress that our goal is not to completely satisfy the original nonlinear constraints in each iteration, which is actually impossible to be achieved by an algorithm. Existence of infeasibility is acceptable, but we expect that the feasibility of the constraints is improved in each iteration and finally the constraints are accurately satisfied. Therefore a relaxation term may be added to Eq. (6.10)

$$h_i(\boldsymbol{y}^{[k]}) + \nabla h_i^T(\boldsymbol{y}^{[k]})(\boldsymbol{y} - \boldsymbol{y}^{[k]}) = \gamma h_i(\boldsymbol{y}^{[k]}) \tag{6.18}$$

where $\gamma \in (0, 1)$ is a constant. Typically $\gamma = 0.01$ is used. The term $\gamma h_i(\boldsymbol{y}^{[k]})$ in the above equation means that the accuracy of the approximation of $h_i(\boldsymbol{y})$ at the current iteration is γ times the value of $h_i(\boldsymbol{y})$ from the previous iteration. So the goal of Eq. (6.18) is to improve the feasibility based on the actual value of $h_i(\boldsymbol{y})$.

While the above discussion focuses on only nonlinear equality constraints, there is no conceptual or methodological difficulty to include linear inequality and second-order-cone constraints in the problem. Therefore the problem with both concave inequality constraints and nonlinear terminal constraints can be solved by seeking successively the solution of the following SOCP problem

$$\mathrm{P}^5(\boldsymbol{y}^{[k]}): \quad \min_{\boldsymbol{y}} \quad \boldsymbol{c}^T\boldsymbol{y} \tag{6.19}$$

$$\text{subject to} \quad H\boldsymbol{y} \le \boldsymbol{p} \tag{6.20}$$

$$g_i(\boldsymbol{y}^{[k]}) + \nabla g_i^T(\boldsymbol{y}^{[k]})(\boldsymbol{y} - \boldsymbol{y}^{[k]}) \le 0, \ i = 1, \ldots, l \tag{6.21}$$

$$h_i(\boldsymbol{y}^{[k]}) + \nabla h_i^T(\boldsymbol{y}^{[k]})(\boldsymbol{y} - \boldsymbol{y}^{[k]}) + h_i^c(\boldsymbol{y}^{[k]}) = 0, \ i = 1, \ldots, q \tag{6.22}$$

$$A\boldsymbol{y} - \boldsymbol{b} \ge_{\bar{K}} 0 \tag{6.23}$$

where in each iteration, Problem P^5 is first solved with $h_i^c = 0$ in Eq. (6.22). Then the corrections $h_i^c(\boldsymbol{y}^{[k]})$ are constructed by Eq. (6.13) or (6.14); Problem P^5 is solved again with the computed h_i^c in Eq. (6.22), and the next iterate $\boldsymbol{y}^{[k+1]}$ is found.

So far the nonlinear inequality constraints in Eq. (6.22) have been regarded to have originated from the nonlinear terminal constraints. But the discretized problem will have the same form as in Eqs. (6.19)–(6.23) if the nonlinear inequality constraints in Eq. (6.22) arise from any other sources in the original problem, including *nonlinear state equations* (only in such a case the dimension q will be large). Therefore, the methodology

developed here can be applied in principle to optimal control problems with nonlinear dynamics as well.

6.4 Applications

In this section, the algorithm proposed in the previous section will be applied to some practical applications where there are nonlinear terminal constraints. To further show the effectiveness of the algorithm, problems with both concave inequality constraints (or collision avoidance constraints here) and nonlinear terminal constraints will also be considered.

6.4.1 McCue's Orbital Transfer Problem

McCue's problem of finite-thrust orbital transfer [62] is one in which the fuel-optimal transfer is sought between two coplanar elliptic orbits whose apsidal axes are not aligned. This type of problems are reported to be extremely sensitive and require the initial guesses to be very close to the optimal solutions when solved by more traditional approaches [62], which makes them good tests to demonstrate the capability of the proposed method for handling nonlinear terminal equality constraints even in highly sensitive problems.

In orbital transfer problems position and velocity usually vary greatly, and in general no close trajectory is available *a priori* to serve as a reference for linearization of the nonlinear trajectory dynamics. To overcome this inconvenience, the same techniques discussed in Chapter 3 for the RPO problems are used here for orbital transfer problems. Let $\boldsymbol{\tau}$ be the thrust acceleration vector of the engine:

$$\boldsymbol{\tau} = \frac{\boldsymbol{T}}{m} \tag{6.24}$$

where $\boldsymbol{T}$ is the thrust-vector-to-initial-weight of the rocket engine, and m the current mass of the vehicle normalized by its initial mass. Define $z = \ln m$ and σ a relaxation

variable representing the thrust-acceleration magnitude in g. The relaxed dimensionless three-degree-of-freedom equations of motion of the spacecraft in an inverse-square gravity field are

$$\dot{\boldsymbol{r}} = \boldsymbol{V} \tag{6.25}$$

$$\dot{\boldsymbol{V}} = -\frac{1}{\|\boldsymbol{r}\|^3}\boldsymbol{r} + \boldsymbol{\tau} \tag{6.26}$$

$$\dot{z} = -\frac{1}{v_{ex}}\sigma \tag{6.27}$$

For the meaning of each variable and the normalization factors, refer to chapter 3 for details. Let $\boldsymbol{x} = (\boldsymbol{r}^T\ \boldsymbol{V}^T\ z)^T$ be the state vector of the above system, and $\boldsymbol{u} = (\boldsymbol{\tau}^T\ \sigma)^T \in R^4$ the control vector. The above state equations can be cast as

$$\dot{\boldsymbol{x}} = \begin{bmatrix} 0_{3\times3} & I_{3\times3} & 0_{3\times1} \\ -\frac{1}{r^3}I_{3\times3} & 0_{3\times3} & 0_{3\times1} \\ 0_{1\times3} & 0_{1\times3} & 0 \end{bmatrix} \boldsymbol{x} + \begin{bmatrix} 0_{3\times3} & 0_{3\times1} \\ I_{3\times3} & 0_{3\times1} \\ 0_{1\times3} & -1/v_{ex} \end{bmatrix} \boldsymbol{u} =: A(r)\boldsymbol{x} + B\boldsymbol{u} \tag{6.28}$$

Two constraints that limit the engine thrust acceleration to its given finite upper bound and define the relaxation relationship are

$$0 \le \sigma \le T_{max}e^{-z} \tag{6.29}$$

$$\|\boldsymbol{\tau}\| \le \sigma \tag{6.30}$$

The propellant consumption performance index is

$$J = \int_0^{t_f} \sigma dt \tag{6.31}$$

Let the specified nonlinear terminal conditions be

$$\psi_i(\boldsymbol{x}(t_f)) = 0, \quad i = 1, \ldots, n_\psi \le 6 \tag{6.32}$$

When $\sigma(t) \equiv \|\boldsymbol{\tau}(t)\|$ the above relaxed problem is the same as the the original rocket flight problem (see Ref. [9]). It can be proved by following the same proofs in Ref [9] that the above relaxed problem in Eqs. (6.28)–(6.32) has the same optimal solution as

the original optimal orbital transfer problem with the same rocket, initial condition and terminal constraints. The advantage of the relaxed problem is that the state equations (6.28) are "almost" linear, with the single nonlinearity $1/r^3$ in the A matrix. However, in the k+1-th iteration of the successive solution process, if $r(t)$ is replaced by the $r^{[k]}(t) = \|\boldsymbol{r}^{[k]}(t)\|$ obtained in the previous iteration, $A(r^{[k]}(t))$ becomes an explicit time-varying matrix, and the system (6.28) will be linear in each iteration. When convergence occurs, the solution will be the same (to the extent of the solution accuracy) as that to Eq. (6.28). Such is the strategy used in order to employ the SOCP method.

To apply the proposed method to solve a McCue's orbital transfer problem, consider a spacecraft in an initial orbit with a semi-major axis $a_0 = 7531.211$ km (perigee altitude of 400 km), eccentricity of $e_0 = 0.1$, orbital inclination of $i_0 = 51.6$ deg, right ascension of ascending node $\Omega_0 = 119.82$ deg, and argument of perigee $\omega_0 = 51$ deg. The engine of the spacecraft has an initial thrust-to-weight ratio of 0.4 and a specific impulse of 320 sec. At $t_0 = 0$, the spacecraft is in this orbit with a true anomaly $\nu = 175$ deg. The spacecraft is required to transfer to another co-planar orbit which has the same semi-major axis and eccentricity, but a different argument of perigee of $\omega_f = 170$ deg. The total transfer time is prescribed to be $t_f = 1700$ sec. Therefore, the terminal constraints for entering the target orbit are (note that everything below is dimensionless)

$$\sqrt{(\boldsymbol{r}_f \times \boldsymbol{V}_f)^T(\boldsymbol{r}_f \times \boldsymbol{V}_f)} - h_f = 0 \tag{6.33}$$

$$0.5\boldsymbol{V}_f^T\boldsymbol{V}_f - \frac{1}{\|\boldsymbol{r}_f\|} + \frac{1}{2a_f} = 0 \tag{6.34}$$

$$\mathbf{1}_h^T\boldsymbol{r}_f = 0 \tag{6.35}$$

$$\mathbf{1}_h^T\boldsymbol{V}_f = 0 \tag{6.36}$$

$$\boldsymbol{n}^T\boldsymbol{e}_f - e_f\cos(\omega_f) = 0 \tag{6.37}$$

where the subscript "f" means the final value in the target orbit, $\boldsymbol{r}_f$ and $\boldsymbol{V}_f$ are the final position and velocity vector of the spacecraft in the GEI frame. The constant

$h_f = \sqrt{a_f(1-e_f^2)}$ is the required magnitude of angular momentum, $a_f = a_0$ and $e_f = e_0$ as specified. The constant unit vector $\mathbf{1}_h$ is in the direction of the norm to the desired target orbital plane. In the GEI frame,

$$\mathbf{1}_h = [\sin\Omega_f \sin i_f \;\; -\cos\Omega_f \sin i_f \;\; \cos i_f]^T$$

where $\Omega_f = \Omega_0$ and $i_f = i_0$ for this problem. The nodal vector $\boldsymbol{n} = [0,\, 0,\, 1]^T \times \mathbf{1}_h$ is another constant unit vector. The eccentricity vector $\boldsymbol{e}_f$ points to the direction of perigee in the target orbital plane, and is defined by

$$\boldsymbol{e}_f = (V_f^2 - \frac{1}{r_f})\boldsymbol{r}_f - (\boldsymbol{r}_f^T \boldsymbol{V}_f)\boldsymbol{V}_f$$

Equations. (6.33)–(6.34) constrain the final eccentricity and semi-major axis. The constraints on i_f and Ω_f are enforced by Eqs. (6.35)–(6.36). Finally Eq. (6.37) ensures that the required ω_f for the target orbit is achieved. But the location to insert into the target orbit is left free, as part of the optimal solution to be found. Three of the five terminal constraints, i. e., Eqs. (6.33), (6.34) and (6.37), are nonlinear.

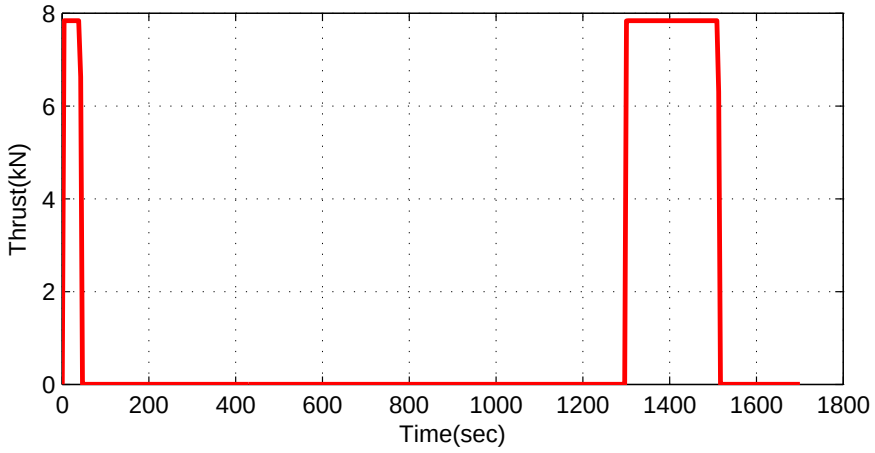

Figure 6.1 The thrust magnitude profile for the McCue's orbital transfer problem

A discussion on the implication of the prescribed final time is in order. The McCue's problem is posed as a free-time transfer problem in Ref. [62]. The optimal solution is supposed to find the optimal transfer time as part of the solution. But it is argued in

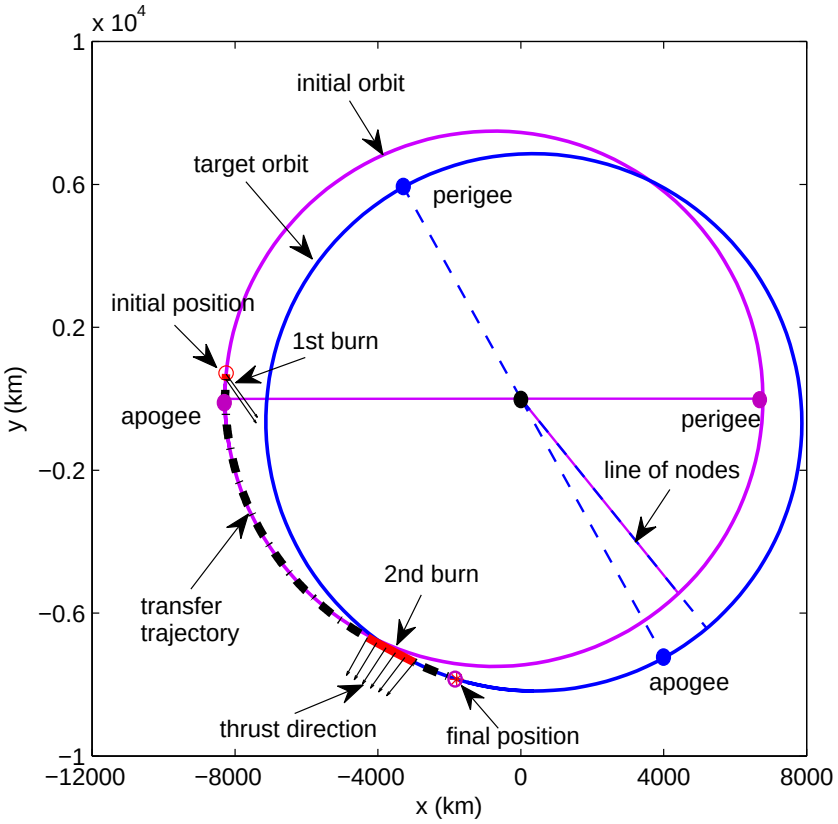

Figure 6.2 Transfer trajectory in the McCue's problem with the locations of the two burns and the thrust vector direction

Ref. [63] that such a free-time multiple-finite-burn problem in an inverse-square gravity field actually *has no fuel-optimal solution*. This peculiarity is caused by the periodicity of the elliptical orbit: the condition at any point on an elliptical orbit will be repeated after any number of orbits if the engine is shut off. See Ref. [63] for detail. To "regularize" the problem so a meaningful optimal solution can be found, one option is to set an upper bound on the time of flight. The prescribed $t_f = 1700$ sec can be interpreted as the upper bound for this problem. If the optimal solution turns out to inject into the target orbit before 1700 sec, the optimal solution should have the engine shut off right at the point. The spacecraft will simply coast on the final orbit until $t_f = 1700$ without incurring any unnecessary additional fuel expenditure, while the orbital elements remain unchanged. The same argument applies to any other orbital transfer problems in the

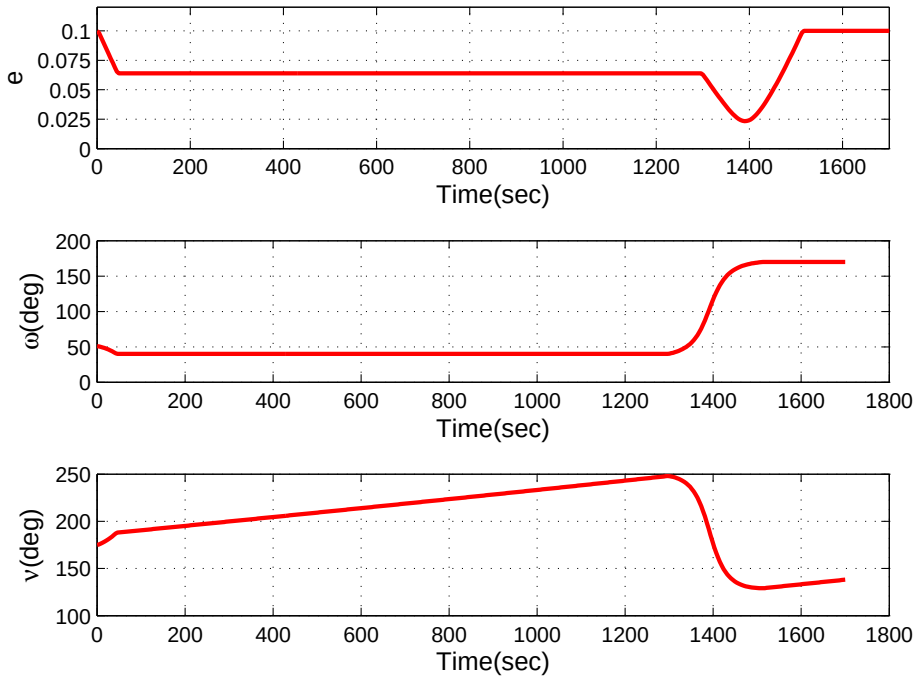

Figure 6.3 The changes of eccentricity e, argument of perigee ω, and true anomaly ν along the transfer trajectory in the McCue's problem

context of Keplerian motion, provided that all the terminal conditions are specified in terms of the final orbital elements.

The optimal control problem is then to find the optimal engine ignition program (when to burn, how many times, for how long), the thrust magnitude, and the direction of the thrust vector during an engine burn, so that the nonlinear terminal constraints in Eqs. (6.33)–(6.37) are satisfied, and the propellant consumption is minimized. As long as the solution contains one or more coast arcs, this minimum-fuel problem is well posed even though the final time is specified. The method proposed in Section 6.3 in conjunction with the relaxation technique described in the first half of this section is used to solve this problem.

Figure 6.1 shows the optimal thrust magnitude profile. The optimal solution starts engine burn immediately in this case. The optimal solution is a two-burn solution at

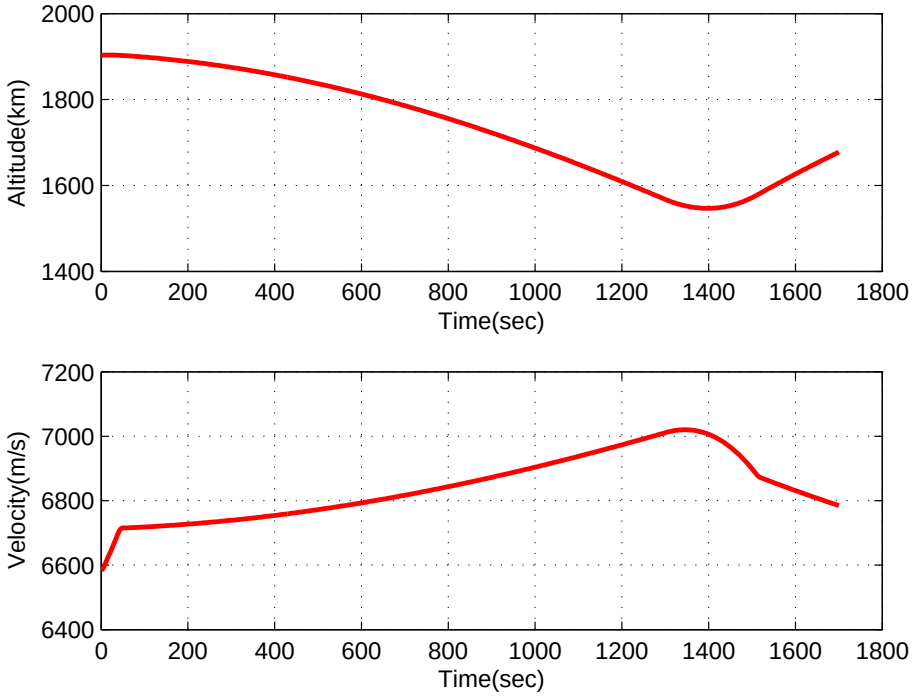

Figure 6.4 Altitude and velocity along the transfer trajectory in the McCue's problem

maximum thrust, and the first burn is quite short. After a long coast, the second burn lasts about 200 seconds and indeed finishes before $t_f = 1700$ sec. For the last 140 seconds or so the solution is a coast arc, indicating that the upper bound $t_f = 1700$ sec is already sufficiently long. The transfer trajectory in the specified orbital plane is plotted in Fig. 6.2. Note that the solution got from solving the problem (6.28)–(6.32) is expressed in the GEI coordinate system, which is in 3-dimension. The solution is transformed to the perifocal coordinate system by using the method discussed in Section 2.3.2 in Chapter 2.

It is seen In Fig. 6.2 that the first burn is far from the intersection of the initial and target orbits. Evidently a solution with a single-burn near the intersection of the orbits is not optimal in this case. The direction of the thrust vector is also shown in Fig. 6.2. The first burn is in the general direction of the orbital motion to help increase the velocity. The direction of the second burn is almost perpendicular to the

trajectory, suggesting that its main function is to adjust the shape of the osculating orbit, not to change the energy. The changes of eccentricity, argument of perigee and true anomaly of the osculating orbit along the transfer trajectory are shown in Fig. 6.3. Note the major variations in all the 3 parameters during the second burn. Figure 6.4 illustrates the variations of the altitude and velocity, where a short but quick increase in velocity during the first burn is clear. All the nonlinear terminal equality constraints in Eqs. (6.33)–(6.37) are satisfied to the specified accuracy.

Even though only one case is presented here, a number of different cases in the McCue's problem with different data have been successfully solved using the proposed method. It should be stressed that the second-order corrections developed in Section 6.3 proves to be instrumental for producing reliable convergence in this highly sensitive problem. Without the second-order corrections, the algorithm would have difficulty to converge in most cases of the McCue's problem.

6.4.2 Optimal Launch Ascent Problem

In this application the capability of simultaneously handling concave state inequality constraints and nonlinear terminal equality constraints by the proposed algorithm is demonstrated. The problem is ascent of the upper stage of a medium-lift launch vehicle. The initial condition is given as that at the burnout of the previous stage of the vehicle. Since the initial altitude (of 86 km) is already sufficiently high, the optimal ascent problem is formulated as a vacuum ascent problem. As such, the dynamics and performance index are the same as in Eqs. (6.25)–(6.31) in the Section 6.4.1. The same successive solution approach is also used to treat the A matrix in Eq. (6.28) as an explicitly time-varying one in each iteration, and then updated for the next iteration.

The initial thrust-to-weight ratio of the upper stage of the launch vehicle is 1.45. The initial mass is given. The final orbit is one with $e = 0.05$, perigee altitude of 400 km, and

$i = 51.6$ deg. The arguments of ascending node and perigee are free. The insertion point is specified to be at the perigee of the final orbit. The nonlinear terminal constraints on the final position and velocity vectors are then

$$\sqrt{\boldsymbol{r}_f^T \boldsymbol{r}_f} - r_f^* = 0 \tag{6.38}$$

$$\sqrt{\boldsymbol{V}_f^T \boldsymbol{V}_f} - V_f^* = 0 \tag{6.39}$$

$$[0 \;\; 0 \;\; 1](\boldsymbol{r}_f \times \boldsymbol{V}_f) - h_f^* \cos(i^*) = 0 \tag{6.40}$$

$$\boldsymbol{r}_f^T \boldsymbol{V}_f = 0 \tag{6.41}$$

where r_f^* and V_f^* are the required radius (corresponding to an altitude of 400 km) and velocity at perigee of the specified orbit. Constraint (6.40) specifies the final orbital inclination at $i^* = 51.6$ deg, where h_f^* is the magnitude of the angular momentum of the final orbit. For insertion at perigee, $h_f^* = r_f^* V_f^*$. Condition (6.41) requires the final flight path angle to be zero (at perigee). The flight time (not the burn time) for the upper stage is prescribed to be 800 sec. The optimal control problem is to find the thrust program of the upper-stage engine (when to burn, how many times, for how long, at what thrust level) and the thrust vector direction so the terminal constraints (6.38)–(6.41) are met, a state inequality constraint to be described below is observed, and the final injected mass maximized (equivalent to minimizing propellant consumption for a given initial mass). Again, the *optimization* part of the problem is well posed as long as the solution has one or more coast arcs.

Suppose that the above problem is solved without any inequality constraints, and it is found that the resulting orbital insertion point is too close to another spacecraft that is already on a nearby orbit. Let this found insertion point be $\boldsymbol{r}_f^*$. An exclusion zone constraint is then imposed on the actual ascent trajectory

$$\delta - \|\boldsymbol{r}_f^* - \boldsymbol{r}(t)\| \leq 0 \tag{6.42}$$

where $\delta = 300$ km is chosen. This is a concave state inequality constraint. Now the problem is solved to meet the constraints in Eqs. (6.38)–(6.41) as well as Eq. (6.42). This problem has both elements of the non-convexity this dissertation intends to address.

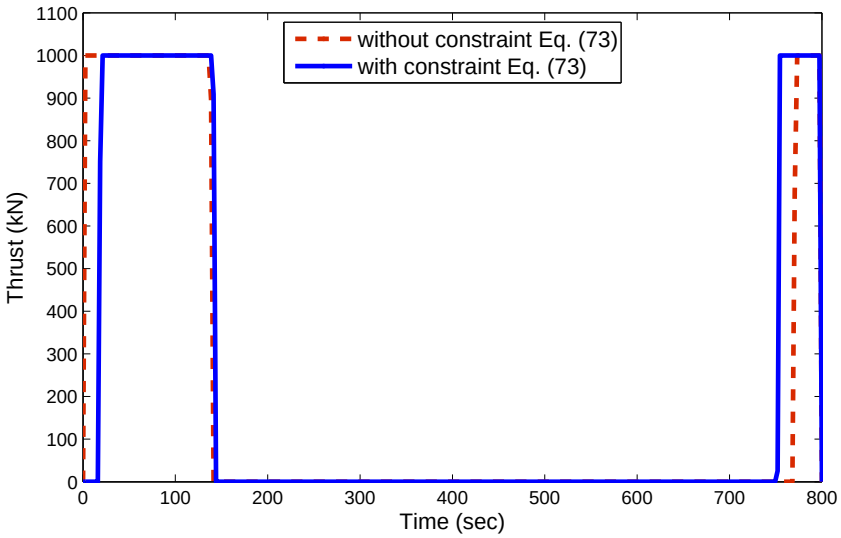

Figure 6.5 Thrust profiles for the launch ascent problem

The proposed algorithm solves this problem with complete ease. Figure 6.5 shows the optimal thrust profile. The optimal thrust profile without the constraint (6.42) is also plotted for comparison. The optimal solution is a two-burn maneuver at the maximum thrust with the first one considerably longer. It is interesting to note an initial coast of 16 seconds before the ignition of the engine for the first burn. The thrust profile without constraint (6.42) does not have such an initial coast. This initial coast mainly contributes to delay the ascent trajectory so the trajectory will terminate 300 km behind the position defined by $\boldsymbol{r}_f^*$. Figure 6.6 illustrates the zoom-in view near the end of the ascent trajectory. It is clear that the optimal ascent trajectory ends right on the boundary of the constraint (6.42), 300 km behind the position defined by $\boldsymbol{r}_f^*$, and this is the only point when the constraint (6.42) becomes active. Again, there is no conservativeness in satisfying the constraint (6.42), even though this is a case where nonlinear inequality terminal constraints are also present. Also evident from Fig. 6.6 is

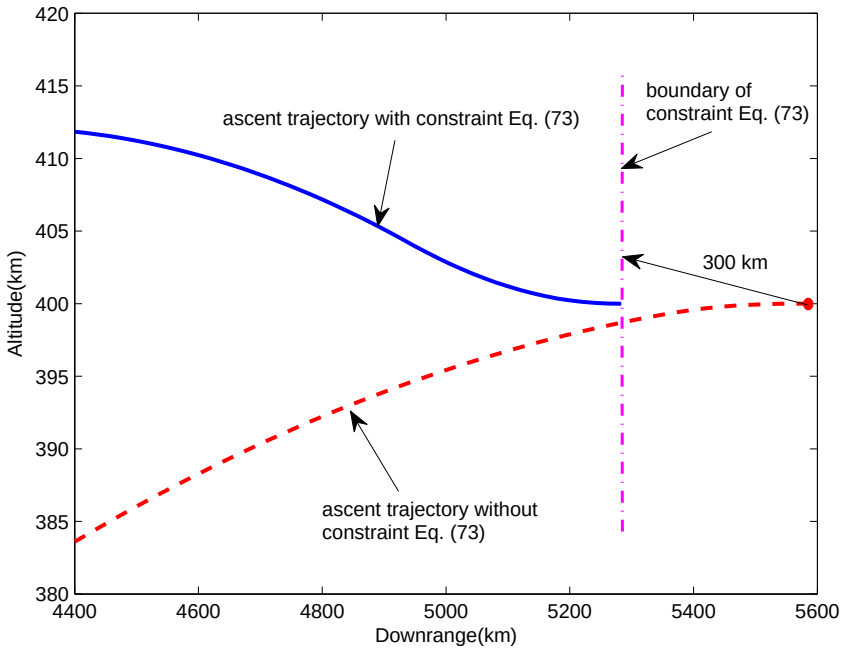

Figure 6.6 Zoom-in view at the end of the ascent trajectories

that the trajectory subject to constraint (6.42) ascends above the required final altitude of 400 km before descending to this prescribed value. Figure 6.7, which shows the altitude and velocity along the ascent trajectories, confirms just that. The variations of instantaneous eccentricity and orbital inclination along the ascent trajectories with and without constraint (6.42) are given in Fig. 6.8. Figures 6.7 and 6.8 clearly verify that the nonlinear terminal constraints in Eqs. (6.38)–(6.41) are all accurately satisfied.

The cost of imposing the state inequality constraint (6.42) is a reduction of 1.15% in the final injected mass, as compared to the case when constraint (6.42) is not imposed.

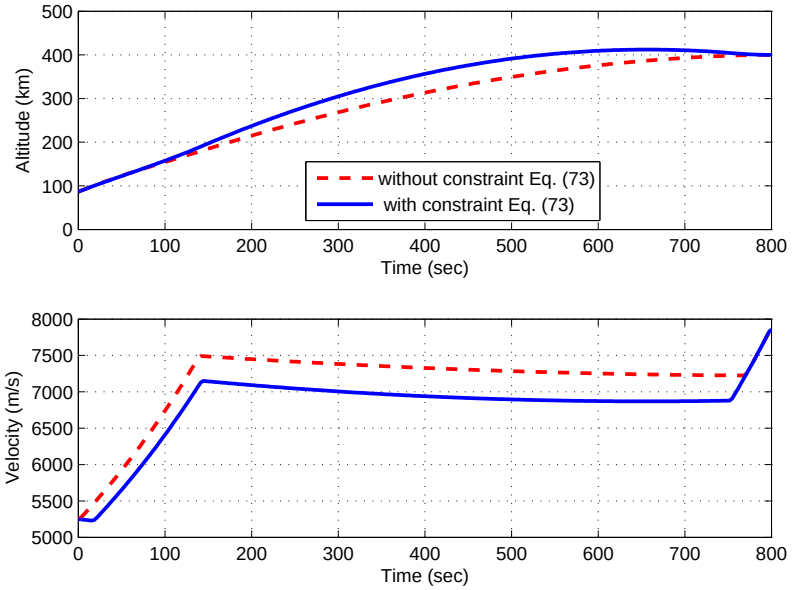

Figure 6.7 Altitude and velocity along the ascent trajectories

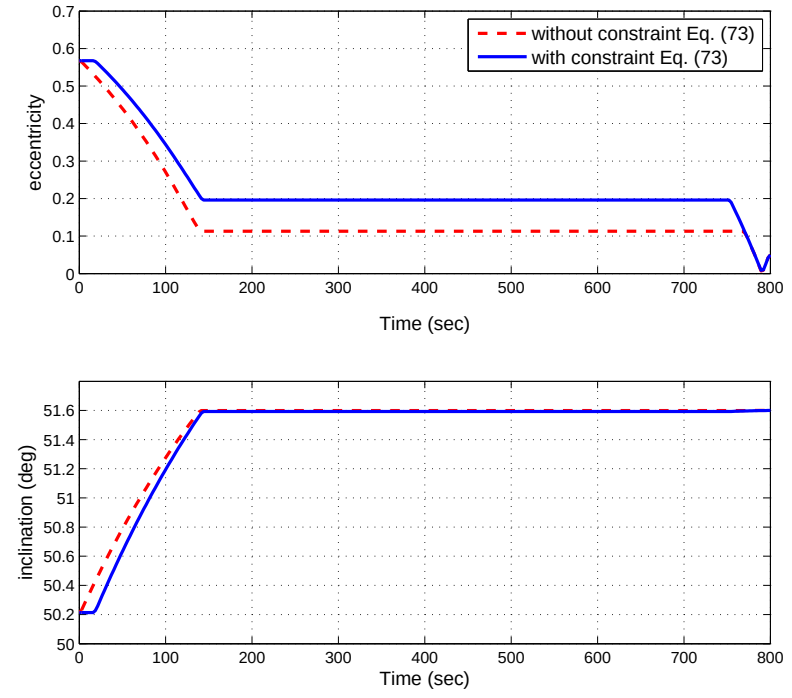

Figure 6.8 Osculating orbital eccentricity and inclination along the ascent trajectories

CHAPTER 7. PRIMAL-DUAL INTERIOR POINT METHOD

7.1 Introduction

The broad applications of SOCP have stimulated the research on algorithms for SOCP. The complexities of different variants of primal-dual algorithms were discussed in Refs. [64, 65]. The primal-dual path-following algorithm enjoys polynomial time convergence and upper bound on the total number of iterations could be pre-determined [66]. Furthermore, Ref. [28] studies a state-of-the-art primal-dual interior point method (IPM) which is robust and can handle the primal or dual infeasible problems in a systematic way. Similar work can also be found in Refs. [27, 32]. The primal-dual IPM does not require use-supplied initial guess and the solution obtained can provide certificate when either the primal problem or the dual problem is infeasible. This chapter gives a summary on the implementation of the primal-dual IPM, which is a basis for writing a customized solver for SOCP in order to improve computational efficiency and have more flexibility for specific applications.

7.2 The Goldman-Tucker Homogeneous Model

As introduced in Chapter 2, the primal SOCP problem can be expressed in standard form as follows:

$$\begin{aligned} P: \text{ minimize} \quad & c^T x \\ \text{subject to} \quad & Ax = b \\ & x \in K \end{aligned}$$

where $A \in R^{m\times n}$ with $rank(A) = m, m \leq n$, $x, c \in R^n, b \in R^m$, K is the Cartesian product of linear, quadratic or rotated quadratic cones and $K = K^{n_1} \times K^{n_2} \times \cdots \times K^{n_r}$ with n_i being the dimension of the cone K^{n_i}. If x is partitioned according to its components to the cones K^{n_i}, we have

$$x = \begin{bmatrix} x^{n_1} \\ x^{n_2} \\ \vdots \\ x^{n_r} \end{bmatrix} \tag{7.1}$$

The corresponding dual problem is given by:

$$\begin{aligned} D: \text{ maximize} \quad & b^T y \\ \text{subject to} \quad & A^T y + s = c \\ & s \in K^* \end{aligned}$$

where $s \in R^n$ is called the dual variable, and K^* is the dual cone of K.

Definition 7.2.1. *Assume K is a convex cone in R^n. Then the dual cone K^* of K is defined as*

$$K^* = \{s \in R^n \,:\, s^T x \geq 0, \forall x \in K\} \tag{7.2}$$

Assume $\bar{K}$ is a linear, quadratic or rotated quadratic cone, it is shown in Ref. [32] that $\bar{K}^* = \bar{K}$. Then, since the K in problem P is a combination of three three kinds of cones, it is implied that K^* in problem D is the same as K in problem P.

The weak duality theorem states that $c^T x \geq b^T y$, or $x^T s = c^T x - b^T y \geq 0$ [22, 32]. In addition, the complementarity gap $x^T s = 0$ implies that x is the optimal solution to problem P and (y, s) is the optimal solution to problem D.

Solving problem P is equivalent to solving the following system:

$$\begin{aligned} Ax - b &= 0, \quad x \in K \\ A^T y + s - c &= 0, \quad s \in K \\ x^T s &= 0 \end{aligned} \tag{7.3}$$

The above system is further equivalent to

$$\begin{aligned} Ax - b &= 0, \quad x \in K \\ A^T y + s - c &= 0, \quad s \in K \\ b^T y - c^T x &\geq 0 \end{aligned} \tag{7.4}$$

since $b^T y - c^T x \geq 0$ together with the fact that $c^T x - b^T y \geq 0$ yield $c^T x - b^T y = 0$, which is the complementarity condition $s^T x = 0$.

After adding a slack variable $\kappa \geq 0$ to the third equation in (7.4), obtained is the following linear system:

$$\begin{aligned} Ax - b &= 0, \quad x \in K \\ A^T y + s - c &= 0, \quad s \in K \\ b^T y - c^T x - \kappa &= 0 \end{aligned} \tag{7.5}$$

By homogenizing the above system, we consider the following Goldman-Tucker homogeneous model [32, 67]:

$$\begin{aligned} Ax - b\tau &= 0, \quad x \in K \\ A^T y + s - c\tau &= 0, \quad s \in K \\ b^T y - c^T x - \kappa &= 0 \end{aligned} \tag{7.6}$$

where the additional variable $\tau \geq 0$.

Denote (x, y, s, τ, κ) as the solution to (7.6), then

i) $x^T s + \tau\kappa = 0$.

ii) If $\tau > 0$, then x/τ is the optimal solution for P and $(y, s)/\tau$ is the optimal solution for D.

iii) If $\kappa > 0$, then either P or D is infeasible and at least one of the following inequalities

$$b^T y > 0 \tag{7.7}$$

and

$$c^T x < 0 \tag{7.8}$$

holds. The primal problem P is infeasible if Eq. (7.7) is satisfied, while D is infeasible if Eq. (7.8) holds. Proof for the above results can be found in Ref. [32].

In order to always have a feasible starting point when using interior-point method in solving the model in (7.6), the following optimization problem is considered [32]:

$$\begin{aligned} \text{minimize} \quad & \beta\gamma \\ \text{subject to} \quad & Ax - b\tau = \gamma r_p \\ & A^T y + s - c\tau = \gamma r_d \\ & b^T y - c^T x - \kappa = \gamma r_g \\ & r_p^T y - r_d^T x + r_g \tau = -\beta \end{aligned} \tag{7.9}$$

where $x, s \in K, \tau \geq 0, \kappa \geq 0$, y and γ are free, and for initial point $(x_0, y_0, s_0, \tau_0, \kappa_0)$,

$$\begin{aligned} r_p &= Ax_0 - b\tau_0 \\ r_d &= A^T y_0 + s_0 - c\tau_0 \\ r_g &= b^T y_0 - c^T x_0 - \kappa_0 \\ \beta &= -(r_p^T y_0 - r_d^T x_0 + r_g \tau_0) \end{aligned} \tag{7.10}$$

where (r_p, r_d, r_g) measure the primal-infeasibility, dual-infeasibility, and duality gap of the starting point, respectively.

For the optimization problem (7.9), it is self-dual and the optimal value is 0. In addition, $\beta\gamma = x^T s + \tau\kappa$ can be proved (See Ref. [32] for more details). So solving (7.9) is equivalent to find the solution of the following system:

$$\begin{aligned} Ax - b\tau &= \gamma r_p \\ A^T y + s - c\tau &= \gamma r_d \\ b^T y - c^T x - \kappa &= \gamma r_g \\ r_p^T y - r_d^T x + r_g \tau &= -\beta \\ x^T s + \tau\kappa &= 0 \end{aligned} \tag{7.11}$$

Furthermore, since the fourth equation in (7.11) is implied by the other four equations, it can be deleted from (7.11). Since $x^T s \geq 0$, $\tau\kappa \geq 0$, $x^T s + \tau\kappa = 0$ implies that $x^T s = 0$ and $\tau\kappa = 0$. Moreover, it is proved in Refs. [28, 32] that $x^T s = 0$ if and only if $XSe = 0$ with $X = mat(Tx), S = mat(Ts)$ where T for roated quadratic cone is defined in Section 2.1. For quadratic cone, T is identity matrix, while $T = 1$ for linear cone. Then (7.11) can be rewritten as:

$$\begin{aligned} Ax - b\tau &= \gamma r_p \\ A^T y + s - c\tau &= \gamma r_d \\ b^T y - c^T x - \kappa &= \gamma r_g \\ XSe &= 0 \\ \tau\kappa &= 0 \end{aligned} \tag{7.12}$$

In the primal-dual interior-point method(IPM), there exists a central path which the solution of the primal-dual problem should follow, which can be achieved by solving the

following system of equations:

$$\begin{aligned} Ax - b\tau &= \gamma r_p \\ A^T y + s - c\tau &= \gamma r_d \\ b^T y - c^T x - \kappa &= \gamma r_g \\ XSe &= \gamma \mu e \\ \tau\kappa &= \gamma\mu \end{aligned} \tag{7.13}$$

where μ is the gap measure, $\mu = (x^T s + \tau\kappa)/(k+1)$, k is the number of cones, between the primal objective and dual objective. when $\mu \to 0$, (7.13) is the same as (7.12). Actually, the solution from (7.13) is the one for (7.6) under the condition that $\mu \to 0$ and $(r_p, r_d, r_g) \to 0$.

It is obvious that (7.13) is a nonlinear system, so newton method can be applied to find its solution. With (r_p, r_d, r_g) defined in the current point (x, y, s, τ, κ), the moving direction $(\Delta x, \Delta y, \Delta s, \Delta\tau, \Delta\kappa)$ for the next point can be found by solving the following 1st-order linearized system:

$$\begin{aligned} A\Delta x - b\Delta\tau &= (\gamma - 1)(Ax - b\tau) \\ A^T\Delta y + \Delta s - c\Delta\tau &= (\gamma - 1)(A^T y + s - c\tau) \\ b^T\Delta y - c^T\Delta x - \Delta\kappa &= (\gamma - 1)(b^T y - c^T x - \kappa) \\ X(\Delta S)e + S(\Delta X)e &= \gamma\mu e - XSe \\ \tau\Delta\kappa + \kappa\Delta\tau &= \gamma\mu - \tau\kappa \end{aligned} \tag{7.14}$$

In the process of solving (7.14), a linear system in the form of $Ax = b$ needs to be solved. For the purpose of avoiding A to be singular and/or nonsymmetric to speed up finding the solution [32], scaling matrix Θ and W such that $(\Theta W)x = (\Theta W)^{-1}s$, with x being scaled by (ΘW) and s by $(\Theta W)^{-1}$, are introduced to (7.14) which is then rewritten

as:

$$\begin{aligned} A\Delta x - b\Delta\tau &= (\gamma-1)(Ax - b\tau) \\ A^T\Delta y + \Delta s - c\Delta\tau &= (\gamma-1)(A^Ty + s - c\tau) \\ b^T\Delta y - c^T\Delta x - \Delta\kappa &= (\gamma-1)(b^Ty - c^Tx - \kappa) \\ \bar{X}T(\Theta W)^{-1}\Delta s + \bar{S}T(\Theta W)\Delta x &= \gamma\mu e - \bar{X}\bar{S}e \\ \tau\Delta\kappa + \kappa\Delta\tau &= \gamma\mu - \tau\kappa \end{aligned} \tag{7.15}$$

where $\bar{X} = mat(T(\Theta W)x)$, $\bar{S} = mat(T(\Theta W)^{-1}s)$. See Ref. [28] for definitions of Θ and W. Note that $\bar{X}^{-1}\bar{S} = I$ since $(\Theta W)x = (\Theta W)^{-1}s$.

Let the next point be $(\bar{x}, \bar{y}, \bar{s}, \bar{\tau}, \bar{\kappa})$. It is easy to prove the relationship between the next point and the current point as follows [28]:

$$\begin{aligned} A\bar{x} - b\bar{\tau} &= (1+\alpha(\gamma-1))(Ax - b\tau) \\ A^T\bar{y} + \bar{s} - c\bar{\tau} &= (1+\alpha(\gamma-1))(A^Ty + s - c\tau) \\ b^T\bar{y} - c^T\bar{x} - \bar{\kappa} &= (1+\alpha(\gamma-1))(b^Ty - c^Tx - \kappa) \\ \bar{x}^T\bar{s} + \bar{\tau}\bar{\kappa} &= (1+\alpha(\gamma-1))(x^Ts + \tau\kappa) \end{aligned} \tag{7.16}$$

where $\alpha \in [0,1]$ is a step size, $\gamma \in [0,1]$ is updated at each iteration and $(\bar{x}, \bar{y}, \bar{s}, \bar{\tau}, \bar{\kappa}) = (x, y, s, \tau, \kappa) + \alpha(\bar{x}, \bar{y}, \bar{s}, \bar{\tau}, \bar{\kappa})$. It is seen from (7.16) that $(\mu, r_p, r_d, r_g) \to 0$ as long as $\gamma < 1$ and $\alpha > 0$ at each iteration, though the convergence speed is unknown, depending on how small γ is and how big α is.

7.3 Methods for Finding the Newton Search Direction

For notational convenience, we rewrite (7.15) as [32]:

$$A\Delta x - b\Delta\tau = r_1 \tag{7.17}$$

$$A^T\Delta y + \Delta s - c\Delta\tau = r_2 \tag{7.18}$$

$$b^T\Delta y - c^T\Delta x - \Delta\kappa = r_3 \tag{7.19}$$

$$\bar{X}T(\Theta W)^{-1}\Delta s + \bar{S}T(\Theta W)\Delta x = r_4 \tag{7.20}$$

$$\tau\Delta\kappa + \kappa\Delta\tau = r_5 \tag{7.21}$$

where

$$\begin{aligned} r_1 &= (\gamma-1)(Ax - b\tau) = (\gamma-1)r_p \\ r_2 &= (\gamma-1)(A^Ty + s - c\tau) = (\gamma-1)r_d \\ r_3 &= (\gamma-1)(b^Ty - c^Tx - \kappa) = (\gamma-1)r_g \\ r_4 &= \gamma\mu e - \bar{X}\bar{S}e \\ r_5 &= \gamma\mu - \tau\kappa \end{aligned} \tag{7.22}$$

There are three different ways of solving (7.17)–(7.21) to get the Newton search direction, the first of which is introduced as follows:

From Eq. (7.20), we have

$$\Delta s = \Theta WT\bar{X}^{-1}(r_4 - \bar{S})T\Theta W\Delta x$$

which can be rewritten as

$$\Delta s = \Theta WT\bar{X}^{-1}r_4 - (\Theta W)^2\Delta x \tag{7.23}$$

since $\bar{X}^{-1}\bar{S} = I$. Eq. (7.21) gives

$$\Delta\kappa = \tau^{-1}(r_5 - \kappa\Delta\tau) \tag{7.24}$$

Substituting Eqs. (7.23) and (7.24) into Eq. (7.18) and Eq. (7.19), we have

$$A^T\Delta y - (\Theta W)^2\Delta x - c\Delta\tau = r_2 - \Theta W T\bar{X}^{-1}r_4 := r_{22} \tag{7.25}$$

$$b^T\Delta y - c^T\Delta x + \frac{\kappa}{\tau}\Delta\tau = r_3 + \frac{r_5}{\tau} := r_{33} \tag{7.26}$$

Rearranging Eq. (7.25) yields

$$\Delta x = D^2(A^T\Delta y - c\Delta\tau - r_{22}) \tag{7.27}$$

where $D := (\Theta W)^{-1}$. Substituting Eq. (7.27) into Eq. (7.17) and Eq. (7.26) gives

$$AD^2A^T\Delta y - (AD^2c + b)\Delta\tau = r_1 + AD^2r_{22} := r_{11} \tag{7.28}$$

$$(b - AD^2c)^T\Delta y + (c^TD^2c + \frac{\kappa}{\tau})\Delta\tau = r_{33} - c^TD^2r_{22} := r_{333} \tag{7.29}$$

$\Delta\tau$ can be found from Eq. (7.29) as

$$\Delta\tau = \frac{1}{c^TD^2c + \kappa\tau^{-1}}(r_{333} - (b - AD^2c)^T\Delta y)$$

which can be written simply as

$$\Delta\tau = \frac{1}{a_1}(r_{333} - a_2^T\Delta y) \tag{7.30}$$

if we define $a_1 := c^TD^2c + \kappa\tau^{-1}$ and $a_2 := b - AD^2c$. Then, substitute Eq. (7.30) into Eq. (7.28) to get

$$AD^2A^T\Delta y + \frac{1}{a_1}(AD^2c + b)a_2^T\Delta y = r_{11} + \frac{1}{a_1}(AD^2c + b)r_{333} := r_{111}$$

which can be further rewritten as

$$(AD^2A^T + \bar{a}\hat{a}^T)\Delta y = r_{111} \tag{7.31}$$

if we define $\bar{a} := AD^2c + b$ and $\hat{a} := \frac{a_2}{a_1}$. From Eq. (7.31), we have

$$\Delta y = (AD^2A^T)^{-1}r_{111} - \frac{\hat{a}^T(AD^2A^T)^{-1}r_{111}(AD^2A^T)^{-1}\bar{a}}{1 + \hat{a}^T(AD^2A^T)^{-1}\bar{a}} \tag{7.32}$$

It is seen from Eq. (7.32) that we need to compute

$$(AD^2A^T)^{-1}r_{111} := v_0 \tag{7.33}$$

and

$$(AD^2A^T)^{-1}\bar{a} := v_1 \tag{7.34}$$

In Eqs. (7.33) and (7.34), AD^2A^T is symmetric and positive definite, so Cholesky factorization can be applied to find the solution v_0 and v_1 [28]. With v_0 and v_1, Δy is found as follows:

$$\Delta y = v_0 - \frac{\hat{a}^T v_0}{1 + \hat{a}^T v_1} v_1 \tag{7.35}$$

In summary, the solution to (7.17)–(7.21) can be found by first computing Δy in Eq. (7.35), then $\Delta\tau$ in Eq. (7.30). After having Δy and $\Delta\tau$, Δx is computed by Eq. (7.27), and finally $\Delta\kappa$ and Δs in Eq. (7.24) and Eq. (7.23) respectively, i.e.,

$$\begin{aligned}
\Delta y &= v_0 - \frac{\hat{a}^T v_0}{1 + \hat{a}^T v_1} v_1 \\
\Delta\tau &= \frac{1}{a_1}(r_{333} - a_2^T \Delta y) \\
\Delta x &= D^2(A^T \Delta y - c\Delta\tau - r_{22}) \\
\Delta\kappa &= \tau^{-1}(r_5 - \kappa\Delta\tau) \\
\Delta s &= \Theta W T \bar{X}^{-1} r_4 - (\Theta W)^2 \Delta x
\end{aligned} \tag{7.36}$$

Following is the second method of computing steps for finding the Newton search direction. Similar ideas may be found in Refs. [27, 28]. Following the way of computing Δs and $\Delta\kappa$ in the first method, we rewrite the formulas here.

$$\Delta s = \Theta W T \bar{X}^{-1} r_4 - (\Theta W)^2 \Delta x \tag{7.37}$$

$$\Delta\kappa = \tau^{-1}(r_5 - \kappa\Delta\tau) \tag{7.38}$$

Substituting Eqs. (7.37) and (7.38) into Eqs. (7.18) and (7.19), we get

$$A^T \Delta y - (\Theta W)^2 \Delta x - c\Delta\tau + \Theta W T \bar{X}^{-1} r_4 = r_2 \tag{7.39}$$

$$b^T \Delta y - c^T \Delta x + \frac{\kappa}{\tau}\Delta\tau - \frac{r_5}{\tau} = r_3 \tag{7.40}$$

From Eq. (7.39), we have

$$\Delta x = D^2 A^T \Delta y + D^2(\Theta W T \bar{X}^{-1} r_4 - c^T \Delta x - r_2) \tag{7.41}$$

where $D := (\Theta W)^{-1}$ is defined as before. Substituting Eq. (7.41) into Eq. (7.17) results in

$$AD^2 A^T \Delta y + AD^2(\Theta W T \bar{X}^{-1} r_4 - c^T \Delta x - r_2) - b\Delta\tau = r_1$$

which gives

$$\begin{aligned} \Delta y &= (AD^2 A^T)^{-1} \left[(r_1 + AD^2 r_2 - AD^2 \Theta W T \bar{X}^{-1} r_4) + (AD^2 c + b)\Delta\tau\right] \\ &= g_2 + h_2 \Delta\tau \end{aligned} \tag{7.42}$$

where

$$\begin{aligned} g_2 &= (AD^2 A^T)^{-1}(r_1 + AD^2 r_2 - AD^2 \Theta W T \bar{X}^{-1} r_4) \\ h_2 &= (AD^2 A^T)^{-1}(AD^2 c + b) \end{aligned}$$

With Δy in Eq. (7.42), Eq. (7.41) is rewritten as

$$\begin{aligned} \Delta x &= D^2(A^T h_2 - c)\Delta\tau + D^2(A^T g_2 + \Theta W T \bar{X}^{-1} r_4 - r_2) \\ &= g_1 + h_1 \Delta\tau \end{aligned} \tag{7.43}$$

where

$$\begin{aligned} g_1 &= D^2(A^T g_2 + \Theta W T \bar{X}^{-1} r_4 - r_2) \\ h_1 &= D^2(A^T h_2 - c) \end{aligned}$$

Replacing Δy and Δx in Eq. (7.40) with Eqs. (7.42) and (7.43), we have

$$b^T(g_2 + h_2\Delta\tau) - c^T(g_1 + h_1\Delta\tau) - \tau^{-1} r_5 + \tau^{-1}\kappa\Delta\tau = r_3$$

So

$$\Delta\tau = \frac{r_3 + \tau^{-1} r_5 + c^T g_1 - b^T g_2}{\tau^{-1}\kappa - c^T h_1 + b^T h_2} \tag{7.44}$$

To make a summary, (g_1, h_1, g_2, h_2) can be found first by the above formulas, which makes the value of $\Delta\tau$ in Eq. (7.44) available. Then Δy and Δx are found by Eq. (7.42) and Eq. (7.43) respectively. Finally Eqs. (7.37), (7.38) are used to compute Δs and $\Delta\kappa$. They are combined together as

$$\begin{aligned}
\Delta\tau &= \frac{r_3 + \tau^{-1} r_5 + c^T g_1 - b^T g_2}{\tau^{-1}\kappa - c^T h_1 + b^T h_2} \\
\Delta y &= g_2 + h_2 \Delta\tau \\
\Delta x &= g_1 + h_1 \Delta\tau \\
\Delta s &= \Theta W T \bar{X}^{-1} r_4 - (\Theta W)^2 \Delta x \\
\Delta\kappa &= \tau^{-1}(r_5 - \kappa\Delta\tau)
\end{aligned} \tag{7.45}$$

The final method to solve (7.17)–(7.21) is to simply combine all variables as one vector and construct one linear system as follows

$$\begin{bmatrix}
A & 0 & 0 & -b & 0 \\
0 & A^T & I & -c & 0 \\
-c^T & b^T & 0 & 0 & -1 \\
\bar{S}T(\Theta W) & 0 & \bar{X}T(\Theta W)^{-1} & 0 & 0 \\
0 & 0 & 0 & \kappa & \tau
\end{bmatrix}
\begin{bmatrix} \Delta x \\ \Delta y \\ \Delta s \\ \Delta\tau \\ \Delta\kappa \end{bmatrix}
=
\begin{bmatrix} r_1 \\ r_2 \\ r_3 \\ r_4 \\ r_5 \end{bmatrix} \tag{7.46}$$

The above linear system can be solved directly to find the newton search direction by using the LU factorization.

Remarks:

1. For the SOCP problem considered above, we assume that there are no free variables. Nevertheless, free variables need to be handled properly so that the above analysis is still effective. The simplest and popular method is to split a free variable $\bar{x}$ into a difference of two nonnegative variables $\bar{x}^+ \geq 0$ and $\bar{x}^- \geq 0$, i.e., $\bar{x} = \bar{x}^+ - \bar{x}^-$ so

that the new variables $\bar{x}^+$ and $\bar{x}^-$ both belong to linear cones. This method may result in numerical instability due to the unboundedness of $\bar{x}^+$ and $\bar{x}^-$. For more details on how to deal with free variables, see Refs. [68, 69].

2. For practical implementation of the primal-dual IPM, more aspects need to be considered. For example, the matrix AD^2A^T in Eq. (7.32) and Eq. (7.42) might be dense even when A is sparse and has only one dense column, which increases the computation cost of computing Δy. Techniques on separating the dense columns in A could improve the efficiency [28, 32, 35]. In addition, presolving are beneficial to reduce the problem size and eliminating features that may lead to numerical difficulties such as linear dependencies in A [35, 70].

3. For the three methods on computing the search direction, the first two methods seek to first solve a normal linear system with coefficient AD^2A^T to find one or more variables, then substitute them back into certain equations in (7.17)–(7.21) to get values for the remaining variables. It is obvious for the third method to have more computational cost when the coefficient of the linear system 7.46 has large size. However, experiences on implementing those methods, as discussed in Section 7.4, tell us that the third method uses fewer iterations to get a solution compared to the first two methods with respect to the same accuracy. The reasons that can be found at this point are that the search direction obtained by the third method can more accurately satisfy the equations in (7.17)–(7.21), while for the first two methods some of the equations in (7.17)–(7.21) are satisfied to only an accuracy of 10^{-8}, rather than high accuracy of about 10^{-15} in the third method for all equations. In other words, the search direction from the first two methods is not as accurate as the one obtained from the third method, which causes the first two methods to use more iterations, though all of them can generate converged solutions. It is mentioned that the third method will encounter difficulty to find the

search direction timely when the problem size is large. Therefore, increasing the accuracy of the search direction from the first two methods to satisfy (7.17)–(7.21) is a big concern for efficient implementation of the primal-dual IPM to large-scale problems.

7.4 Implementation of the Primal-Dual IPM

With the Newton search direction from Section (7.3), it is natural to find the step size for the next point to stay in a neighborhood of the central path. However, in order to improve the efficiency of the algorithm in practice, adaptive Mehrotra's predictor-corrector method [71] is applied, in which a predictor direction is searched and then a corrector direction is computed. The reason for doing so is that γ in (7.17)–(7.21) needs to be determined and the accuracy of the model (7.17)–(7.21) should be improved when possible.

Mehrotra's predictor-corrector method satisfies the above two points. To be specific, after having the predictor direction $(\Delta x^p, \Delta y^p, \Delta s^p, \Delta \tau^p, \Delta \kappa^p)$ with $\gamma = 0$, the step size α^p is found to be the maximum step size when the next point belongs to the feasible set formed by all the constraints. Let the duality gap for the next point and current point be $\bar{\mu}$ and μ respectively. γ is computed by

$$\gamma = (\frac{\bar{\mu}}{\mu})^3 \tag{7.47}$$

where

$$\bar{\mu} = \frac{(x + \alpha^p \Delta x^p)^T (s + \alpha^p \Delta s^p) + (\tau + \alpha^p \Delta \tau^p)(\kappa + \alpha^p \Delta \kappa^p)}{k + 1}$$

We have mentioned that (7.17)–(7.21) is 1st-order approximation to the original system (7.13). With the predictor direction, the quadratic items when linearizing the fourth and fifth equations in (7.13) can be added to improve the accuracy. So the fourth and fifth

equations in (7.22) are replaced with

$$r_4 = \gamma\mu e - \bar{X}\bar{S}e - \Delta\bar{X}\Delta\bar{S}e \tag{7.48}$$

$$r_5 = \gamma\mu - \tau\kappa - \Delta\tau\Delta\kappa \tag{7.49}$$

where

$$\Delta\bar{X}\Delta\bar{S}e \approx \Delta\bar{X}^p\Delta\bar{S}^p e \tag{7.50}$$

$$\Delta\tau\Delta\kappa \approx \Delta\tau^p\Delta\kappa^p \tag{7.51}$$

with

$$\Delta\bar{X}^p := mat(T\Theta W\Delta x^p),\ \Delta\bar{S}^p := mat(T(\Theta W)^{-1}\Delta s^p)$$

For system (7.17)–(7.21) with $(r_1, r_2, r_3, r_4, r_5)$ defined in (7.22), if we choose $\gamma = 0$, then the resulting Newton direction computed by (7.36), (7.45), or (7.46) is found, which is also called pure Newton direction or affine scaling direction. The dynamic choice of γ is based on how much progress there is on the affine scaling direction with respect to the duality gap. The formula in (7.47) is proved to work efficiently based on computation experience, though other choices for computing γ may also work [28].

Next, for system (7.17)–(7.21) with (r_1, r_2, r_3) defined in (7.22) but with (r_4, r_5) defined in Eqs. (7.48) and (7.49), and γ is given by Eq. (7.47), then the computed Newton direction is the corrector direction, denoted as $(\Delta x^c, \Delta y^c, \Delta s^c, \Delta\tau^c, \Delta\kappa^c)$, since there are two corrector items added to the original (r_4, r_5) in (7.22). Based on the corrector direction, the corresponding maximum step size α^c needs to be obtained to make sure the next point

$$(\bar{x}, \bar{y}, \bar{s}, \bar{\tau}, \bar{\kappa}) = (x, y, s, \tau, \kappa) + \alpha^c(\Delta x^c, \Delta y^c, \Delta s^c, \Delta\tau^c, \Delta\kappa^c) \tag{7.52}$$

belongs to a neighborhood of the central path, which is described as

$$(\bar{x}, \bar{y}, \bar{s}, \bar{\tau}, \bar{\kappa}) \in N(\sigma) \tag{7.53}$$

where [27]

$$N(\sigma) = \left\{(x, s, \tau, \kappa) \in int(\bar{K}) | \sqrt{(\bar{x}^i)^T Q^i \bar{x}^i (\bar{s}^i)^T Q^i \bar{s}^i} \geq \sigma\mu, \forall i, \text{and } \tau\kappa \geq \sigma\mu\right\} \quad (7.54)$$

and $\sigma \in [0, 1], \bar{K} = K \times K \times R_+ \times R_+$, i is the idex for each cone. When σ decreases, the size of the neighborhood defined by Eq. (7.54) increases. σ can be typically chosen as 0.001 or other values determined by heuristics.

Following is the procedure for implementing the primal-dual IPM:

1. Choose the starting point for the algorithm:

$$x^{i(0)} = s^{i(0)} = T^i e_1^i, \ y^0 = 0, \ \tau = 1, \ \kappa = 1$$

2. For the current point, set $\gamma = 0$ and solve the linear system (7.17)–(7.21) with $(r_1, r_2, r_3, r_4, r_5)$ defined in (7.22) to get the affine scaling direction. Then the step size α^p is found to be the maximum step that makes sure the next point belongs to the feasible set formed by all constraints. To be prepared for step 3, γ is computed by (7.47) and $r_4, \ r_5$ by (7.48), (7.49).

3. Apply γ from step 2 and solve again the linear system (7.17)–(7.21) with (r_1, r_2, r_3) defined in (7.22) but with (r_4, r_5) defined in Eqs. (7.48) and (7.49) to obtain the corrector direction. The step size α^c is produced based on the idea that the next point belongs to the neighborhood of the central path defined by Eq. (7.53) under maximum step size.

4. Compute the next point as in Eq. (7.52), update the current point with that point $(x, y, s, \tau, \kappa) = (\bar{x}, \bar{y}, \bar{s}, \bar{\tau}, \bar{\kappa})$ and check whether the following conditions are all

satisfied [35]:

$$\begin{aligned} \frac{\| Ax - b\tau \|_\infty}{1+ \| b \|} &\leq \epsilon \\ \frac{\| A^T y + s - c\tau \|_\infty}{1+ \| c \|} &\leq \epsilon \\ \frac{\| b^T y - c^T x - \kappa \|_\infty}{1+ \| c^T x \|} &\leq \epsilon \\ \frac{x^T s + \tau\kappa}{k+1} &\leq \epsilon \end{aligned} \tag{7.55}$$

where ϵ is a prescribed number and very small, usually 10^{-8}. Meanwhile, check whether the maximum iteration limit N_{max}, such as 50 for instance, is reached. If neither of them is satisfied, go to step 2. Otherwise, go to step 5.

5. The following conclusion is given based on the current point (x, y, s, τ, κ):

   If $\tau > 0$, $(\frac{x}{\tau}, \frac{y}{\tau}, \frac{s}{\tau})$ is the optimal solution for (7.3) or the primal-dual problem. Otherwise, if $\tau = 0$ and $\kappa > 0$, the primal problem is infeasible when $b^T y > 0$, and the dual problem infeasible when $c^T x < 0$.

CHAPTER 8. CONCLUSIONS

The majority of the optimal control problems from aerospace applications are nonlinear and non-convex. This dissertation proposes to apply various techniques to transform the original problems into appropriate formulations so that second-order cone programming (SOCP), which belongs to convex optimization, can be employed to solve the problems. For rendezvous and proximity operations (RPO), a lossless relaxation technique is used to obtain a relaxed problem which is proven to have the same solutions with the original problem. Then a novel successive approximation method is applied to deal with the nonlinearity inherent in the inverse-square gravity in the system dynamics. Consequently, the highly constrained RPO problem (non-convex) is to solve a sequence of SOCP problems. The convergence property of the successive solutions is discussed in this dissertation and numerical results demonstrate the effectiveness of the methodology, which, meanwhile, is also capable of incorporating perturbations such as Earth harmonics J_2 and atmospheric drag. For problems with concave inequality constraints, specifically collision avoidance constraints, the successive linearization method is proposed to linearize the concave constraints to get a sequence of SOCP subproblems and leads to some strong theoretical results which include guaranteed satisfaction of the original constraints through the linearized ones, existence of the solution sequence and the equivalence of a local optimal solution of the original non-convex problem to the convergent solution of the sequence of subproblems. Furthermore, when a problem has nonlinear terminal constraints, the method used is to linearize the nonlinear equality constraints and also add second-order corrections which are predicted by solving the problem with the linearized

equality constraints. The corrections are found to improve the robustness of convergence in practical problems. For problems with any non-convexity feature above, various application problems are provided to demonstrate the effectiveness of the methodology proposed in this dissertation.

APPENDIX . PROOF OF LEMMAS

Proof of Lemma 3.2.2: We shall prove this lemma by showing that if $\boldsymbol{p}_V \neq 0$ *a.e.*, $\|\boldsymbol{T}^*\| = \eta^*$ must hold. First assume that this interval where $\|\boldsymbol{T}^*\| < \eta^*$ does not overlap with the finite interval(s) where the constraint (3.40) is active (if it happens at all). If $\boldsymbol{p}_V \neq 0$ *a.e.* in this interval, the pointwise maximization condition (3.30) applies. Following the same arguments based on the existence of a maximizing $\boldsymbol{T}^*$ and the KKT conditions as used in Lemma 3.2.1 shows for any fixed $\eta \geq 0$

$$\|\boldsymbol{T}^*\| = \eta \;\longrightarrow \|\boldsymbol{T}^*\| = \eta^* \tag{.1}$$

that is, $\|\boldsymbol{T}^*\| < \eta^*$ cannot be true in this interval.

Now, if the interval where $\boldsymbol{p}_V \neq 0$ *a.e.* overlaps with a finite interval where the constraint (3.40) is active, the pointwise maximization condition (3.30) in this interval will be modified as (see the proof of Theorem 22 in Ref. [41] for detail.[1])

$$\max_{(\boldsymbol{T},\eta)\in\Omega(\boldsymbol{x})} H[\boldsymbol{y}(t), \boldsymbol{p}(t), \boldsymbol{T}, \eta] \tag{.2}$$

where H is the same as in Eq. (3.26), and the set $\Omega(\boldsymbol{x})$ is defined as follows: for given $\boldsymbol{x} = (\boldsymbol{r}^T \; \boldsymbol{V}^T)^T$ where $h(\boldsymbol{r}, t) = 0$

$$\begin{aligned} \Omega(\boldsymbol{x}) \;\; = \;\; & \big\{(\boldsymbol{T}, \eta) \mid \; \|\boldsymbol{T}\| \leq \eta, \boldsymbol{\gamma}^T(\boldsymbol{r}, t)\boldsymbol{T} + \phi(\boldsymbol{r}, \boldsymbol{V}, t) = 0, \\ & \mathbf{1}_n^T \boldsymbol{T} \leq \eta \cos\theta, \; 0 \leq \eta \leq T_{max}\big\} \end{aligned} \tag{.3}$$

[1]Note that Theorem 22 in Ref. [41] applies to first-order state inequality constraint $g(\boldsymbol{x}) \leq 0$. But, in the notation of Ref. [41], what is fundamental in the proof is the first-order time derivative of the constraint $p(\boldsymbol{x}, \boldsymbol{u}) = \dot{g}(\boldsymbol{x})$. For a second-order constraint, the proof would remain essentially the same if $p(\boldsymbol{x}, \boldsymbol{u})$ is replaced by the second-order time derivative of the constraint $q(\boldsymbol{x}, \boldsymbol{u}, t)$, as in our case.

where the second constraint $\boldsymbol{\gamma}^T(\boldsymbol{r},t)\boldsymbol{T}+\phi(\boldsymbol{r},\boldsymbol{V},t)=0$ is from Eq. (3.41). For each fixed $\eta>0$ the domain from which $\boldsymbol{T}$ is selected to maximize H is the set $\omega(\boldsymbol{x})$

$$\omega(\boldsymbol{x})=\{\boldsymbol{T}\mid\ \|\boldsymbol{T}\|\leq\eta,\boldsymbol{\gamma}^T(\boldsymbol{r},t)\boldsymbol{T}+\phi(\boldsymbol{r},\boldsymbol{V},t)=0,\mathbf{1}_n^T\boldsymbol{T}\leq\eta\cos\theta,\} \tag{.4}$$

The set $\omega(\boldsymbol{x})$ is the intersection of a sphere, a hyperplane, and the half-space defined by another hyperplane. So $\omega(\boldsymbol{x})$ itself is convex and bounded. For $\boldsymbol{p}_V\neq 0$ the Hamiltonian is a non-constant convex (linear) function of $\boldsymbol{T}$. Hence a maximizing $\boldsymbol{T}^*$ is guaranteed to exist on the boundary of $\omega(\boldsymbol{x})$ [42], and it satisfies the KKT conditions similar to Eq. (3.33) (plus a term $\lambda_3\boldsymbol{\gamma}$ associated with $\boldsymbol{\gamma}^T(\boldsymbol{r},t)\boldsymbol{T}+\phi(\boldsymbol{r},\boldsymbol{V},t)=0$ this time) and Eq. (3.34). The same arguments as used the proof of Lemma 1 will show that $\|\boldsymbol{T}^*\|=\eta$, and $\|\boldsymbol{T}^*\|=\eta^*$ when η takes its optimal value. □

Proof of Lemma 3.2.3: Because the jump conditions such as those in Eqs. (3.42) and (3.43) generally involve $\boldsymbol{p}_V$, a finite interval where $\boldsymbol{p}_V=0$ can only be in a subinterval separated by two adjacent jump conditions. First assume that such an interval does not overlap with $[t_{in},\ t_{out}]$ in which $h(\boldsymbol{r},t)=0$ (cf. Eq. (3.40)). The same arguments as in the proof of Lemma 1 will show $\boldsymbol{p}_r=\boldsymbol{p}_V=0$ in this interval, resulting in the condition for the Hamiltonian defined in Eq. (3.26)

$$H=-\left(\frac{p_m}{v_{ex}}+p_0\right)\eta \tag{.5}$$

If $(p_m/v_{ex}+p_0)>0$, the optimality condition (3.30) with respect to η in the set $\mathscr{U}_\eta$ defined as

$$\mathscr{U}_\eta=\{\eta\mid\mathbf{1}_n^T(t)\boldsymbol{T}\leq\eta\cos\theta,\ 0\leq\eta\leq T_{max}\} \tag{.6}$$

should take the lower bound of this set. As argued in the proof of Lemma 1, the lower bound of the set $\mathscr{U}_\eta$ is $\eta=0$ under Assumption 1, thus $H=0$; if $(p_m/v_{ex}+p_0)=0$, still $H=0$ regardless of what value $\eta^*\in[0,T_{max}]$ is. Since the system equations (3.15)–(3.17) are autonomous, the performance index (3.14) is not an explicit function of time, the problem has a fixed final time t_f, and the continuity of the Hamiltonian is

not affected by the jump conditions (3.42) and (3.43), it follows that the optimal value of H is a constant throughout $[0, t_f]$ [41]. But both the above two possibilities imply that $H = 0$, and this is irrespective of any value of t_f. Given that the $H(t_f)$ represents the influence of the variation of t_f on the performance index [43], such an invariance of the cost with respect to any t_f is not possible for the problem at hand. Therefore the condition that $(p_m/v_{ex} + p_0) \geq 0$ can be ruled out, and the only remaining possibility is that $(p_m/v_{ex} + p_0) < 0$. From Eq. (3.29) it is clear that p_m is constant when $\boldsymbol{p}_V = 0$, so is $(p_m/v_{ex} + p_0)$. The maximization of H in (.5) with respect to η over the set $\mathscr{U}_\eta$ in Eq. (.6) calls for the optimal η^* to take the upper bound of $\mathscr{U}_\eta$. But it is pointed out in the proof of Lemma 1 that $\mathscr{U}_\eta = \{\eta \mid 0 \leq \eta \leq T_{max}\}$ (cf. Eq. (3.38)). Hence $\eta^* = T_{max}$.

If the constraint (3.40) is not active anywhere, or active only at some isolated points ($t_{in} = t_{out}$), the above discussion already covers the case. Next consider the case when the interval $[t_{in},\ t_{out}]$ has finite length ($t_{out} > t_{in}$), and the interval in which $\boldsymbol{p}_V = 0$ is contained in $[t_{in},\ t_{out}]$. In the interval $[t_{in},\ t_{out}]$ the costate equation for $\boldsymbol{p}_V$ becomes [41]

$$\dot{\boldsymbol{p}}_r = \frac{1}{\|\boldsymbol{r}\|^3}\boldsymbol{p}_V - \frac{(\boldsymbol{p}_V^T\boldsymbol{r})}{\|\boldsymbol{r}\|^5}\boldsymbol{r} + D(\boldsymbol{x}, \boldsymbol{T}, t)\boldsymbol{p}_r + E(\boldsymbol{x}, \boldsymbol{T}, t)\boldsymbol{p}_V \tag{.7}$$

$$\dot{\boldsymbol{p}}_V = -\boldsymbol{p}_r + F(\boldsymbol{x}, \boldsymbol{T}, t)\boldsymbol{p}_r + G(\boldsymbol{x}, \boldsymbol{T}, t)\boldsymbol{p}_V \tag{.8}$$

where D–G are 3×3 matrices from a dyad formed by $\partial q(\boldsymbol{x}, \boldsymbol{T}, t)/\partial \boldsymbol{x}$ and another time-dependent vector in R^6. See the proof of Theorem 22 in Ref. [41] for detail.[2] When $\boldsymbol{p}_V = 0$ in any finite subinterval in $[t_{in},\ t_{out}]$, $\boldsymbol{p}_r$ will have to vanish simultaneously in general, and consequently $\boldsymbol{p}_V = \boldsymbol{p}_r = 0$ throughout $[t_{in},\ t_{out}]$. Hence the Hamiltonian reduces to (.5) again. The optimal η will be determined from condition (.2), which for η is over the same set $\mathscr{U}_\eta$ in Eq. (.6). Therefore the same arguments employed in the preceding paragraph will again lead to $\eta^* = T_{max}$. □

[2] The footnote in the proof of Lemma 3.2.2 applies here as well.

Proof of Lemma 5.3.2: The dual problem to the SOCP problem PP($\boldsymbol{y}^{[k]}$) is first derived. Define the Lagrangian of PP($\boldsymbol{y}^{[k]}$) as [22]

$$\begin{aligned} L(\boldsymbol{y},\boldsymbol{\iota},\boldsymbol{v},\boldsymbol{s}) &= \boldsymbol{c}^T\boldsymbol{y} + \boldsymbol{\iota}^T(H\boldsymbol{y}-\boldsymbol{p}) + \sum_{i=1}^{l} v_i[g_i(\boldsymbol{y}^{[k]}) + \nabla g_i(y^{[k]})^T(\boldsymbol{y}-\boldsymbol{y}^{[k]})] - \boldsymbol{s}^T(A\boldsymbol{y}-\boldsymbol{b}) \\ &= \left[H^T\boldsymbol{\iota} + \boldsymbol{c} + \sum_{i=1}^{l} v_i\nabla g_i(\boldsymbol{y}^{[k]}) - A^T\boldsymbol{s}\right]^T \boldsymbol{y} - \iota^T\boldsymbol{p} + \boldsymbol{b}^T\boldsymbol{s} \\ &+ \sum_{i=1}^{l} v_i\left[g_i(\boldsymbol{y}^{[k]}) - \nabla g_i(\boldsymbol{y}^{[k]})^T\boldsymbol{y}^{[k]}\right] \end{aligned} \tag{.9}$$

where $\boldsymbol{\iota}$, $\boldsymbol{v}$ and $\boldsymbol{s}$ are the associated Lagrange multipliers with $\boldsymbol{\iota} \geq 0$, $\boldsymbol{v} = [v_1, \ldots, v_l]^T \geq 0$ and $\boldsymbol{s} \in \bar{K}^*$ with $\bar{K}^*$ being the dual cone to $\bar{K}$. The dual problem to PP($\boldsymbol{y}^{[k]}$) is given by [22]

$$\max_{\boldsymbol{\iota}\geq 0,\, \boldsymbol{v}\geq 0,\, \boldsymbol{s}\in\bar{K}^*} \left[\inf_{\boldsymbol{y}\in R^n} \; L(\boldsymbol{y},\boldsymbol{\iota},\boldsymbol{v},\boldsymbol{s})\right] \tag{.10}$$

or equivalently[3]

$$\text{DD}(\boldsymbol{y}^{[k]}): \quad \text{maximize} \quad -\boldsymbol{\iota}^T\boldsymbol{p} + \sum_{i=1}^{l} v_i[g_i(\boldsymbol{y}^{[k]}) - \nabla g_i(\boldsymbol{y}^{[k]})^T\boldsymbol{y}^{[k]}] + \boldsymbol{b}^T\boldsymbol{s} \tag{.11}$$

$$\text{subject to} \quad H^T\boldsymbol{\iota} + \boldsymbol{c} + \sum_{i=1}^{l} v_i\nabla g_i(\boldsymbol{y}^{[k]}) = A^T\boldsymbol{s} \tag{.12}$$

$$\boldsymbol{\iota} \geq 0, \; \boldsymbol{v} \geq 0 \tag{.13}$$

$$\boldsymbol{s} \in \bar{K}^* \tag{.14}$$

The Weak Duality Theorem [22] states that the optimal cost of DD($\boldsymbol{y}^{[k]}$) is a lower bound to that of the primal problem PP($\boldsymbol{y}^{[k]}$), and the difference between them is called the optimal duality gap. PP($\boldsymbol{y}^{[k]}$) is a second-order cone problem and thus convex, Moreover, since it is strictly feasible, the Slater's condition [22] holds. Hence the strong duality holds, meaning that the optimal duality gap is zero. Denote the optimal values of the objective functions of the primal and dual problems by P^* and D^* respectively. Then

[3]The formulation of the dual problem DD($\boldsymbol{y}^{[k]}$) presented here may also be derived by following the approach in Section 2.3 of Ref. [33].

for $\boldsymbol{y}^* = \boldsymbol{y}^{[k]}$, zero duality gap implies

$$\begin{aligned} 0 = P^* - D^* &= \boldsymbol{c}^T\boldsymbol{y}^* + \boldsymbol{\iota}^{*T}\boldsymbol{p} - \sum_{i=1}^{l} v_i^*[g_i(\boldsymbol{y}^{[k]}) - \nabla g_i(\boldsymbol{y}^{[k]})^T\boldsymbol{y}^{[k]}] - \boldsymbol{b}^T\boldsymbol{s}^* \\ &\geq \boldsymbol{c}^T\boldsymbol{y}^* + \boldsymbol{\iota}^{*T}H\boldsymbol{y}^* + \sum_{i=1}^{l} v_i^*\nabla g_i(\boldsymbol{y}^{[k]})^T\boldsymbol{y}^* - \boldsymbol{b}^T\boldsymbol{s}^* \\ &= [H^T\boldsymbol{\iota}^* + \boldsymbol{c} + \sum_{i=1}^{l} v_i^*\nabla g_i(\boldsymbol{y}^{[k]})]^T\boldsymbol{y}^{[k]} - \boldsymbol{b}^T\boldsymbol{s}^* \\ &= \boldsymbol{s}^{*T}A\boldsymbol{y}^{[k]} - \boldsymbol{b}^T\boldsymbol{s}^* = \boldsymbol{s}^{*T}(A\boldsymbol{y}^{[k]} - \boldsymbol{b}) \end{aligned} \tag{.15}$$

where the asterisked multipliers are the corresponding ones in the optimal solution of DD($\boldsymbol{y}^{[k]}$). The inequality sign in above equation is a result of using $\boldsymbol{\iota}^{*T}\boldsymbol{p} \geq \boldsymbol{\iota}^{*T}H\boldsymbol{y}^*$ and $g_i(\boldsymbol{y}^{[k]}) + \nabla g_i(\boldsymbol{y}^{[k]})^T(\boldsymbol{y}^* - \boldsymbol{y}^{[k]}) \leq 0$, and the last second to the last equality sign is a consequence of Eq. (.12). Equation (.15) gives $\boldsymbol{s}^{*T}(A\boldsymbol{y}^{[k]} - \boldsymbol{b}) \leq 0$. On the other hand, by the definition of dual cone [22], $\boldsymbol{s}^* \in \bar{K}^*$ means that $\boldsymbol{s}^{*T}(A\boldsymbol{y}^{[k]} - \boldsymbol{b}) \geq 0$. Therefore, the only possibility is

$$\boldsymbol{s}^{*T}(A\boldsymbol{y}^{[k]} - \boldsymbol{b}) = 0 \tag{.16}$$

In addition, the following equation holds

$$\begin{aligned} &\boldsymbol{\iota}^{*T}(H\boldsymbol{y}^* - \boldsymbol{p}) + \sum_{i=1}^{l} v_i^*[g_i(\boldsymbol{y}^{[k]}) + \nabla g_i(\boldsymbol{y}^{[k]})^T(\boldsymbol{y}^* - \boldsymbol{y}^{[k]})] - \boldsymbol{s}^{*T}(A\boldsymbol{y}^* - \boldsymbol{b}) \\ =&[H^T\boldsymbol{\iota}^* + \sum_{i=1}^{l} v_i^*\nabla g_i(\boldsymbol{y}^{[k]})]^T\boldsymbol{y}^* - \boldsymbol{\iota}^{*T}\boldsymbol{p} + \sum_{i=1}^{l} v_i^*[g_i(\boldsymbol{y}^{[k]}) - \nabla g_i(\boldsymbol{y}^{[k]})\boldsymbol{y}^{[k]}] + \boldsymbol{b}^T\boldsymbol{s}^* - \boldsymbol{s}^{*T}A\boldsymbol{y}^* \\ =&[H^T\boldsymbol{\iota}^* + \sum_{i=1}^{l} v_i^*\nabla g_i(\boldsymbol{y}^{[k]})]^T\boldsymbol{y}^* + \boldsymbol{c}^T\boldsymbol{y}^* - \boldsymbol{s}^{*T}A\boldsymbol{y}^* = \boldsymbol{s}^{*T}A\boldsymbol{y}^* - \boldsymbol{s}^{*T}A\boldsymbol{y}^* = 0 \end{aligned} \tag{.17}$$

where in above steps, the following two results from the first part of Eq. (.15) and Eq. (.12) are used

$$\boldsymbol{c}^T\boldsymbol{y}^* + \boldsymbol{\iota}^{*T}\boldsymbol{p} - \sum_{i=1}^{l} v_i^*[g_i(\boldsymbol{y}^{[k]}) - \nabla g_i(\boldsymbol{y}^{[k]})^T\boldsymbol{y}^{[k]}] - \boldsymbol{b}^T\boldsymbol{s}^* = 0$$

$$H^T\boldsymbol{\iota}^* + \boldsymbol{c} + \sum_{i=1}^{l} v_i\nabla g_i(\boldsymbol{y}^{[k]}) - \boldsymbol{s}^{*T}A = 0$$

Let C be the feasibility set of Problem PP($\boldsymbol{y}^{[k]}$)

$$C = \left\{ \boldsymbol{y} \in R^n \mid H\boldsymbol{y} \leq \boldsymbol{p},\ g_i(\boldsymbol{y}^{[k]}) + \nabla g_i(\boldsymbol{y}^{[k]})^T(\boldsymbol{y} - \boldsymbol{y}^{[k]}) \leq 0,\ A\boldsymbol{y} - \boldsymbol{b} \geq_K 0,\ \|\boldsymbol{y} - \boldsymbol{y}^{[k]}\| \leq \rho \right\} \tag{.18}$$

The constraints in Eqs. (.13) and (.14) for Problem DD($\boldsymbol{y}^{[k]}$) plus $\boldsymbol{y}^* \in C$ mean that $\boldsymbol{\iota}^{*T}(H\boldsymbol{y}^* - \boldsymbol{p}) \leq 0$, $v_i^*[g_i(\boldsymbol{y}^{[k]}) - \nabla g_i(\boldsymbol{y}^{[k]})^T(\boldsymbol{y}^* - \boldsymbol{y}^{[k]})] \leq 0$, and $-\boldsymbol{s}^{*T}(A\boldsymbol{y}^* - \boldsymbol{b}) \leq 0$. Hence Eq. (.17) implies that each term on the left-most hand side of the equation must be zero, in particular,

$$\boldsymbol{\iota}^{*T}(H\boldsymbol{y}^* - \boldsymbol{p}) = 0 \tag{.19}$$

$$v_i^*[g_i(\boldsymbol{y}^{[k]}) - \nabla g_i(\boldsymbol{y}^{[k]})^T(\boldsymbol{y}^* - \boldsymbol{y}^{[k]})] = 0 \tag{.20}$$

When $\boldsymbol{y}^* = \boldsymbol{y}^{[k]}$, the above two equations become

$$\boldsymbol{\iota}^{*T}(H\boldsymbol{y}^{[k]} - \boldsymbol{p}) = 0 \tag{.21}$$

$$v_i^* g_i(\boldsymbol{y}^{[k]}) = 0 \tag{.22}$$

Finally, when $\boldsymbol{y}^* = \boldsymbol{y}^{[k]}$, the trust region constraint in (5.22) is an inactive inequality constraint and can be ignored, which implies that all the cone constraints in PP($\boldsymbol{y}^{[k]}$) are identical to those in P^1, or $\bar{K} = K$.

Combine all the constraints from both PP($\boldsymbol{y}^{[k]}$) and DD($\boldsymbol{y}^{[k]}$), Eqs. (.16), (.21), and (.22), $\boldsymbol{y}^* = \boldsymbol{y}^{[k]} \in C$, and condition $\bar{K} = K$ to get

$$H^T\boldsymbol{\iota}^* + \sum_{i=1}^{l} v_i^* \nabla g_i(\boldsymbol{y}^{[k]}) + \boldsymbol{c} = A^T\boldsymbol{s}^* \tag{.23}$$

$$\iota^{*T}(H\boldsymbol{y}^{[k]} - \boldsymbol{p}) = 0 \tag{.24}$$

$$v_i^* g_i(\boldsymbol{y}^{[k]}) = 0,\ i = 1, \ldots, l \tag{.25}$$

$$\boldsymbol{s}^{*T}(A\boldsymbol{y}^{[k]} - \boldsymbol{b}) = 0 \tag{.26}$$

$$H\boldsymbol{y}^{[k]} \leq p \tag{.27}$$

$$g_i(\boldsymbol{y}^{[k]}) \leq 0,\ i = 1, ..., l \tag{.28}$$

$$\boldsymbol{\iota}^* \geq 0,\ \boldsymbol{v}^* \geq 0,\ A\boldsymbol{y}^{[k]} - \boldsymbol{b} \geq_K 0,\ \boldsymbol{s}^* \in K^* \tag{.29}$$

The above equations suggest that the Lagrange multipliers ($\boldsymbol{\iota}^*$, $\boldsymbol{v}^*$, $\boldsymbol{s}^*$) and $\boldsymbol{y}^* = \boldsymbol{y}^{[k]}$ satisfy the KKT conditions for the original problem P^1. Equations (.24)–(.25) are the conditions for complementary slackness and Eqs. (.27)–(.29) conditions for feasibility [22]. So $\boldsymbol{y}^* = \boldsymbol{y}^{[k]}$ is a KKT solution for Problem P^1. □

BIBLIOGRAPHY

[1] Woffinden, D. C. and Geller, D. K., "Navigating the Road to Autonomous Orbital Rendezvous," *Journal of Spacecraft and Rockets*, Vol. 44, No. 4, 2007, pp. 898–909.

[2] Goodman, J. L., "History of Space Shuttle Rendezvous and Proximity Operations," *Journal of Spacecraft and Rockets*, Vol. 43, No. 5, 2006, pp. 944–959.

[3] Goodman, J. L. and Brazzel, J. P., "Rendezvous Integration Complexity of NASA Human Flight Vehicles," AAS Paper 09-065, 32nd Annual AAS Guidance and Control Conference, Breckenridge, CO, January 2009.

[4] Goodman, J. L., "History of Space Shuttle Rendezvous," Revision 3, JSC-63400, Flight Dynamics Division, Mission Operations Directorate, NASA Johnson Space Center, Houston, TX, October 2011.

[5] Clohessy, W. H. and Wiltshire, R. S., "Terminal Guidance for Satellite Rendezvous," *Journal of the Aerospace Sciences*, Vol. 27, No. 9, 1960, pp. 653–674.

[6] Carter, T. E. and Humi, M., "Fuel-Optimal Rendezvous Near a Point in General Keplerian Orbit," *Journal of Guidance, Control, and Dynamics*, Vol. 10, No. 6, 1987, pp. 567–573.

[7] Carter, T. E. and Humi, M., "State-Transition Matrices for Terminal Rendezvous Studies: Brief Survey and New Example," *Journal of Guidance, Control, and Dynamics*, Vol. 21, No. 1, 1998, pp. 148–155.

[8] Yamanaka, K. and Andersen, F., "New State Transition Matrix for Relative Motion on an Arbitrary Elliptical Orbit," *Journal of Guidance, Control and Dynamics*, Vol. 25, No. 6, 2002, pp. 1073–1080.

[9] Lu, P. and Liu, X., "Autonomous Trajectory Planning for Rendezvous and Proximity Operations by Conic Optimization," *Journal of Guidance, Control, and Dynamics*, 2013, in press.

[10] D'Souza, C., Hanak, F. C., Spehar, P., Clark, F. D., and Jackson, M., "Orion Rendezvous, Proximity Operations, and Docking Design and Analysis," AIAA Paper 2007-6683, August 2007.

[11] Chobotov, V. A., *Orbital Mechanics*, chap. 9, AIAA, Reston, VA, 3rd ed., 2002.

[12] Vallado, D., *Fundamentals of Astrodynamics and Applications*, chap. 8, Microcosm Press, El Segundo, CA, 2nd ed., 2004, Appendix B.

[13] Schweighart, S. A. and Sedwick, R. J., "High-Fidelity Linearized J_2 Model for Satellite Formation Flight," *Journal of Guidance, Control, and Dynamics*, Vol. 25, No. 1, 2002, pp. 60–66.

[14] Bevilacqua, R. and Romano, M., "Rendezvous Maneuvers of Multiple Spacecraft Using Differential Drag Under J_2 Perturbation," *Journal of Guidance, Control, and Dynamics*, Vol. 31, No. 6, 2008, pp. 15951607.

[15] Richards, A., Schouwenaars, T., How, P., and Feron, E., "Spacecraft Trajectory Planning with Avoidance Constraints Using Mixed-Integer Linear Programming," *Journal of Guidance, Control, and Dynamics*, Vol. 25, No. 4, 2002.

[16] Mueller, J. B. and Larsson, R., "Collision Avoidance Maneuver Planning with Robust Optimization," 7th International ESA Conference on Guidance, Navigation and Control Systems, June 2008.

[17] Mueller, J. B., Griesemer, P. R., and Thomas, S., "Collision Avoidance Maneuver Planning with Robust Optimization," AIAA Paper 2010-3525, April 2010.

[18] Boggs, P. and Tolle, J., "Sequential Quadratic Programming," *Acta Numerica*, Vol. 4, 1995, pp. 1–51.

[19] Nocedal, J. and Wright, S. J., *Numerical Optimization*, chap. 11 and 18, Springer-Verlag, New York, NY, 2nd ed., 2006.

[20] Acikmese, B. and Blackmore, L., "Lossless Convexification for a Class of Optimal Control Problems with Nonconvex Control Constraints," *Automatica*, Vol. 47, No. 2, 2011, pp. 341–347.

[21] Acikmese, B., Carson, J. M., and Blackmore, L., "Lossless Convexification of Nonconvex Control Bound and Pointing Constraints of the Soft Landing Optimal Control Problem," accepted for publication in *IEEE Transactions on Control Systems Technology*, 2013.

[22] Boyd, S. and Vandenberghe, L., *Convex Optimization*, chap. 5, Cambridge University Press, New York, 2004.

[23] Alizadeh, F. and Goldfarb, D., "Second-Order Cone Programming," *Mathematical Programming*, Vol. 95, No. 1, 2003, pp. 3–51.

[24] Lobo, M. S., Vandenburghe, L., Boyd, S., and Lebret, H., "Applications of Second-Order Cone Programming," *Linear Algebra and its Applications*, Vol. 284, 1998, pp. 193–228.

[25] Acikmese, B. and Ploen, S. R., "Convex Programming Approach to Powered Descent Guidance for Mars Landing," *Journal of Guidance, Control and Dynamics*, Vol. 30, No. 5, 2007, pp. 1353–1366.

[26] Blackmore, L., Acikmese, B., and Scharf, D. P., "Minimum Landing Error Powered Descent Guidance for Mars Landing Using Convex Optimization," *Journal of Guidance, Control and Dynamics*, Vol. 33, No. 4, 2010, pp. 1161–1171.

[27] Kuo, Y.-J. and Mittelmann, H. D., "Interior Point Methods for Second-Order Cone Programming and OR Applications," *Computational Optimization and Applications*, Vol. 28, 2004, pp. 255–285.

[28] Andersen, E. D., Roos, C., and Terlaky, T., "On Implementing a Primal-Dual Interior-Point Method for Conic Quadratic Optimization," *Mathematical Programming*, Vol. 95, No. 2, 2003, pp. 249–277.

[29] Toh, K. C., Todd, M. J., and Tütüncü, R. H., "SDPT3A MATLAB Software Package for Semidefinite Programming," *Optimization Methods and Software*, Vol. 11-12, 1999, pp. 545–581.

[30] Sturm, J. F., "Using SeDuMi 1.02, A MATLAB Toolbox for Optimization over Symmetric Cones," *Optimization Methods and Software*, Vol. 11-12, 1999, pp. 625–653.

[31] Vandenberghe, L. and Boyd, S., "Semidefinite Programming," *SIAM Review*, Vol. 38, No. 1, 1996, pp. 49–95.

[32] Wang, B., *Implementation of Interior Point Methods*, Master's thesis, McMaster University, Hamilton, Ontario, 2003.

[33] Ben-Tal, A. and Nemirovski, A., *Lectures on Modern Convex Optimization: Analysis, Algorithms, and Engineering Applications*, chap. 2-3, Society for Industrial and Applied Mathematics, Philadelphia, PA, 2001.

[34] Nesterov, Y. and Nemirovsky, A., *Interior-point Polynomial Methods in Convex Programming*, Society for Industrial and Applied Mathematics, Philadelphia, PA, 1994.

[35] Wright, S. J., *Primal-Dual Interior-Point Methods*, Society for Industrial and Applied Mathematics, Philadelphia, PA, 1997.

[36] Bate, R. R., Mueller, D., and White, J. E., *Fundamentals of Astrodynamics*, chap. 2, General Publishing Company, Toronto, Ontario, 1971.

[37] Wie, B., *Space Vehicle Dynamics and Control*, chap. 5, AIAA, Reston, VA, 2nd ed., 2008.

[38] Fehse, W., *Automated Rendezvous and Docking of Spacecraft*, Cambridge University Press, 2003.

[39] Goodman, J. L., "Challenges of Orion Rendezvous Development," AIAA Paper 2007-6682, August 2007.

[40] Jezewski, D. J., Brazzel, J. P., Prust, E. E., Brown, B. G., Mulder, T. A., and Wissinger, D. B., "A Survey of Rendezvous Trajectory Planning," Paper AAS 91-505, AAS/AIAA Astrodynamics Conference, Durango, CO, August 19-22 1991.

[41] Pontryagin, L. S., Boltyanskii, V. G., Gramkreledze, Q. V., and Mishchenko, E. F., *The Mathematical Theory of Optimal Processes*, chap. 1, 2 and 6, Intersciences, New York, 1962.

[42] Berkovitz, L. D., *Convexity and Optimization in R^n*, chap. IV, John Wiley, New York, 2002.

[43] Bryson, A. E. and Ho, Y. C., *Applied Optimal Control*, chap. 3, Hemisphere, Washington, D. C., 1975.

[44] Jezewski, D. J., "An Optimal, Analytic Solution to the Linear-Gravity, Constant-Thrust Trajectory Problem," *Journal of Spacecraft and Rockets*, Vol. 8, No. 7, 1971, pp. 793–796.

[45] Carson, J. M. and Acikmese, B., "A Model Predictive Control Technique with Guaranteed Resolvability and Required ThrusterSilent Times for Small-Body Proximity Operations," AIAA Paper 2006-6780, August 2006.

[46] Lu, P., Griffin, B., Dukeman, G., and Chavez, F., "Rapid Optimal Multi-Burn Ascent Planning and Guidance," *Journal of Guidance, Control, and Dynamics*, Vol. 31, No. 6, 2008, pp. 1656–1664.

[47] Banks, S. P. and Dinesh, K., "Approximate Optimal Control and Stability of Nonlinear Finite- and Infinite-Dimensional Systems," *Annals of Operations Research*, Vol. 98, 2000, pp. 19–44.

[48] Ström, T., "Logarithmic Norms," *SIAM Journal of Numerical Analysis*, Vol. 12, No. 5, 1975, pp. 741–753.

[49] Hofer, E. and Tibken, B., "An Iterative Method for the Finite-Time Bilinear Quadratic Control Problem," *Journal of Optimization Theory and Applications*, Vol. 57, No. 3, 1988, pp. 411–427.

[50] Aganovic, Z. and Gajic, Z., "The Successive Approximation Procedure for Finite-Time Optimal Control of Bilinear Systems," *IEEE Transactions on Automatic Control*, Vol. 39, No. 9, 1994, pp. 1932–1935.

[51] Lee, E. B. and Markus, L., *Foundations of Optimal Control Theory*, chap. 4, John Wiley, New York, 1967.

[52] Lu, P. and Liu, X., "Robust Trajectory Optimization for Highly Constrained Rendezvous and Proximity Operations," submitted to the Guidance, Navigation, and Control Conference, 2013, Boston, MA.

[53] Löfberg, J., "YALMIP: A Toolbox for Modeling and Optimization in MATLAB," In Proceedings of the CACSD Conference, Taipei, Taiwan, 2004.

[54] Stewart, R. A. and Griffith, R. E., "A Nonlinear Programming Technique for the Optimization of Continuous Processing Systems," *Management Science*, Vol. 7, No. 4, 1961, pp. 379–392.

[55] Palacios-Gomez, F., Lasdon, L., and Engquist, M., "Nonlinear Optimization by Successive Linear Programming," *Management Science*, Vol. 28, No. 10, 1982, pp. 1106–1120.

[56] Lu, P. and Liu, X., "Solving Non-Convex Optimal Control Problems by Convex Optimization," submitted to the Journal of Guidance, Control and Dynamics, 2013.

[57] Jongen, H. T., Meer, K., and Triesch, E., *Optimization Theory*, Kluwer Academic Publishers, New York, 2004, p. 5.

[58] Zangwill, W. I., *Nonlinear Programming: A Unified Approach*, chap. 4, Prentice-Hall, Englewood Cliffs, NJ, 1969.

[59] Fehse, W., *Automated Rendezvous and Docking of Spacecraft*, chap. 5, Cambridge University Press, Cambridge, UK, 2nd ed., 2003.

[60] Lu, P., "Use of Approximate Gradients in Trajectory Optimization," *Journal of Guidance, Control, and Dynamics*, Vol. 15, No. 5, 1992, pp. 1299–1301.

[61] Broyden, C. G., "A Class of Methods for Solving Nonlinear Simultaneous Equations," *Mathematics of Computation*, Vol. 19, 1965, pp. 577–593.

[62] McCue, G. A., "Quasilinearization Determination of Optimum Finite-Thrust Orbital Transfer," *AIAA Journal*, Vol. 5, No. 5, 1967, pp. 755–763.

[63] Brown, K. R., Harrold, E. F., and Johnson, G. W., "Rapid Optimization of Multiple-Burn Rocket Flights," NASA CR-1430, September 1969.

[64] Tsuchiya, T., "A Polynomial Primal-Dual Path-Following Algorithm for Second-Order Cone Programming," Tech. rep., The Institute of Statistical Mathematics, Tokyo, Japan, 1997.

[65] Monteiro, R. D. C. and Tsuchiya, T., "Polynomial Convergence of Primal-Dual Algorithms for the Second-Order Cone Program Basedon the MZ-Family of Directions," *Mathematical Programming*, Vol. 72, 2000, pp. 61–83.

[66] Tsuchiya, T., "Polynomial Convergence of Primal-Dual Algorithms for the Second-Order Cone Program Basedon the MZ-Family of Directions," *Optimization Methods and Software*, Vol. 11/12, 1999, pp. 141–182.

[67] Ye, Y., *Interior Point Algorithms, Theory and Analysis*, John Wiley, Chichester, UK, 1997.

[68] Andersen, E. D., "Handling Free Variables in Primal-Dual Interior-Point Methods Using a Quadratic Cone Approach," Tech. rep., 2002.

[69] Anjos, M. F. and Burer, S., "On Handling Free Variables in Interior-Point Methods for Conic Linear Optimization," *SIAM Journal on Optimization*, Vol. 18, No. 4, 2007, pp. 1310–1325.

[70] D., A. E. and Andersen, K. D., "Presolving in Linear Programming," *Mathematical Programming*, Vol. 71, No. 2, 1995, pp. 221–245.

[71] Mehrotra, S., "On the Implementation of a Primal-Dual Interior Point Method," *SIAM Journal on Optimization*, Vol. 2, No. 4, 1992, pp. 575–601.